Dissertation for Doctoral Degree

Study on the long-short double-pulse laser-induced breakdown spectroscopy for the steel chemical composition analysis

A dissertation submitted to

Tokushima University

in partial fulfillment of the requirements

for the doctor degree

Mechanical engineering

Intelligent structures and mechanics system engineering

Tokushima University

Minchao Cui

Supervisor: Prof. Yoshihiro Deguchi; Prof. Shengdun Zhao

September 2018

Abstract

Recently, various spectral analysis methods are studied and applied to the steel composition measurement, such as inductively coupled plasma atomic emission spectroscopy (ICP-AES), atomic absorption spectroscopy (AAS), spark optical emission spectroscopy (S-OES), laser-induced breakdown spectroscopy (LIBS). Among these spectral methods, LIBS is considered to be a good method that can be applied in the on-line detection of steel composition during making process. LIBS technique is highly anticipated because of the fast response, high sensitivity, real-time and non-contact features. For the online analysis, it is important to measure controlling factors without any sample preparation to maintain the real-time measurement feature. In this study, we have discussed the potential application fields of LIBS. With the rapid development of the modern industry, a lot of techniques have been studied for the industrial production. These advanced techniques also bring a requirement of process analysis and raw material quality control. The joint research of LIBS with other advanced techniques is meaningful for the performance improvement of industrial production. For the advanced forming production line, the quality of the steel part after forming is important for the process. LIBS technique is a promising method to analyze the formed steel parts on the production line. For the production of electrical machine of vehicle, LIBS can be applied to the quality control of the raw silicon steel plate which is one of the most important raw material for the rotor and stator of the electrical machine. LIBS technique also has a promising future in the fields of the online rapid analysis of aluminum sheet for the plastic joint process, the analysis and control of the steel making process, the waste disposal and recycling plant. According to these potential industrial applications of LIBS, the study on the analysis of manganese in steel samples were carried out in this dissertation. A new LIBS method named as long-short double-pulse LIBS (DP-LIBS) method is developed in this study for the application of real plants.

Firstly, the steel samples at solid state were measured to investigate the performance improvement of the long-short double-pulse LIBS. The role of inter-pulse delay in signal enhancement for long-short DP-LIBS was investigated by experiments, the results showed that the optimal coupling of pre-heating and re-heating effects can be obtained by firing the short pulse at the middle of long pulse. Compared with SP-LIBS, long-short DP-LIBS has obtained 3-7 folds signal enhancement in the optimal inter-pulse delay. Through the observation of plasma, the plasma images showed the remarkable differences between SP-LIBS and long-short DP-LIBS. The plasma was bigger and had a longer lifetime in long-short DP-LIBS condition. Moreover, the observed images of long pulse LIBS suggested that the long pulse can’t generate the plasma due to the low power density. The variation of plasma temperature showed that the plasma was maintained at a high and stable temperature. The variation of time-resolved intensity ratio was different for SP-LIBS and long-short DP-LIBS. I_{Mn}/I_{Fe} linearly increased with delay time in SP-LIBS condition, whereas, it showed a remarkable stabilization around the delay time

of 3000 ns in long-short DP-LIBS condition. These phenomena indicated that the plasma was stabilized by using the long-pulse-width laser beam. Through the testing at different sample temperatures, the measured spectra were consistent for long-short DP-LIBS, whereas, the spectra were significantly different for SP-LIBS. The results demonstrated that long-short DP-LIBS can be used for the online measurement of steel production line, in where the temperature of target is unknown.

For the quantitative analysis of steel samples under the simulated plant conditions, the long-short DP-LIBS method also show an acceptable performance. The long pulse made it possible to obtain clear spectra from the steel washers which had an obvious rusty layer. Through the study on the crater morphology, the improvement of detection ability can be attributed to the cleaning effect of long pulse. This result indicated that long-short DP-LIBS can be used in steel production lines, in where severe oxidation is difficult to be avoided. The emission intensity was obviously enhanced by long-short DP-LIBS because of the preheating effect of the long pulse. The comparison of spectra showed that more spectral lines were available for quantitative analysis from the spectrum of long-short DP-LIBS. This result suggested that long-short DP-LIBS can obtain more spectral information under the same experimental conditions. The measured results of long-short DP-LIBS showed a better linearity. The determination coefficients (R^2) was 0.988 for the calibration curve of long-short DP-LIBS, which is acceptable for the industrial application. Moreover, the larger slope of calibration curve for long-short DP-LIBS indicated that the effect of self-absorption was eliminated by the long pulse, which therefore improved the analytical performance of LIBS. The prediction results showed that the precision and accuracy of long-short DP-LIBS were better than those of SP-LIBS. The mean RSD% was reduced from 29.3% to 10.5% and the mean REP% was reduced from 94.9% to 4.9%.The improvement can be attributed to the stabilized plasma which was generated by long-short DP-LIBS process. The simulated prediction experiments demonstrated that the analytical performance of LIBS can be improved by adding a long pulse to the traditional SP-LIBS. The measurement results of liquid steel showed that the conventional SP-LIBS can’t obtain a satisfied calibration curve due to the unstable sample condition. However, long-short DP-LIBS showed an acceptable performance for the measurement of liquid steel samples. The fitting parameters R^2 of the calibration curve is 0.9788 for the long-short DP-LIBS, which is only 0.5329 for the SP-LIBS. At the same time, the standard deviation of the measured intensity ratio values are relative low in the long-short DP-LIBS results. It proved that the plasma is stabilized by the long pulse laser beam.

Keywords: Laser-induced breakdown spectroscopy (LIBS); Industrial application; Rapid analysis; Advanced production process; Long-short double-pulse LIBS; Steel analysis

Contents

1 Introduction

1.1 Background and significance

The modern industry production has been greatly developed in the lately decades. At the same time, with the further development of the modern industry, the quality control of production line becomes more and more important day by day. So many production companies, such as iron and steel making company, power plant, automobile manufacture company and et al., demand a convenient technique to efficiently control the quality of their products.

At present, there are mainly two types of measurement methods which were applied in the steel production plants, one type was named as the chemical analysis method and the other was named as the spectral analysis method. The chemical analysis method is already used in the steel industry for a long time. Nevertheless, chemical analysis is limited because it is quite expensive and time-consuming. For example, the quantitative determination of the main 12 elements in steel need one or two days, which is unwelcome in the steel plants [1]. Therefore, many steel production companies are trying to give up the chemical analysis methods in their plants and the spectral analysis methods of steel were developed and applied to solve the problems in the measurement of steel products. To date, various spectral analysis methods were studied for steel measurement, such as X-ray fluorescence spectroscopy (XRF), inductively coupled plasma atomic emission spectroscopy (ICP-AES), atomic absorption spectroscopy (AAS), spark optical emission spectroscopy (S-OES), laser-induced breakdown spectroscopy (LIBS). Among those spectral methods, LIBS is considered to be the only method that can be applied to the on-line detection of steel making process [2].

Laser-induced breakdown spectroscopy (LIBS) as a rapid and convenient analytical method has been successfully applied in the industrial applications, including combustions, materials, toxics, foods, and so on [1, 2]. One of the most remarkable features of LIBS is the in situ measurement capability. Objects to be measured are examined directly, and the pretreatment process, which becomes the time-consuming part of many conventional analyses, is not necessary in LIBS. There is also another merit of LIBS in spatial resolution. As for the solid material analyses, for example, LIBS has a good spatial resolution; two-dimensional (2-D) elemental distribution on the surface of a material can be detected by scanning the laser focus point or the material position.

LIBS is a kind of atomic emission spectroscopy (AES) method which uses the laser-induced plasma as the emission source. The laser-induced plasma is formed by focusing the pulsed laser beam. The emitted spectra from the plasma are detected by the combination of spectrometer and detection device [3]. The qualitative and quantitative analysis of materials can be achieved by measuring the emission intensities of the characteristic lines. LIBS is an all-optical measurement system which has the considerable features, such as no sample preparation required, remote

detection, online analysis, simultaneous multi-element analysis and relatively cheap price [4]. However, compared with other traditional analytical methods, LIBS suffers the drawbacks of low sensitivity and poor repeatability of measurement, which limit the development of LIBS application. There are many reasons for these drawbacks due to the complexity of LIBS process. The major reasons for these drawbacks include the pulse energy fluctuation, temporal and spatial non-uniformity of laser-induced plasma, uneven sample surface, matrix effects and influence of environment. Because of these difficulties, many researches of LIBS are still based on the polished samples. Some of the features of LIBS can't be reflected, such as no sample preparation, remote detection and online analysis.

Therefore, how to enhance and stabilize the laser-induced plasma is an important issue for the development of LIBS technique, especially for the industrial applications. Several methods have been reported to enhance the signal intensity or control the laser-induced plasma by employing an external energy source, such as spatial or magnetic confinement [5, 6], spark discharge LIBS [7, 8], microwave-assisted [9-11] and dual-pulse [12-14]. Usually, the additional devices for the energy supply should be installed nearby the measurement target, which is difficult in the industrial application. In dual-pulse LIBS (DP-LIBS), the additional energy is supplied by the laser beam, which is possible to be applied in online measurement. DP-LIBS configuration is realized with two independent lasers in some studies, while other researchers use a single laser to fire the dual-pulse [15, 16]. A lot of experimental results have proved that DP-LIBS is an effective method to enhance the signal intensity. The configurations of collinear, cross beam, orthogonal pre-ablation and orthogonal re-heating have been studied and reviewed with different laser power, wavelength and pulse width [17]. With the use of UV fs-ns DP-LIBS, the 360-fold signal enhancement has been obtained on a single-crystalline Si sample [18]. Using collinear DP-LIBS, the signal from the aluminum sheet sample has been enhanced near 300 times compared with that of tradition single pulse LIBS (SP-LIBS) [19].

1.2 Research status

1.2.1 Increased research on LIBS

In the last years, the number of publications in the field of LIBS shows a strong growth. Fig.1.1 shows a report of the publication amount from a database in the years 1980-2010 using the search term "laser-induced breakdown spectroscopy LIBS" in the ISI Web of Knowledge showing the nearly exponential growth of publications in the last years reaching more than 450 publications dealing with LIBS in the year 2009.

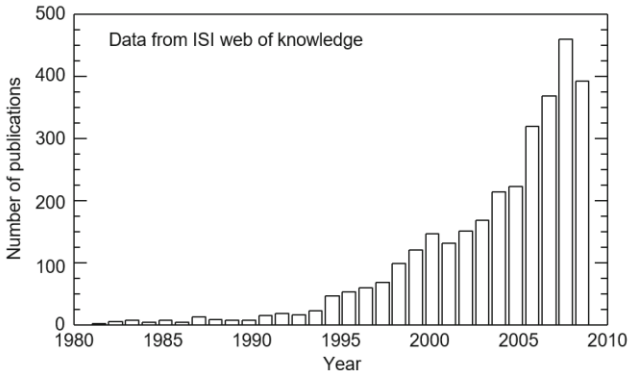

Fig. 1.1 Number of publications in the field of LIBS in the years 1980–2010: data from ISI Web of Knowledge [1]

Laser spectroscopic methods are a powerful tool for fundamental investigations, such as high-resolution spectroscopy within the Doppler width to study the fine structure of excited states [20]. Femtosecond laser pulses allow observing directly the dynamics of chemical reactions. The Nobel prize for physics in the year 1999 was awarded to A. Zerwail for his pioneering work in this field [21]. In an increasing degree laser spectroscopy enters into new application fields. Among these are the remote investigation of harmful substances in the atmosphere, the monitoring of combustion processes or material-dependent production processes, and the quality assurance of semi-finished products [22-25].

For technical applications, laser spectroscopic methods are of special interest as they are able to determine several species simultaneously with minimum equipment. Laser-induced breakdown spectroscopy (LIBS) belongs to these methods [26]. Fundamentals and applications of LIBS are the subject of this book. LIBS is able to analyze solid, liquid, and gaseous substances. In principle, laser absorption spectroscopy and LIF are also able to determine several species, but in this case different laser wavelengths are necessary, which cause a corresponding high instrumental effort for technical applications.

Focusability and temporal modulation of the power of the laser beam are the two main features of laser radiation which are exploited for LIBS. At irradiances above $10^9 W/cm^2$ a solid substance to be studied evaporates locally within a short time forming a transient plasma. In the plasma, the ablated atoms and ions are excited and emit their characteristic line radiation [27]. Emission wavelengths cover a broad spectral range from the deep ultraviolet to the infrared. A short time after the invention of the laser the emission features of the laser-induced plasma were investigated [28]. However, the used ruby lasers could only be operated at low repetition rates. Additionally the emission of the plasma was observed time integrated, so only a limited analytical quantification was achievable.

The dynamic technological developments in the field of solid state lasers, electro-optic detectors, and signal processing during the last decade were successfully utilized for LIBS. The analytical performance for a multi-element analysis achieves a level, which equals or is even

better than that of classical methods [29]. The vital point is that due to optical excitation of the measuring radiation over a distance, new fields of application were opened up, which are not accessible for conventional physical methods, such as X-ray fluorescence analysis or spark emission spectrometry. Such fields are, e.g., the inline analysis of liquid steel or the material identification for sorting and quality assurance tasks [30, 31]. Quality assurance close to the process on the basis of an automated inline measurement is the first step to fast and efficient feedback actions which result in significant cost savings and improved competitiveness.

Pulsed laser radiation can be used not only for analysis, but also for the preparation of substances to be investigated. Surface layers, as, e.g., corrosion layers, oxides, scale, contaminations, whose chemical composition differs from one of the subjacent substances, can be ablated locally by the laser beam. A mechanical preparation step, by milling, turning, or grinding, is not necessary in many cases. This dual use of the laser beam as ablation and analyzing tool has a high technological potential in terms of automation capabilities for inline inspection systems.

With diode-pumped solid state lasers, compact radiation sources of high beam quality are available offering electro-optical Q-switching with pulse repetition rates of 1 kHz and beyond, average powers of several watts, and excellent beam qualities [32]. The operating life time of these lasers amounts to more than 20,000 h. This opens for LIBS the area of spatially resolved determinations of element distributions on the surface of macroscopic samples. An example of this approach is the analysis of the cleanliness of steel samples, where microscopic inclusions in a steel matrix are determined, consisting of hard materials as, e.g., carbides and nitrides. These inclusions influence the process-ability and the material properties of steel grades. While competing methods such as scanning electron microscopy (SEM) for a spatially resolved energy-dispersive X-ray fluorescence analysis (SEM-EDX) or the electron microprobe require high vacuum conditions and an extensive sample preparation such as diamond polishing, the laser-based method measures under an inert gas atmosphere and a simple preparation of the sample surface by milling or grinding is sufficient.

The mechanisms of signal enhancement for DP-LIBS have also been widely discussed. Freeman et al. [33] have suggested that the signal enhancement can be attributed to the re-heating of plasma plume. The experiments were carried out using crossed-beam DP-LIBS. The signal enhancement was also observed when the second pulse didn’t ablate any of the brass samples. It means that the signal enhancement was attributed to the re-heating of plasma plume. However, Noll et al. [34] have concluded that the second pulse of the collinear DP-LIBS mainly transmitted through the plasma and generated the new plasma from the pre-ablated sample surface based on the plasma observation and the calculation of plasma transmission factor. In traditional DP-LIBS, the second laser pulse is also a Q-switched Nd:YAG laser pulse, which may not only re-heat the plasma but also generate new plasma from the sample surface.

Therefore, the plasma generation process and cooling process become complicated in the cases of traditional DP-LIBS.

In previous studies, the 10.6 μm CO_2 laser pulse, which can be considered as long pulse laser beam, has been applied to DP-LIBS. The enhancement of emission signal and plasma temperature has been confirmed based on the setup of Nd:YAG-CO_2 DP-LIBS [35, 36]. This dual-pulse technique was also applied to the measurement of organic films. The molecular emission signals from C_2 and CN were enhanced through the energy supply of CO_2 laser [37]. However, the CO_2 laser beam is unsuitable for the transmission with optical fiber and the CO_2 laser itself is also difficult to couple with Nd:YAG laser compactly, which may suffer the limitations in industrial application. For our research interest, we are focusing on the industrial application of LIBS, especially the non-contact and real-time measurement of industrial production lines. In this work, a long-pulse-width Nd:YAG laser was applied to the laser-induced plasma process in order to enhance and stabilize the plasma. The long-pulse-width laser means that the duration time of laser pulse is long but the peak power of laser pulse is low. More specifically, a Nd:YAG laser, which was operated at free running (FR) mode, was employed in current study to generate the long-pulse-width laser beam with 1064 nm wavelength and 60 μs pulse width.

The features of LIBS compared with those of other laser spectroscopic methods are promising for the industrial applications. Laser-induced breakdown spectroscopy is the only method, which allows for a simultaneous multispecies analysis in all states of aggregation of a substance. At the same time, LIBS requires a relative low price devices and is suitable for the terrible measurement conditions compare than other measurement method for the real industry. Therefore, the discussion on the LIBS methods, applications and improvement are strongly growth in recent years.

1.2.2 Measurement of steel samples in laboratory

It is well known that the iron and steel industry is one of the most important industries for human beings. In modern life, steel products are used almost everywhere. With the development of industry, high quality steel is desired in various fields. The advanced control methods for steelmaking process are required to meet these industrial demands. However, it is difficult and expensive to measure the composition of steel during the steelmaking process, which limited the production efficiency of high quality steel. In recent years, laser-induced breakdown spectroscopy (LIBS), as one of the analytical techniques for steelmaking process, has been widely studied because of its potential for on-line analysis [1, 2, 20]. Various papers have been published to report the applications of LIBS in steel industry, such as the measurements of solid steel [38-44], liquid steel [45-47], slags [48-49], oxides [50-52], rapid in-suit analysis [53-55], etc. One vital subject among these studies is the analytical performance of LIBS for the industrial application. To improve the performance, many approaches have been developed based on LIBS,

such as microwave-assisted LIBS [10, 11], LIBS laser-induced fluorescence [56], resonance-enhanced LIBS [57, 58], dual-pulse LIBS [59-64], etc. However, it is still difficult to apply LIBS in the steelmaking process due to the terrible measurement conditions of steel plant. Dual-pulse LIBS (DP-LIBS) is a promising way to enhance the detection performance in practical application. Many geometrical configurations (reheating [59], collinear [60], crossed beam [61], etc.) have been studied to realize DP-LIBS. Among these configurations of DP-LIBS, the collinear configuration is feasible for the application in steel production lines [2]. However, the plasma conditions are still temporally unstable and spatially non-uniform [65, 66].

As well known, the theory of LIBS process is quite complex since several physical processes were involved in the generation and evolution of plasma, such as photo ionization, high velocity impact between electrons, atoms, molecules and ions, and inverse bremsstrahlung. The complete physical-mathematical model, which can finely describe the LIBS process, has not been established till now [67]. The unstable and non-uniform laser-induced plasma leads to the unsatisfied performance of LIBS for industrial requirements. Even though the temperature in plasma core is very high (104 K magnitude), the temperature in plasma edge is still very low (only a few thousand Kelvin) [68]. LIBS utilizes the signals which were emitted from the non-uniform plasma. However, at present, most of the quantitative analysis methods for LIBS assumed that the laser-induced plasma was under the local thermodynamic equilibrium (LTE) condition. LTE condition means that the temperature of a local region in plasma tends to be equalized. In fact, LTE condition of laser-induced plasma was not well satisfied in the often cases of LIBS measurement. In previous reports, several works have obtained the high-accuracy results for quantitative analysis through considering unstable plasma conditions [68-70]. In order to generate a more stable plasma, the collinear long-short DP-LIBS has been proposed in the previous work. The feasibility of the new method has been verified through the experiments in air and under water. The results have suggested that the plasma cooling process was controlled by the long-pulse-width laser [71].

1.2.3 Measurement of steel products on production line

In the metallurgical industry, the analysis of the elemental components in steelmaking process is a vital requirement for the quality control of production. At present, the conventional techniques used in steelmaking plants are difficult to be applied to the real-time and online analysis of elemental components due to the requirement of sample preparation [2], such as X-ray fluorescence spectroscopy (XRF), inductively coupled plasma atomic emission spectroscopy (ICP-AES) and spark optical emission spectroscopy (S-OES). Laser-induced breakdown spectroscopy (LIBS) is a qualitative and quantitative analysis technique which is based on the interaction of laser and material. It utilizes a focused laser beam to ablate the surface of target thereby generates the plasma. Through the record and analysis of plasma spectra, the elemental composition and the element content of target can be analyzed conveniently. In recent decades,

LIBS technique has been widely studied because of the features such as multi-element rapid and simultaneous analysis, no sample preparation, available measurement for solid, liquid and gas, et al [1, 2].

Another important feature for LIBS technique is the potential for online analysis, which attracts many researchers to apply LIBS technique to the online analysis of steelmaking process. Noll et al. [56] have applied LIBS to the steelmaking process and realized the monitor of steel quality. In the experiment of Gruber et al. [45], a 12 m optical fiber was employed to transmit the plasma emission signal, the contents of Cr, Cu, Mn and Ni in liquid steel were obtained in 7 seconds. Sun et al. [54] have also realized the monitor of liquid steel contents by double-pulse LIBS with a Cassegrain telescope. Palanco et al. [37] have designed a remote LIBS system for the monitor of Cr and Ni contents in liquid steel. Hubmer et la. [72] proposed a LIBS configuration for the analysis of liquid high-alloy-steel. An optical fiber cable was employed to transmit the plasma signal over a distance of 10 m.

Due to the poor environmental conditions in the steelmaking plants, such as high temperature, dust, vibration, et al., the protection of optics is hard, which limits the practical application of LIBS technique. Therefore, some scholars carried out the research of open-path remote LIBS system for practical application. Palanco et al. [73] developed an open-path LIBS system with a 7.5 m beam path in air. The experimental results demonstrated that the content of Cr and Ni in liquid steel were successfully measured. Sun et al. [74-76] have also developed an open-path LIBS system for the monitor of compositional variation in a 30 kg induction furnace. Although the literature contains a large number of studies on the online measurement of steel using LIBS, there are still some topics worth to be studied for the online application in steelmaking plants. One valuable subject is the remote analysis of high temperature steel products in solid phase. The quality of steel product is largely affected by the feedback information in different manufacture stages. The analysis of the finished steel product is an important part for the online LIBS system. However, the high temperatures, the uneven of liquid steel, the significant oxide layer are involved in the LIBS online analysis due to the finished steel product on production line are very hot. It is still left a lot of work to do in order to promote the LIBS technique to the real application in steel production lines.

1.3 Contents and structure of this dissertation

The purpose of this dissertation is to give a introduction of LIBS for the application of steel composition measurement, the relevant devices parameters, the improvement of LIBS for the real application in steel plant, the comparative studies results between the long-short double pulse LIBS and conventional LIBS method, the measurement results of long-short DP-LIBS in the simulated plant conditions. For these purposes, the structure of this dissertation is organized as the follows chapters. The rapid analysis requirements on the steel composition from the industrial production are discussed firstly in Chap. 2. The studies on the advanced forming

process, the novel electric machine, the mechanical joint process are presented here. According to the requirements of these fields, the joint research between LIBS and the industrial production fields are discussed. Chap. 3 gives an overview of the fundamental of Laser-Induced Breakdown Spectroscopy. The typical LIBS measurement processes, devices, parameters are discussed in this chapter. In addition, the principle of the long-short DP-LIBS method is presented here also. The details of the experimental systems and devices are presented in Chap. 4. In Chap. 5, the comparative studies results between long-short DP-LIBS and conventional LIBS are discussed. In Chap. 6, the experimental results of the measurement in the simulated steel plant conditions are presented and discussed. Finally, the conclusions and outlook of this work are drawn in Chap. 7.

2 Rapid analysis requirements of industrial production

In the last century, the rapid development of industry has brought a huge demand of product quality control on the production line. In various production lines, the chemical composition of the products needs to be analyzed timely in order to adjust the parameters of production line, which is important for the quality and efficiency of production. In recent years, the requirements of rapid analysis method becomes urgent in the advanced mechanical systems. Especially in the field of advance equipment development, some novel mechanical equipment or systems can't be applied to real production because of the lack of rapid online analysis method. Therefore, it is valuable to carry out the joint research on the advanced mechanical equipment or systems and rapid analysis method for product quality control. In this chapter, we have studied and developed various advanced mechanical systems. The joint research on the advanced mechanical systems and laser-induced breakdown spectroscopy is also discussed to apply both of the techniques to the real industry. The rapid analysis requirements of the advanced mechanical equipment or systems are discussed as follows.

2.1 Rapid analysis of advanced forming process

Spline shafts are widely used to transmit motion or torque between shafts in the mechanical system, and the advantages of spline shaft connection attracted lots of interests attributed to their high connection strength, high reliability, compact structure and convenient assembly [77]. The various advantages of spline shaft connection bring the extensive application of spline shaft in the industries of aerospace, ship, engineering machinery and automobile. For example, a standard car contains more than 30 spline shafts. As shown in Fig. 2.1, the installed positions of spline shafts include transmission, differential, clutch and etc. [78, 79]. Furthermore, higher requirement of the performance of spline shaft has been put forward in the modern manufacturing. Thus, it is essential to study the novel manufacture process of spline shaft to obtain higher performance.

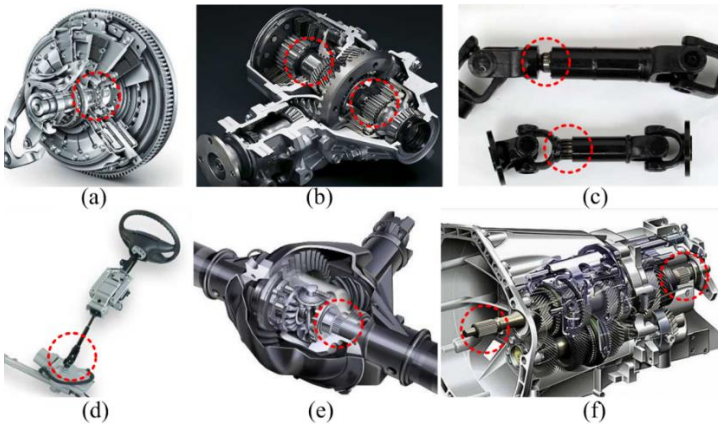

Fig. 2.1 Installation positions of the spline shaft in automobile: (a) Clutch; (b) Driving axle; (c) Transmission assembly; (d) Steering assembly; (e) Differential; (f) Transmission

Recently, the researches and applications of the plastic rolling process of spline shaft become more and more active for its advantages such as superior product quality, saving of raw materials, high productivity and low cost [80, 81]. Rolling process can be applied in the products which have axisymmetric cross area such as spline shafts and gears [82, 83]. The traditional rolling processes can be summarized as three types: rolling process with rack dies, with round dies and with incremental dies. Fig. 2.2 shows the principle of traditional rolling processes applied in spline shafts. The blank is just rotated along the circumferential by the driven of dies and the teeth are formed in the radial direction gradually due to the in-feed of dies. Although these traditional rolling processes can realize the forming of spline shaft, there are still some problems such as the huge forming load, dies wear, inaccurate tooth number of formed spline shaft and insufficient of material flow [80, 83]. In an attempt to solve the above problems, an axial-infeed incremental rolling process of spline shaft with 42CrMo steel is proposed. It is a novel metal forming process in which the blank of spline shaft is pressed into the rolling dies continuously and the material in the surface of the blank is formed to a certain shape. The forming load is divided into axial and radial load, so the die life improves. There are many factors that affect the axial-infeed incremental rolling process such as die angle, in feed velocity and rotational speed, and the Finite Element Method (FEM) is also widely utilized to optimize the process parameters [84, 85]. The plastic properties and constitutive equations of 42CrMo steel were investigated [86-88]. The experimental research on forming parameters for spline rolling with round dies was carried out [89]. The phase synchronous problem of three dies was solved by Zhang et al [90].

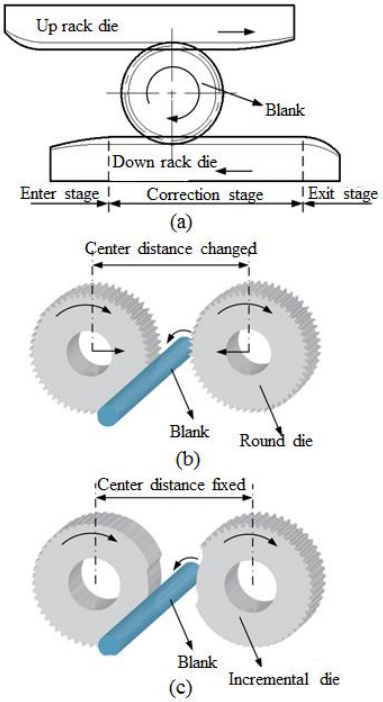

Fig. 2.2 The schematic diagrams of traditional rolling processes of spline shaft: (a) with rack dies, (b) with round dies and (c) with incremental dies.

As shown in Fig. 2.3(a), the axial-infeed incremental rolling system mainly contains three rolling dies, back-drive center and blank. The three rolling dies were assembled along the circumference evenly. Along the axial direction, each rolling die contains die angle part with the angle and correction part, as shown in Fig. 2.3(b). The function of die angle part is preforming for spline shaft and the function of correction part is adjustment for tooth profile. The back-drive center has the same tooth profile parameters with spline shaft, so it could determine the initial phase of the rolling dies and ensure the die speed keep consistent.

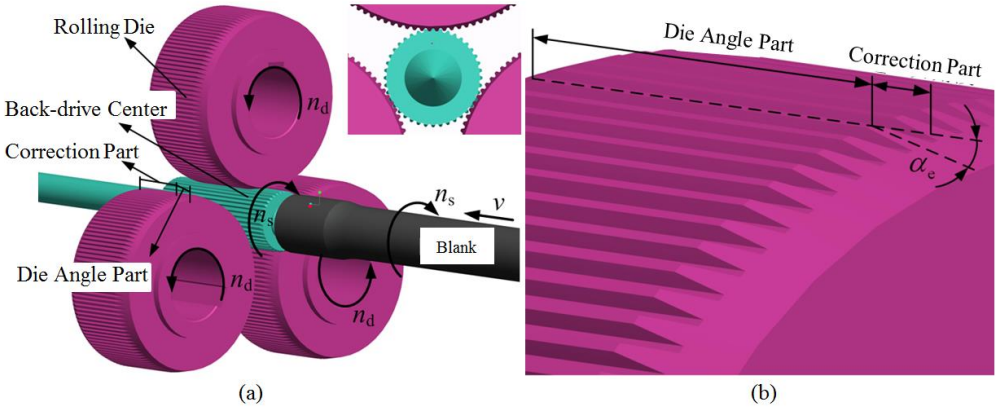

Fig. 2.3. Diagram of the axial-infeed incremental process: (a) the axial-infeed incremental rolling system and (b) the local structure of the rolling die

The axial-infeed incremental rolling process as shown in Fig. 2.4 and it includes the following steps. (1) The blank is clamped by the former-drive center and the back-drive center. (2) The rolling dies rotate at the same speed and drive the blank rotate. (3) The blank is fed along the axial direction by the center and the deformation of the metal occurs on the surface of the blank. Under the action of multiple pre-rolling, the plastic deformation of the blank increase continually. Then, the preformed tooth profile is adjusted by the correction part. Due to pre-rolling and adjust-rolling, the dimension precision and surface quality increase. (4) After rolling, the rolling dies retract slightly along the radius direction and the formed spline shaft is pushed off along the inversion direction, the forming process end.

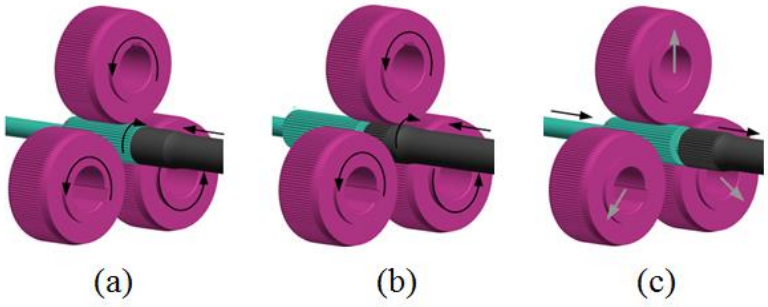

Fig. 2.4 Diagram of the steps of the rolling process: (a) Before rolling, (b) During rolling and (c) After rolling

An axial-infeed incremental rolling equipment was designed, manufactured and assembled as shown in Fig. 2.5. The axial movement of blank is realized by two air cylinders. The big one is installed in the right side and drives the former-drive center (not draw in Fig. 2.5). The small one is installed in the left side and drives the back-drive center (in the center of Fig. 2.5). When the bland feeding, the big cylinder provides propulsion and the small cylinder provides a proper clamping force. The axial forming force and friction force are overcome by the propulsion of big cylinder. When the blank exiting, the small cylinder provides a proper force to push-out the formed spline shaft.

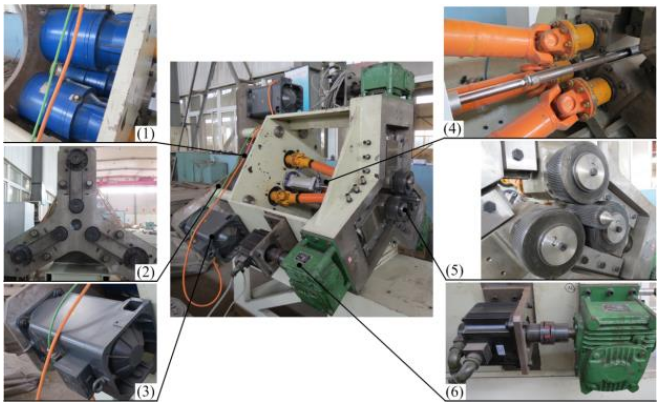

Fig. 2.5 The axial-infeed incremental rolling equipment: (1) Planetary reducer, (2) Synchronous Belt Transmission, (3) Main AC servo motor, (4) Universal coupling, (5) Rolling position and (6) Diameter control AC servo motor and worm gear reducer

Then, the experiments of axial-infeed incremental rolling process of spline shaft with 42CrMo steel are carried out and the metal structure and hardness of formed spline shaft are investigated.

The experimental blank of spline shaft is designed, which is similar to the end part of the real spline shaft that used in the heavy truck, and the shape and sizes are shown in Fig. 2.6(a). Meanwhile, Fig.2.6(b) shows the real picture of the blank of spline shaft.

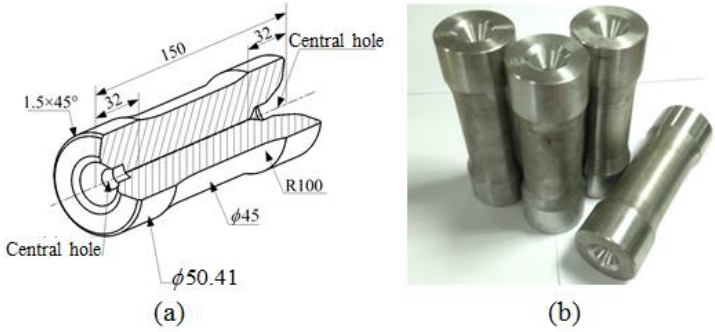

Fig. 2.6 The shape and sizes of the blank of spline shaft: (a) shape and sizes and (b) real picture of blank shaft

The axial-infeed incremental rolling experimental process is shown in Fig. 2.7. The whole rolling process lasted about 2 min, including (1) feed before rolling 15s, (2) axial-infeed rolling 64s (the feed speed mm·s-1), (3) correction rolling 15s and (4) reverse out 15s.

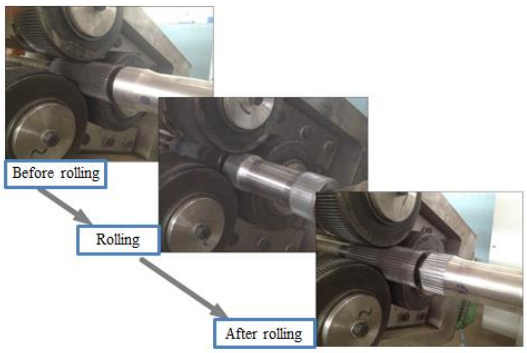

Fig. 2.7 The axial-infeed incremental rolling experimental process

The microstructure of the formed spline shaft with 42CrMo steel is shown in Fig. 2.8 (the process parameters are: the diameter of blank is 50.85mm, the rotation speed of rolling dies is 25r • min^{-1}, the feed speed is 0.5mm • s^{-1}, the forming temperature is 20℃ and the die angle of rolling dies is 9°). For details, the width of the sample is about 12mm along the circumferential direction and the depth is about 10mm along the radial direction. The sample is cut, polished and corroded by 4% nitric acid alcohol solution, and then it is observed by optical microscope (Leica DMI3000M metallographic microscope).

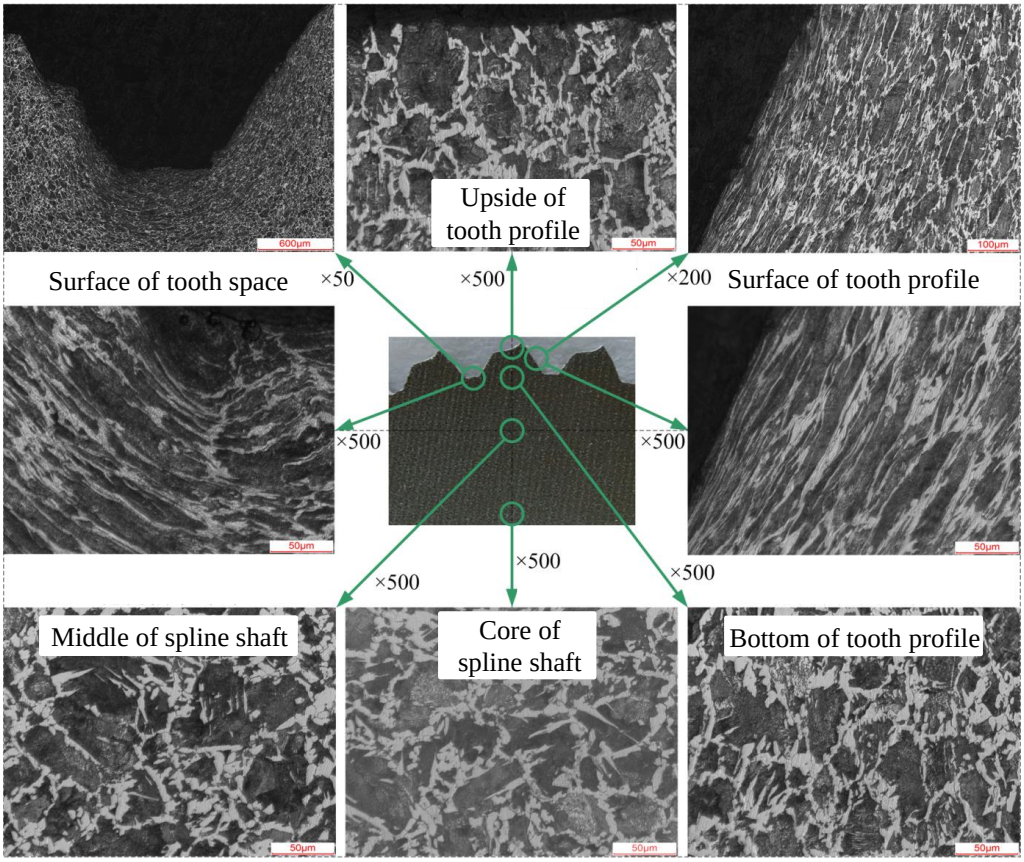

Fig. 2.8 Microstructures of different areas in the cross section of the formed spline shaft with No.45 steel

The microstructure contains ferrite, pearlite and sorbite in the core and middle of the formed spline shaft and the microstructure is slightly stretched along the outward radial direction in the bottom and top of the tooth profile (this change can evidently refine the grain size and improve the distributed uniformity of structure). The microstructure in the bottom of tooth root area is fibrous tissue which is composed of ferrite and pearlite. The fibrous tissue was refined obviously and its flow line was distributed along the bottom of the tooth root to adjacent tooth root area, continue to the surface of tooth profile. The fracture, fragmentation, dissolution, balling of pearlite and the refinement of ferrite are obviously viewed in this area, so the grain density increases. The surface of tooth profile is fibrous tissue which is composed of clipper-built ferrite and pearlite. The fibrous tissue's grain is obviously refined and dense, and the flow line is distributed along the direction of the tooth surface (With the increase of depth along the direction from the tooth surface to core, the fibrous tissue disappears gradually and the grain density reduces gradually).

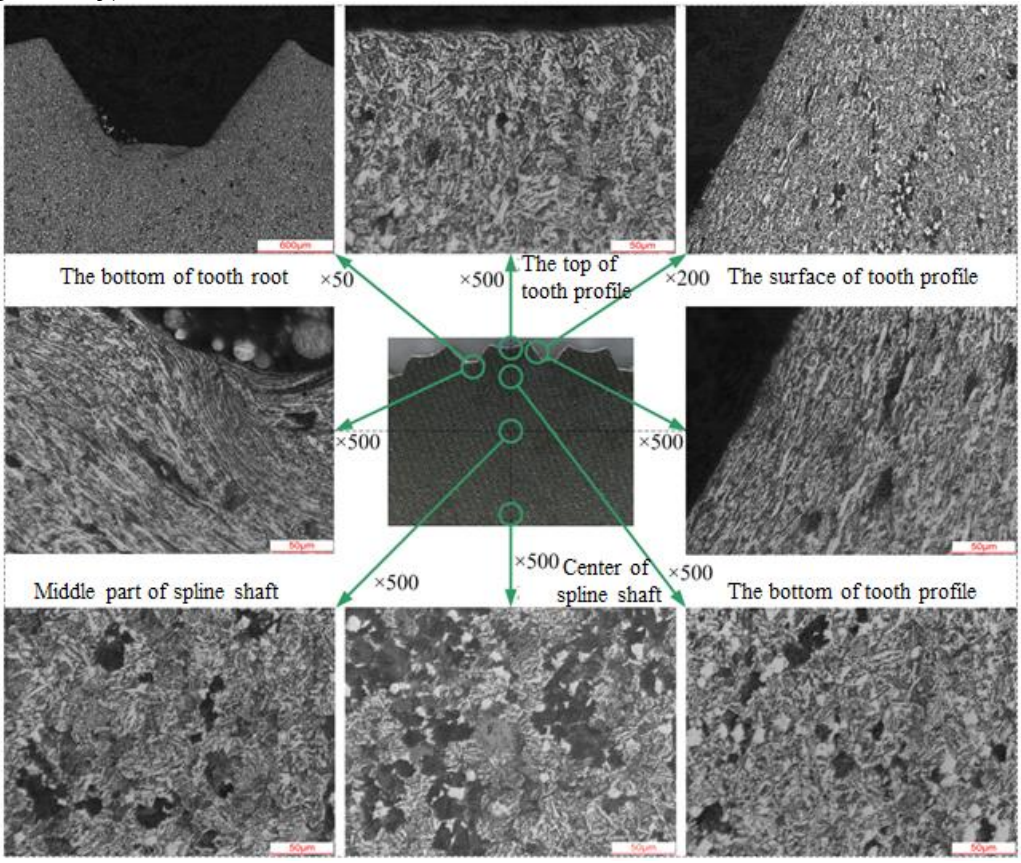

Fig. 2.9 The metal structure of the formed spline shaft with 42CrMo steel

It can be seen in Fig. 2.8 that the microstructure of spline shaft was changed after the axial-infeed incremental rolling process. Due to this effect, the usability of the formed spline shaft is improved. However, it is very difficult to control microstructure of spline shaft during the rolling process. For example, the microstructure of the formed spline shaft is changed at high

temperature. In the real production of spline shaft, the warm forming temperature is used to decrease the forming forces and protect the rolling dies. We have also carried out the experiments at 650 ^{o}C, the microstructure of the formed spline shaft is showed in Fig. 2.9. It can be seen that the microstructure is definitely different with that of room temperature. The results inducted that the forming temperature has the influences on the microstructure of spline shaft. However, in the real production of spline shaft, we do not precisely control the forming temperature of spline shaft. A wide temperature range are used for the production of spline shaft. Therefore, we have to develop the technique to evaluate the microstructure of the formed spline shaft. For the real production, it is very important to product the spline shat with the same mechanical properties.

LIBS is an effective method to be applied in the axial-incremental rolling equipment. Due to the change of microstructure of local region, the relevant composition of the steel will also be changed. The distribution of carbon element and other alloy elements will be different in different region of the formed spline shaft. Using LIBS, we can rapidly measure the variation of the steel composition. For each of the spline shaft, we can control the difference of the surface composition in a low level. Therefore, the mechanical properties of the formed spline shaft can be control in the same level, which is important for the use of this part. In conclusion, the application of axial-incremental rolling process and equipment of spline shaft have a great desire of rapid analysis method for the chemical composition. LIBS is considered to be a feasible method to be applied to this process and equipment.

2.2 Application to the production of electrical machine of vehicle

The widespread use of traditional fossil fuel vehicles has brought global environmental and energy problems, which leads to an urgent demand of environmental-friendly cars. Electric Vehicle (EV), which is rapidly developed in recent years, is considered to be a long-term solution for air pollution problem [91]. However, the large-scale application of EV is limited due to several bottlenecks such as automobile technology, battery quality, charging facilities and production cost. For this reason, Hybrid Electric Vehicle (HEV), which possesses both the advantages of fossil fuel vehicles and electric vehicles, have attracted the attention of researchers [92, 93].

Integrated Starter and Generator (ISG), which can be operated in starting mode and generating mode, is an effective and simple method to realize a HEV strategy [94]. ISG replaces the original position of starter and cooperates with the flywheel ring gear of the engine. In the starting mode, ISG can start the engine and drive the car like motor. In the generating mode, ISG provides the required electricity for vehicle-mounted devices and battery charging. It is considered as a great hybrid power strategy for traditional cars. ISG can reduce the surrounding parts of the engine and realize mild/medium hybrid power on the basis of original engine and transmission system. Therefore, ISG technology becomes an important branch of HEV research [95-98].

Switched Reluctance Machine (SRM) was considered to be a good choice for ISG machine before [91, 93, 94, 97]. The design methodology for the switched reluctance motor/generator has been introduced by Faiz and Moayed-Zadeh, which is based on pre-defined equations with the objective functions as high torque over low speed and high efficiency over high speed.1 A two phase SRM was designed by Lee and Krishnan [99]. The E-core structure was applied in the common pole, and two or four large poles and four small poles were configured on the stator. The common poles are shared by both phases for positive torque production through the entire operation. In 2013, a two-layer 6/4 three-phase switched reluctance motor/generator has been designed and analyzed [100]. Different geometries of SRM have been proposed in 2007 [101]. The rotor and stator poles were designed with different pole arcs and the air gap width is variable. In 2012, a two-phase SRM with modified shape of rotor poles and optimized output torque has been presented [102]. Besides, many kinds of SRM with specific characteristics have also been discussed, such as hybrid stator pole [103], axial-type [104], dual channel [105], multi-layer [106], isolated double layer [107], linear [108], disc-type machine [109], etc [110-112]. Although the SRM has been widely studied in the field of ISG and Motor/Generator, there are still some inherent problems to be solved [113]. The requirement of excitation and low output power density are two major problems for SRM in HEV applications [114-116]. To solve these problems, Flux Switching Permanent Magnet Machine (FSPMM) seems to be an ideal choice [117-119].

FSPMM shows the significant advantages in many aspects, such as robust mechanical structure, simple rotor structure (similar to the SRM), high power density and torque density. Thus a lot of studies on FSPMM have been reported in recent years. FSPMM can work in rough conditions and high speed applications because of the excellent robustness and the simple structure. Most of the studies are focused on the output torque of FSPMM, which aim to develop a main traction motor for HEV or EV. In 2014, a dual excitation switched-flux motor has been designed and analyzed to develop a traction motor for HEV [120]. In 2009 and 2011, the 6/8 type and the 6/5 type FSPMM machines have been discussed for HEV application respectively [121, 122]. Based on an in-wheel drive EV (out-rotor flux switching starter), the impact of different rotor pole number has been presented in 2013 [123]. However, the applications of FSPMM are still limited due to the bottlenecks of battery performance and capacity in cars [124, 125]. Considering the current battery performance, the Flux Switching Integrated Starter Generator (FSISG) is proposed to provide a hybrid power strategy for traditional cars. FSISG takes the advantages of power generating capacity and torque output ability of FSPMM, which provides a new way for the application of flux switching machines in HEV.

The working principle of FSISG is illustrated in Fig. 2.10. In power generating mode, the rotor teeth are moved along the movement direction by the external driving torque which is applied to the rotor. According to the magnetic resistance minimum principle and the magnetization direction of permanent magnet, the direction of the magnetic circuit can be determined. As

shown in Fig. 2.10, while the rotor tooth locates at different positions, the directions of magnetic circuit are showed with black arrow-lines. The direction of magnetic flux in the winding is from down to up at position 1, but it changes to the opposite direction at position 2. According to the law of electromagnetic induction, the induced electromotive force will be generated in the winding. The electromotive force in the windings will cyclically change with the continuous rotation of rotor. Therefore, FSISG can output electromotive force without external electric excitation. In the torque output mode, the principle is the inverse process of power generating mode. The alternating current is applied in the windings properly. Then, the inductive magnetic field of the windings switches the direction of the magnetic flux. At the same time, the rotor is rotated by magnetic field force.

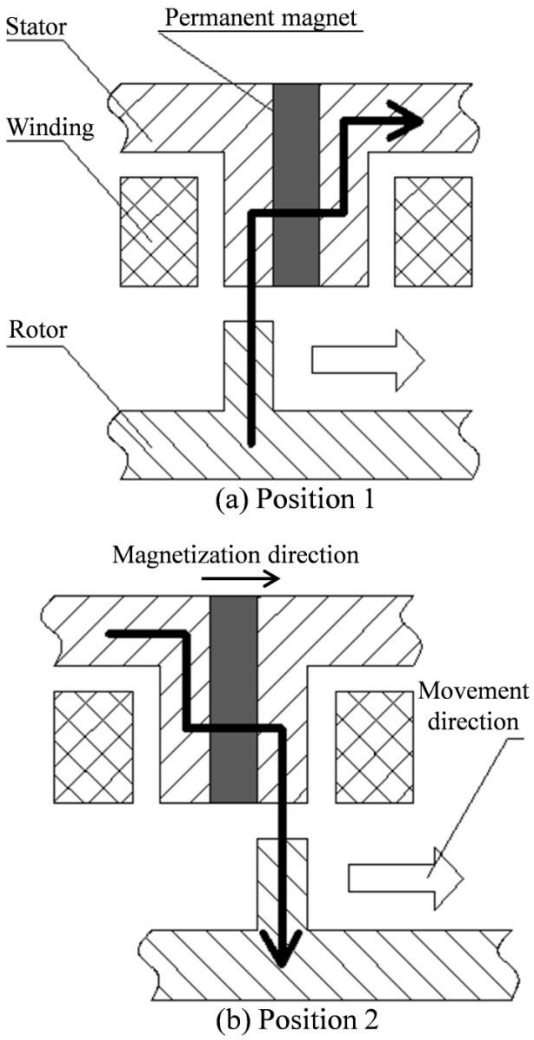

Fig. 2.10 Working principle of FSISG: (a) position 1 and (b) position 2.

Fig. 2.11 shows the working principle of FSISG system in HEV. The FSISG system mainly contains FSISG, control circuits and car battery. In starting mode, FSISG works as a starter or a drive motor, which outputs the torque through gear engagement. The electric energy of car

battery assists the engine to drive the car through the conversion of FSISG system. In generating mode, FSISG converts the kinetic energy of car to electricity energy. Then, the energy can be used for recharging battery and supporting electrical appliances in car. In brief, FSISG system makes a two-way transfer of energy between the driving system and the battery in car.

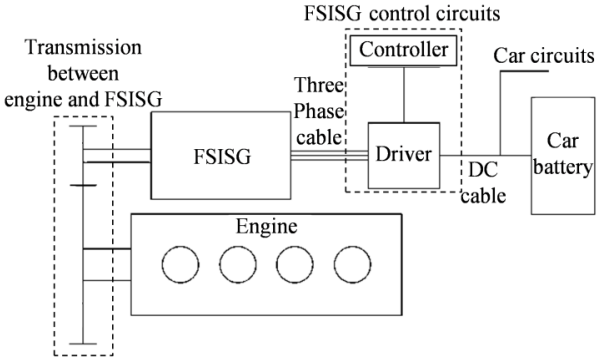

Fig. 2.11 Principle of ISG system with FSISG.

In order to develop a high performance starter and generator for HEV, a 12-10 FSISG machine is simulated by the finite element method. In the generating mode, the distributions of magnetic flux density with different rotor positions are showed in Fig. 2.12. The maximum magnetic flux density value is 1.5 T, which appears in the end of rotor teeth. As the reference tooth moves from 0° position (Fig. 2.12a) to 18° position (Fig. 2.12c), the average magnetic flux density increases from 0.3 T to 1.5 T accordingly. Then, it decreases to 0.3 T when the position of reference tooth is 27° (Fig. 2.12d). According to Fig. 2.12, the maximum magnetic flux density appears in the end of stator teeth and rotor teeth. Therefore, the parameters of stator teeth and rotor teeth should be verified to ensure the efficiency when designing a new machine for FSISG. However, it can be seen from Fig. 2.12 that there is a large area of magnetic saturation in stator teeth and rotor teeth. It indicates that the novel FSISG has high requirements for the magnetization properties of silicon steel sheets.

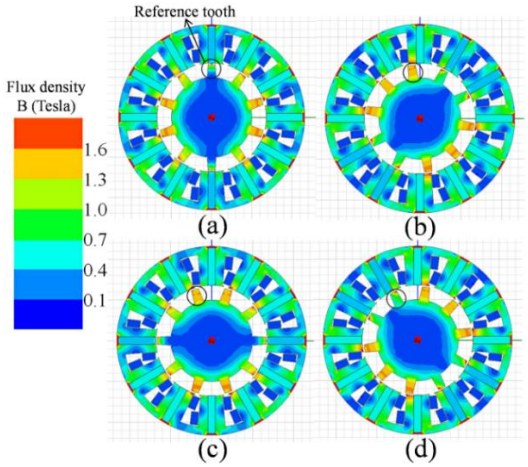

Fig. 2.12 Magnetic flux density distributions at different rotor positions: (a) 0º, (b) 9 º, (c) 18 º and (d) 27 º.

For the application of FSISG technique, it is important to control the composition of silicon steel sheets during the production of steel sheet. In order to realize a high performance of transfer efficiency, each of the silicon steel sheet should has the high and same magnetization properties. However, in present, the production of silicon steel sheets is very rough, the magnetization properties of different silicon steel sheets are fluctuant usually. In order to product the high quality silicon steel sheets which meet the requirement of FSISG machine, the rapid analysis method is required for the production line of silicon steel sheets. LIBS is considered to be suitable for this purpose, due to the simple instruments, on-line analysis ability and low coast. Thus LIBS is studied for the steel measurement in this dissertation to possibly solve the requirement of FSISG technique for the high quality silicon steel sheets.

2.3 Online rapid analysis of aluminum sheet for the plastic joint process

Aluminium alloy has been widely used in the automotive industry. In recent years, the joining of aluminium alloy becomes a hot research topic. Welding, self-pierce riveting, clinch riveting, adhesive bonding and mechanical clinching can be used to join aluminium alloy and other metal materials [126–131]. However, it is difficult for welding method to join aluminium alloy because of the high thermal conductivity, oxide layer on the sheet surface and low melting point [132]. A special rivet is required in the self-pierce riveting process. The cost of production may be increased by the rivet. In addition, the upper sheet will be penetrated by the rivet in the self-pierce riveting process, which will damage the aluminium alloy sheet. There is a convenient method to join aluminium alloy sheets by adhesive bonding. No dies and no rivet are needed in the adhesive bonding process. However, the surface of the sheet must be kept clean before the adhesive bonding. It takes a long time to bond the sheets by adhesive. Adhesive is needed as auxiliary in this process, which may increase the cost.

An effective way for joining aluminium alloy sheets is mechanical clinching technology, which has been investigated by many researchers [133-138]. There is no rivet required in the clinching process [139, 140], which reduces the cost of production. The clinched joint was produced by plastic deformation. There is no chemical reaction in the process. The upper sheet and lower sheet are joined together by an interlock. No light, no spark and no smoke are generated in the clinching process, which contributes to protect the environment.

A design method of the clinching dies used for joining aluminium alloy sheets was proposed by Lee et al. [141]. The top-hat impact test was carried out to assess the reliability of the clinched joint used in the automobile. The results showed that the clinched joint with aluminium alloy sheets had a similar crash resistance with the self-pierce riveted joint.

Aluminium alloy sheet and polymer sheet also can be joined together [142, 143]. Lambiase et al. [144, 145] investigated the polymer-metal hybrid joints in many different aspects. The mechanical clinching method was proved to be effective to join aluminium alloy sheet and polymer sheet.

Aluminium alloy sheet and high strength steel sheet also can be joined effectively. The sheets undergo large plastic deformation in the mechanical clinching process [146, 147]. Because of the small ductility, it is easy for high strength steel to fracture around the corner radius of the punch. In order to prevent the fracture, the clinching dies were optimized to control the metal flow of the sheets [148]. When the high strength steel was taken as the upper sheet, the die depth should be decreased to prevent the deformation concentration of the sheets. A numerical investigation of the clinched joint with aluminium alloy was conducted by He et al. [149]. Experimental tests were carried out to validate the numerical model. The numerical results were in good agreement with the experimental results.

The strength of the clinched joint can be increased by increasing the joint number and joint diameter. The arrangement of the sheet in relation to the clinching dies has an important influence on the mechanical properties of the clinched joint [150].

In fact, the clinched joint has a lower static strength than the welded joint and self-pierce riveted joint. In order to increase the strength of the joint, some new fastening methods have been investigated. It is essential for clinched joint to benefit from other fastening method. Adhesive bonding method was used to increase the static strength of the clinched joint [151]. The rigidity and tightness of the joint structure can be enhanced by the adhesive. The clinch-bonded hybrid joint has higher energy absorption than the clinched joint in the tension shearing test.

A clinch riveting method was presented for joining different thin steel sheets [152, 153]. The quality of the joint was evaluated by conducting tension-shearing strength test. The tension-shearing strength can be increased effectively by the clinch riveting method. The special rivet used in this process may change the separation mode of the upper sheet and lower sheet.

A reshaping method was proposed to increase the pull-out strength and shear strength of the clinched joint [154]. A pair of special dies was used to compress the joint. The reshaping method was effective for increasing the strength of the clinched joint. However, a pair of special dies is required to compress the joint. The upper die is contoured, and the lower die is bumped. The upper contoured die must be placed on the same axis with the lower bumped die, which makes the operation more complex. In addition, the optimization of the reshaping tools is the key content of their study. Only one group of geometrical parameters was investigated, which could not reflect the quality of the reshaped joint. The geometrical parameters, energy absorption and failure mode of the reshaped joints were not investigated. In order to increase the strength of the clinched joint, some new reshaping methods should be investigated, and the existing reshaping methods should be improved.

Chen et al. presented a reshaping method with a rivet [155, 156]. The strength of the joint can be increased obviously by this reshaping method. A rivet was used to increase the strength of the joint and control the material flow. The protrusion can be reduced and the strength can be

increased in the reshaping process. However, an additional rivet is required in the reshaping process, which may increase the weight of the joint. It is better to reduce the weight of the joint on the lightweight automobile. In addition, they also presented another reshaping method with a pair of flat dies [157, 158]. The dies are easy to produce, and the operation of the dies is easy. However, the strength of the reshaped joint with a pair of flat dies cannot be increased observably.

The previous works are mainly the reshaping method with a rivet and another reshaping method with a pair of flat dies. In this study, a height-reducing method with a bumped die and a flat die was investigated. Without the use of rivet or other additional elements, the weight of the height-reduced joint by a bumped die and a flat die is not increased, which meets the requirements of automotive lightweight. The height-reduced joint by a bumped die and a flat die has a higher strength than the reshaped joint with a pair of flat dies. The height-reducing process has many advantages which other reshaping processes do not have, so this height-reducing process should be investigated. AL5052 which is widely used on the automotive body is used as the material of the sheets. Extensible dies were used to produce the clinched joint, while a flat die and a bumped die were used to produce the height-reduced joint. The protrusion of the clinched joint was compressed by the flat die. Different joints with different geometrical parameters were used to conduct the cross-tensile tests. The cross-tensile strength, energy absorption and failure mode of the joint are investigated. The height-reducing method was proved effective for increasing the strength of the clinched joint.

As shown in Fig. 2.13, a clinched joint was produced by the mechanical clinching method. Extensible dies were used in the mechanical clinching process. The dies were made of high strength steel materials which can increase the durability of the extensible dies. The extensible dies consist of the sliding sectors, punch, fixed anvil, blank holder and spring. The geometrical parameters of the extensible dies used in the clinching process are shown in Fig. 2.14. In order to make the material flow uniformly, three sliding sectors were used in the extensible dies. Two AL5052 sheets were stacked on the three sliding sectors in the mechanical clinching. The blank holder was used to fix the upper and lower sheets to make sure that the deformation of the sheets occurs mainly in the cavity volume.

The mechanical clinching process was conducted on a clinching machine which was produced by the Express Company. A pressurized oil-air cylinder is used in the clinching machine to produce pressure on the punch. The displacement of the punch can be detected and controlled by the displacement sensor.

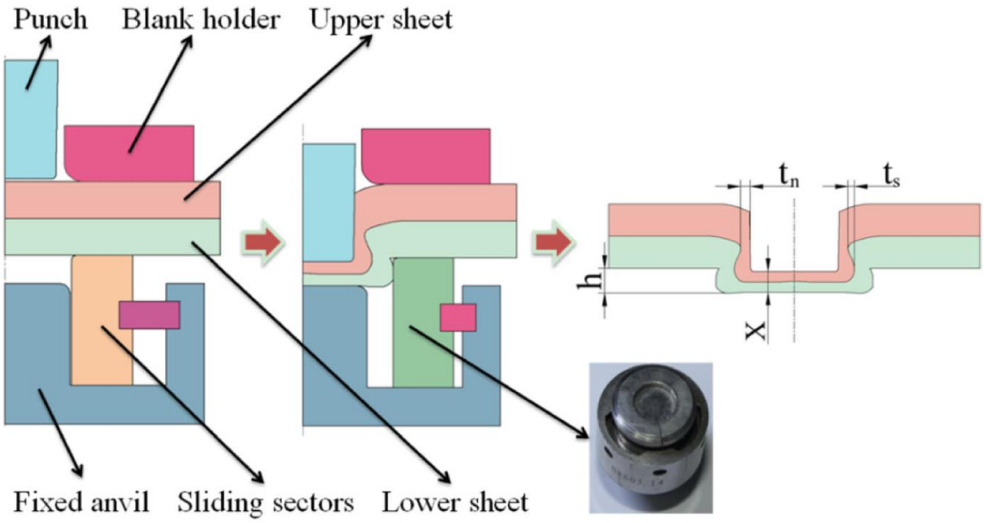

Fig. 2.13 Principle of mechanical clinching process

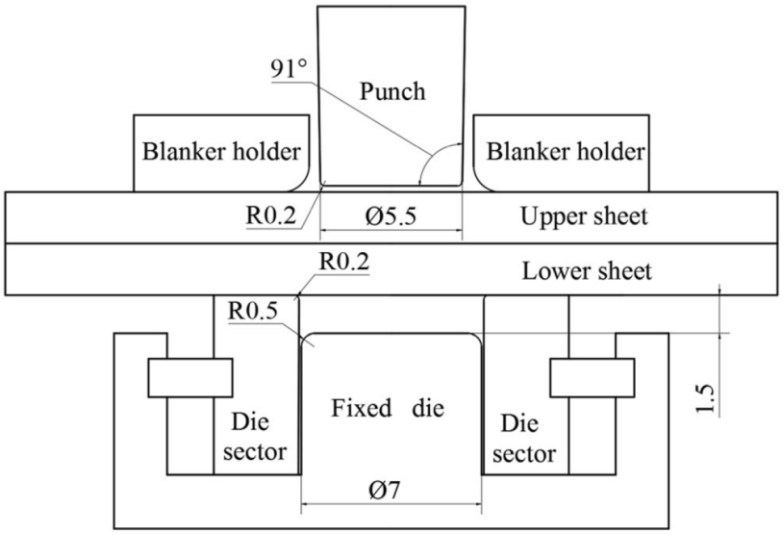

Fig. 2.14 Geometrical parameters of the extensible dies

The geometrical parameters of the clinched joint have an essential effect on the mechanical properties of the clinched joint. As shown in Fig. 2.13, two main parameters of the clinched joint are neck thickness (t_n) and interlock (t_s). The neck thickness and interlock are difficult to measure without the damage to the joint. So the bottom thickness (X) of the clinched joint was always taken as the measurable factor to evaluate the quality of the joint. The bottom thickness can be measured easily with no damage to the joint.

In the mechanical clinching process, the punch was driven by the clinching machine to move downward to press the AL5052 sheets with a speed of 0.5 mm/s. The control mode of the clinching machine was set to “controllable displacement.” So the displacement of the punch can

be controlled in the clinching process to get different bottom thicknesses. Different bottom thicknesses of the clinched joints represent different geometrical parameters. The clinched joints with different bottom thicknesses were produced in the mechanical clinching process. The bottom thicknesses of the clinched joints were set to 1.4, 1.5 and 1.6 mm, respectively.

As shown in Fig. 2.15, after the mechanical clinching process, the clinched joints with different bottom thicknesses were reshaped by a height-reducing method. A bumped die and a flat die were used to conduct the height-reducing process. The bumped die was taken as the lower die, and the flat die was taken as the upper die. The geometrical parameters of the bumped die used in the reshaping process are shown in Fig. 2.16. The geometrical parameters of the bumped die have been optimized. Orthogonal design was used to optimize the geometrical parameters of the bumped die. The best combination of geometrical parameters of the bumped die was gotten by simulating many groups of different combinations.

The height-reducing process was carried out on a hydraulic servo press. The force of the hydraulic servo press can be controlled precisely. The clinched joint was placed between the bumped die and the flat die. Whether or not the bumped die and the flat die are on the same axis has little effect on the height-reducing process, which is one of the advantages of the height-reducing method.

The pit of the clinched joint was placed on the bump of the bumped die which was used to fix the clinched joint. The bumped die was fixed, and the flat die was driven by the hydraulic servo press to reshape the clinched joint with a speed of 0.05 mm/s. The force of the hydraulic servo press was set to 25 kN. When the height-reducing force was increased to reach the setting force of the hydraulic servo press, the hydraulic servo press was stopped at once.

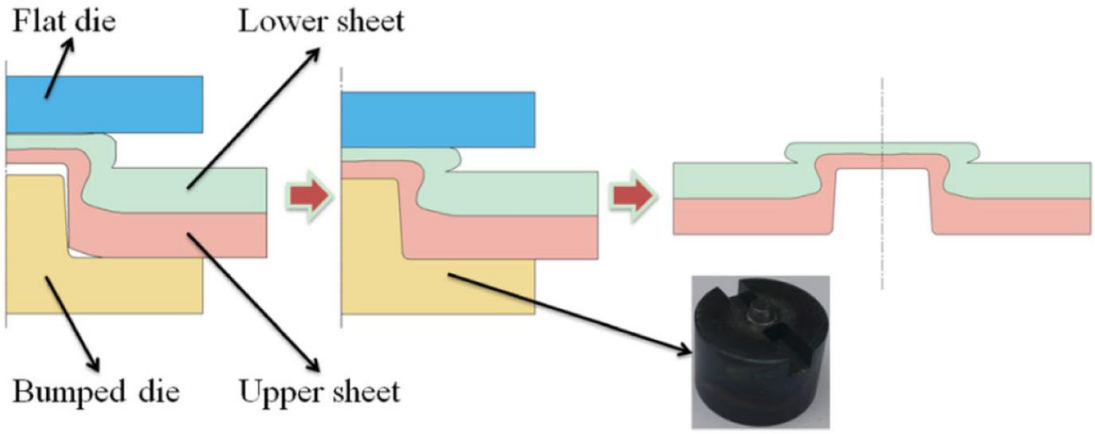

Fig. 2.15 Height-reducing process

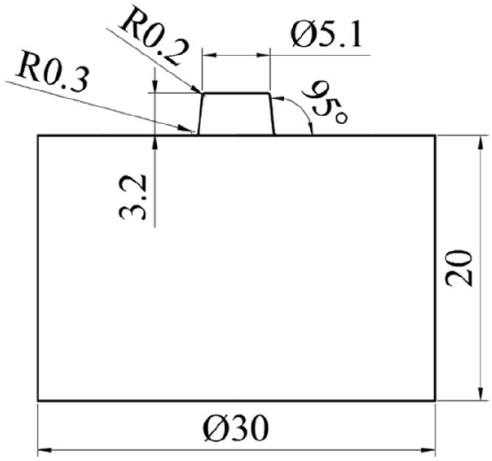

Fig. 2.16 Geometrical parameters of the bumped die

Fig. 2.17 shows the results of the height-reducing joint process. In the height-reducing process, the protrusion was compressed by a pair of dies. The material of the protrusion was compressed to flow to the neck of the joint. With the bump on the surface of the bumped die to support the neck of the joint, some material of the protrusion could flow downward to be gathered at the neck. The neck thickness was increased by the material flow of the protrusion. With the increase of the neck thickness, the cross-tensile strength and energy absorption of the joint were also increased.

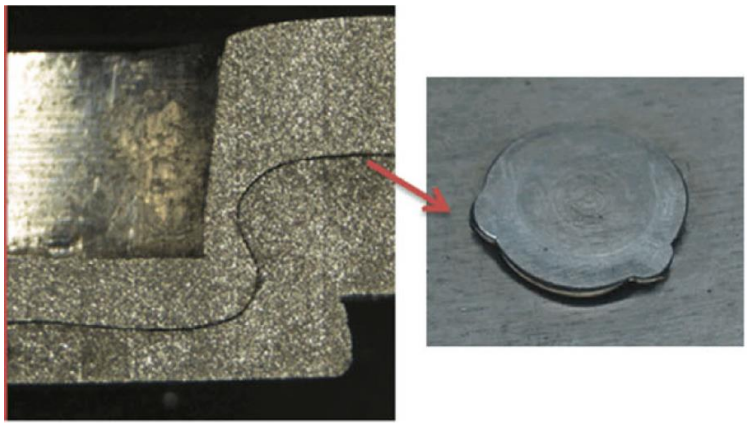

Fig. 2.17 Results of the height-reducing joint process

Although the height-reducing joint process shows a very good structure for the connection of aluminium sheets, it still faces some problems for the real application. The plastic joint process is very sensitive for the mechanical properties of the aluminium sheet. Sometimes, the height-reducing joint process is failed because the non-uniform composition of aluminium sheets. Fig.2.18 shows an example of the failure of the height-reducing joint process. The reason for the failure is the non-uniform composition of aluminium sheets leads to a decrease in the mechanical properties. When the joint process is applied to the non-uniform point, the connection can be broken easily because of the low mechanical properties.

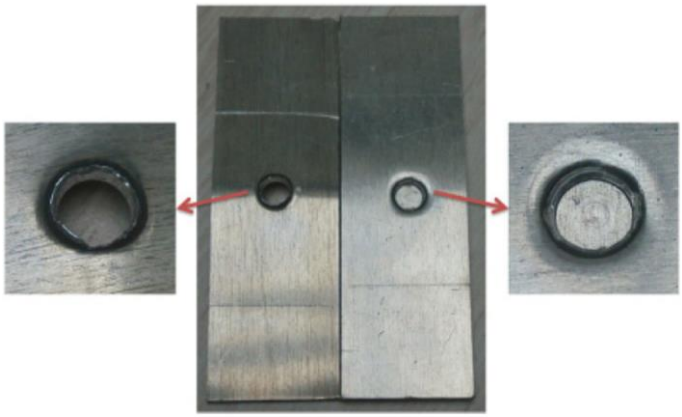

Fig. 2.18 Failure of the height-reducing joint process

Therefore the rapid composition analysis of aluminium sheets is very important for the quality of the plastic connection. In the real production, the height-reducing joint process can only be applied to the point in which the composition meets the requirement for the plastic joint process. Use this method, the failure problem which was mentioned in Fig. 2.18 can be solved. However, the traditional analysis methods usually need the sample preparation, complex devices and long analysis time. The traditional composition analysis can't be combined with the plastic joint process. It is gratifying that LIBS can be combined with the plastic joint process easily due to the features of no sample preparation, simple optical structure and short analysis time. The combination of plastic joint technique and LIBS technique can be used for the industrial production of automotive. Thus it is important for the real application that investigates and improves the performance of LIBS in the simulated conditions of the height-reducing joint process.

2.4 Online rapid analysis for the steel making process

It is well known that the iron and steel industry is one of the most important industries for human beings. In modern life, steel products are used almost everywhere. With the development of industry, high quality steel is desired in various fields. The advanced control methods for steelmaking process are required to meet these industrial demands. Elemental analyses of metals are one of the most suitable applications of LIBS and there have been many applications to measure elemental compositions of iron in an iron-making process. There are two approaches to applying LIBS to iron-making plants. One is the direct monitoring of raw ores or irons to optimize the process. The in situ characteristics of LIBS are actively utilized in these applications. The other is the detailed measurement of products as a product inspection. An inspection of segregation is one of these examples. LIBS has excellent time and spatial resolutions, and these features are suitable for these applications.

Fig. 2.19 shows an example of on-line monitoring in iron-making processes [159]. A LIBS unit was installed to analyze bulk minerals on a moving belt conveyer. There are several

drawbacks to analyzing bulk samples using LIBS because LIBS can only measure a small amount of materials located on the surface of bulk samples. If this small amount of material on the surface can represent bulk samples, LIBS is a good tool to measure these bulk samples.

Fig. 2.19(a) shows a photo of the measurement system [2]. The measurement configuration is almost the same as that of Fig. 2.19(b). The phosphate rock on the belt conveyer was analyzed using LIBS. The compositions of CaO, MgO, Fe_2O_3, and Al_2O_3 are the most important factors in phosphate analysis. These emission lines have often been used in other applications such as coal and ash analyses. The Nd:YAG laser at 1064 nm was used as a light source and the gated signals were detected with 1 μs delay time. Fig. 2.19(b) shows measurement results of five days continuous detection. It is clear that the fluctuation of elemental compositions can be detected by LIBS; these on-line data are important for advanced plant operations.

A rapid product inspection at the micro level is important to improve the control of steel-making processes. It is important to use measurement results for process adjustment during inspection time. Fig. 2.20 shows the 2-D distribution of carbon content on a metal surface measured by LIBS [55]. A photograph of the crystal structure revealed by sample polishing and etching is also shown in the figure. A photo-diode pumped Nd:YLF laser at 1047 nm was used as a light source and it was operated at 1 kHz to achieve fast scans of the measured area. A 4 × 1 mm2 area with a step size of 20 μm was measured in 2 min. The crystal structure photograph and the 2-D carbon map by LIBS show excellent agreement, showing the ferritic zone and the ferritic grain boundaries.

There are many other LIBS applications in various fields. LIBS is intrinsically an elemental analysis method, and it can be applied to industrial fields with a need for elemental analyses. One of the major drawbacks of LIBS is the difficulty of quantitative analysis. There are numerous correction methods for LIBS to achieve quantitative information; however, they are usually application dependent and there is no universal method applicable to all LIBS applications because of the complexities of plasma characteristics produced by the LIBS process. With this in mind, databases for LIBS in terms of quantitative analyses, which can be usable by not only spectroscopists but designers for various fields, will be important for the advancement of industrial applications. With these databases, engineers of various application fields can efficiently employ the LIBS technique. It is also important to understand that LIBS can be used for the molecular detection employing the “elemental fingerprint of a molecule.” It often happens that the elemental signal pattern of some molecules is unique and this pattern can be used to evaluate the target molecule. In these applications, such a systematic database is valuable.

Many of the LIBS applications have used pulsed lasers and ICCD detectors. Because of their high cost and vulnerability, it is rather difficult to use those laser systems for the control of industrial processes for long-term use. Lasers, especially, are not rugged enough to use them continuously for several years, which is often required in several industries. Therefore the advancement of lasers and detectors is crucial for these applications. Currently, portable LIBS

systems have been developed and applied to various fields. Portability of the system is important for many applications [160, 161]. The portable system is useful for large-area measurements. For example, monitoring of radioactive elements [162] in large areas becomes important in case of leakage of radioactive materials from a nuclear power plant. This has actually happened in the Japanese nuclear power plants in Fukushima in 2011. LIBS has the potential to cover these applications.

(a)

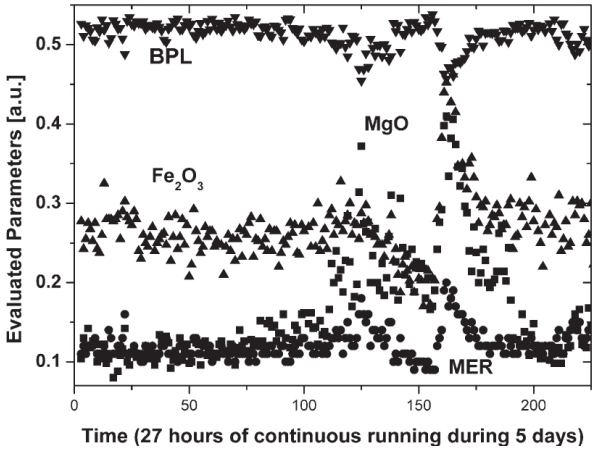

(b)

Fig. 2.19 On-line monitoring in iron-making processes. (a) A photograph of the LIBS system on movingbelt conveyer. (b) Measurement results of 5 days continuous detection. MgO (■), Fe2O3 (▲),BPL (▼), and MER (●) as functions of time during continuous run (total running time is 27 h) captured by the LIBS analyzer. Each analytical point results from averaging 300 laser pulses, laser energy is 40 mJ/pulse, laser frequency is 5 Hz, spectrometer settings for the delay from the laser pulse is 1 μs, and the acquisition time is 9 ms. In order to be at the same scale, the MgO concentrations were divided by 5, Fe2O3 concentrations by 4, and BPL concentrations by 120. BPL (bone phosphate of lime): a traditional reference to the amount (by weight percentage) of calcium phosphate contained in phosphate rock. MER = 2.185 [(Fe_2O_3 + Al_2O_3 + MgO)/BPL] [2]

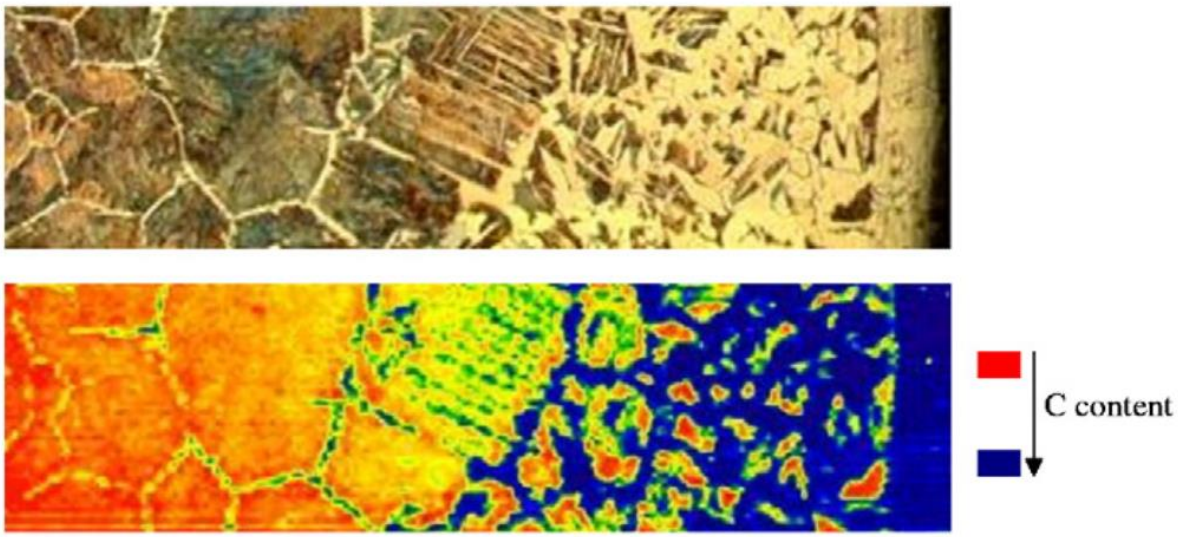

Fig. 2.20 2-D distribution of carbon content on a metal surface measured by LIBS. Comparison between the photographs of the crystal structure revealed by sample polishing and etching (top) and the C map generated by LIBS measurement on the same sample surface (bottom). [55]

2.5 Waste Disposal and Recycling Plant Applications

Waste disposal and recycling plants are important facilities to achieve a sustainable society. There are several places where LIBS can be applied to these plants [163-167]. For waste disposal and recycling processes, wastes are inputs to the processes and their compositions intrinsically fluctuate. Therefore it is important to know about the behavior of the waste composition to operate the system efficiently. There are also LIBS applications to monitor important elements during the disposing and recycling processes. These applications include wood recycling processes [163, 164], plastic waste management [165-167], and automobile catalyst recycling processes [168]. Platinum, palladium, and rhodium concentration has been measured in recycling processes of automobile catalyst scrap. Fig. 2.21 shows the measurement results of chromate copper arsenate (CCA) treated and untreated woods [163]. CCA is a widely used preservative for woods. CCA-treated woods contain high levels of chromium, copper, and arsenate, and the separation of CCA-treated woods from normal (untreated) ones has been necessary for clean recycling of woods. LIBS can detect the elemental contents of CCA and it is possible to distinguish CCA-treated and untreated woods using LIBS.

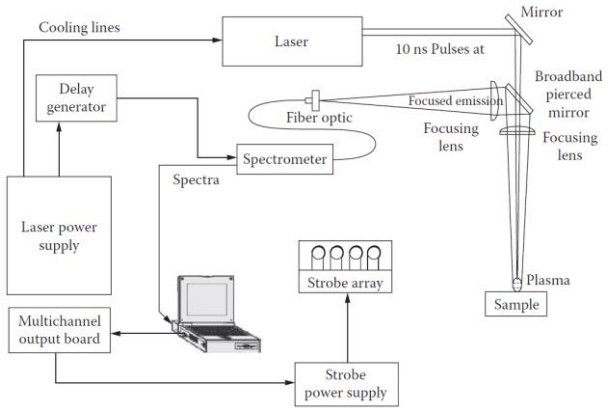

(a)

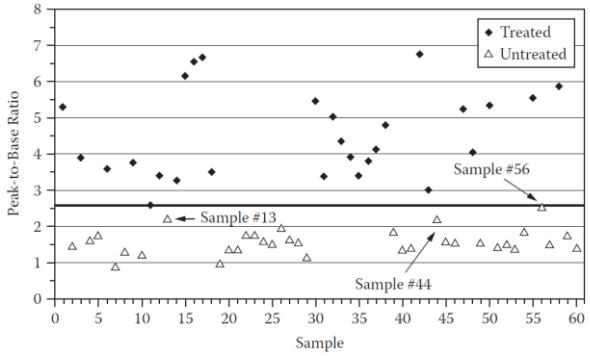

(b)

Figure 2.21 Measurement results of CCA-treated and untreated woods. (a) Schematic diagram for final LIBS system; (b) Measurement results of CCA-treated and untreated woods showing the ability of LIBS to detect treated and untreated wood using a peak-to-base ratio of 2.6 (10-shot average). [163]

2.6 Analysis requirements from other industrial fields

Application requirements of LIBS have also occurred in many industrial fields, including analyses from food to nuclear materials. Since LIBS is a method to analyze elemental compositions, industrial fields with a need for elemental analysis are potential LIBS applications [169]. As for LIBS application to foods and water [170-172], measurements of compositions or contaminations have been demonstrated in flours, wheat, barley, and water. Soils [173] and minerals [174] are among applications of LIBS. Many elements such as Mg, Al, Cu, Cr, K, Mn, Rb, Cd, and Pb have been measured by LIBS. LIBS has been also applied to the safety and security fields [175, 176], including explosives [177].

3 Fundamental of Laser-Induced Breakdown Spectroscopy

Laser-induced breakdown spectroscopy (LIBS) was studied as a rapid analysis method for the industrial applications. In this chapter, the principles and configurations of LIBS were clarified as follows. The intention is to give a brief overview of the fundamental of LIBS.

3.1 Theory of Laser-Induced Breakdown Spectroscopy (LIBS)

In the LIBS process, a laser beam is focused into a small area, producing hot plasma. The material contained in the plasma is atomized and the light corresponding to a unique wavelength of each element is emitted from excited atoms in the plasma, as shown in Fig. 3.1.

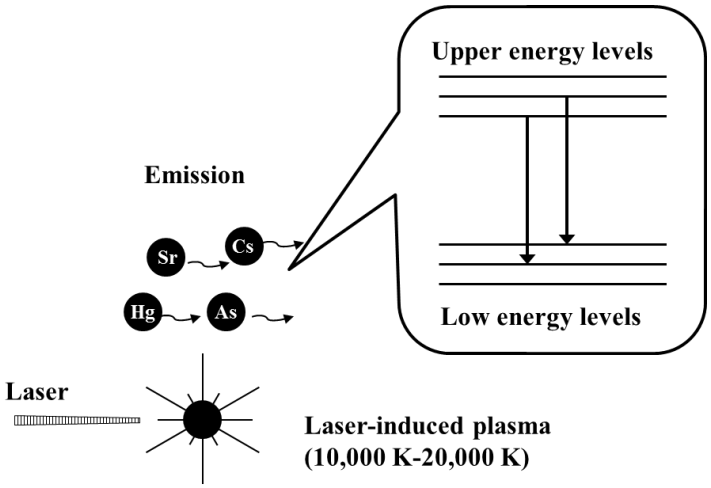

Fig. 3.1 Laser-induced plasma process

The interaction between pulsed laser beam and sample material, the plasma generation process and evolution process could be illustrated by Fig. 3.2 schematically. A pulsed laser beam is focused onto the surface of a substance to be analyzed, see (1) in Fig. 3.2. Radiation energy is locally coupled into the material (2) and the material starts to evaporate (3). Within this material vapor and the surrounding gas atmosphere a plasma is generated (4), leading to the excitation of the material constituents and their spontaneous emission of radiation. The plasma decays and emits element-specific radiation (5)–(7). This emission is resolved spectrally and is detected by a spectrometer. For solid substances, a crater is formed finally (8). The evaporated material is removed partially from the interaction zone driven by the intrinsic dynamics of the plasma expansion and by an externally impressed gas flow.

The process denoted in phase (3) as “evaporation” is a simplified description and refers to solid inorganic substances. In general, there is no pure sublimation from the solid phase to the gaseous phase. Depending on the laser parameters- e.g., the pulse duration- and the material properties a transient liquid phase may also exist. Besides the evaporation and dissociation processes also particles are ablated, e.g., small particulates or droplets, which are ejected due to

the impact of the pressure exerted by the plasma and the accompanying shock waves on a melt layer [1]. For organic substances, the initial material is disintegrated, fragmented, and dissociated.

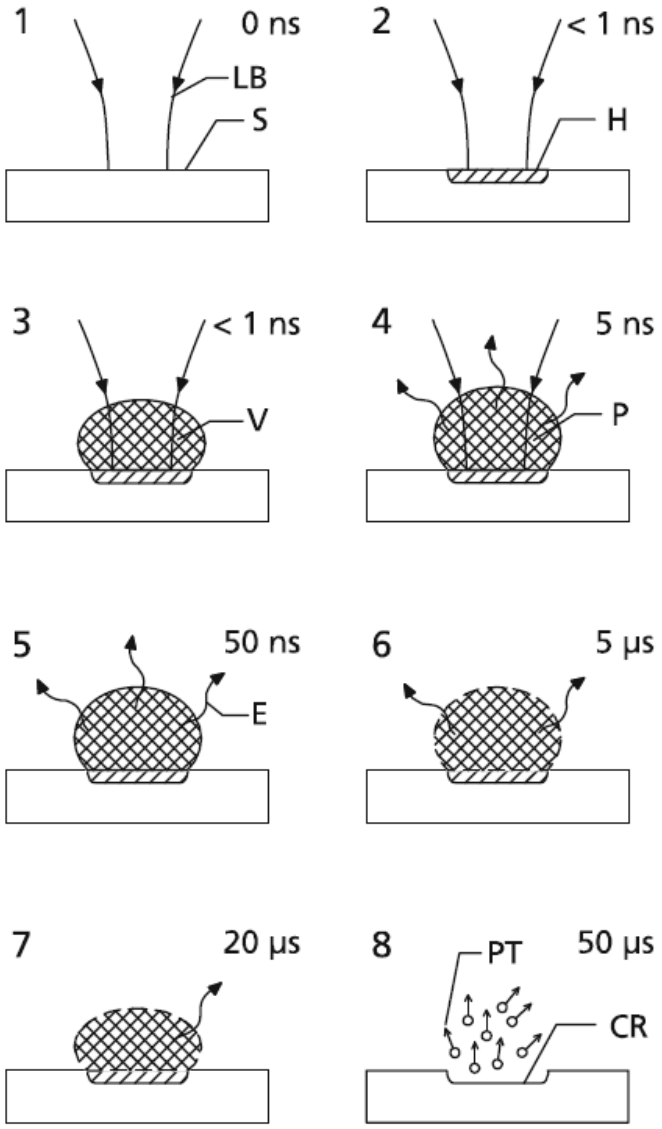

Fig. 3.2 Principle of laser-induced breakdown spectroscopy shown in phases 1–8; LB means incoming laser beam, S means sample, H means region of energy deposition, V means material vapor, P means plasma, E means element-specific emission, CR means crater, PT means particles. The times given depict the temporal evolution after start of irradiation of the laser pulse

The life time of the plasma depends on the laser beam parameters chosen, the conditions of the surrounding gas atmosphere, and the substance to be analyzed. The life time lies typically in the range of 0.5–10 µs. The whole process depicted in Fig. 3.2 can be repeated with frequencies of 10Hz up to 1 kHz.

Fig. 3.3 shows schematically some of the measuring parameters and the spectrum emitted from the plasma. The incident laser irradiance $I^{i}_{\lambda_L}(t)$ at the wavelength λ_L is a function of time (the spatial dependence is not discussed here). The temporal structure of the laser pulse has a decisive influence on the generated plasma states and hence the emitted spectrum. The quantity Δs describes the position of the beam waist of the laser beam in relation to the sample surface for a solid or a liquid measuring object. A part of the incident irradiance of the laser beam is reflected by the sample and the plasma in the backward direction, and the other part is scattered in various directions. These intensities are denoted with $I^{r}_{\lambda_L}$ and $I^{s}_{\lambda_L}$. Besides the irradiance $I^{i}_{\lambda_L}(t)$, the ambient gas pressure p_g and the type of the ambient gas have an influence on the plasma dynamics. The emitted spectrum of the plasma $I_{\lambda}(t)$ is also a function of time. Fig. 3.3, bottom right, shows schematically a spectrum detected at a time t_{delay} with respect to the irradiation time of the laser pulse and integrated for a duration of t_{int}.

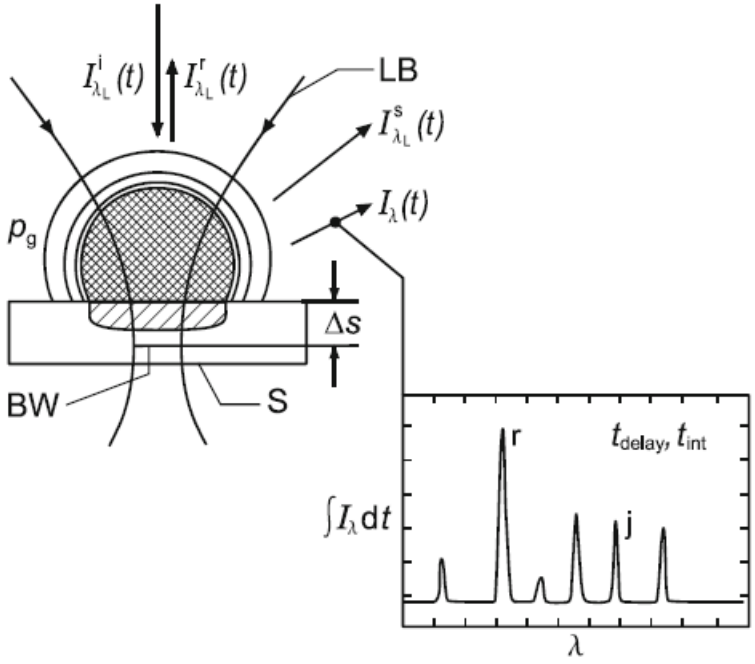

Fig. 3.3 Schematic illustration of some measuring parameters and the emitted spectrum; LB means incident laser beam, S means sample, BW means beam waist, $I^{i}_{\lambda_L}(t)$ means irradiance of the incident laser beam, $I^{r}_{\lambda_L}(t)$ reflected laser irradiance, $I^{s}_{\lambda_L}(t)$ means scattered laser irradiance, p_g means ambient gas pressure, Δs means beam waist position, *j* means emission line of an analyte, *r* means emission line of a reference line, t_{delay} means delay time between the laser pulse and the start of the integration window to record the spectrum, t_{int} means width of the integration window

During the life time of the plasma the emission spectrum changes. Fig. 3.4 illustrates schematically emission spectra of the laser-induced plasma for three different time delays after

the irradiation of the laser pulse. At the time t_1, the plasma emits predominantly a continuous spectrum, caused by free–free transitions of electrons. Only small peaks of the line intensities of atoms and ions are visible, and the ratio of the peak intensity of an emission line to the neighboring intensity of the spectral continuum emission is low. At the time t_2, the plasma has cooled down and the intensity of the line emission, as well as the ratio peak intensity to continuous background, increases significantly. At t_3, the plasma temperature decreases further and the emission intensities decrease.

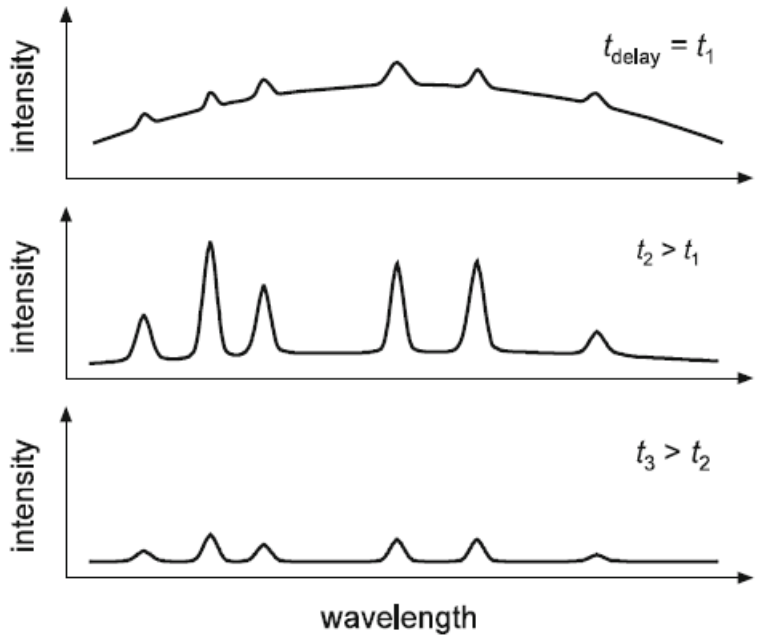

Fig. 3.4 Schematic illustration of the emission spectra of the laser-induced plasma for different time delays with respect to the irradiation of the laser pulse

A calibration of the LIBS signal is necessary for quantitative analysis. Despite the fact that the LIBS processes involved are complex, the emission intensity from the atomized species can be described by the following equation with the assumption of uniform plasma temperature:[2]

$$I_i = n_i K_{i,j} g_{i,j} \exp\left(-\frac{E_{i,j}}{kT}\right) \tag{3-1}$$

In the above expression, I_i is the emission intensity of species i, n_i is the concentration of species i, $K_{i,j}$ is a variable that includes the Einstein A coefficient from the upper energy level j, $g_{i,j}$ is the statistical weight of species i at the upper energy level j, $E_{i,j}$ is the upper level energy of species i, k is the Boltzmann constant and T is the plasma temperature. Eq. (3-1) is applicable under the conditions of local thermodynamic equilibrium (LTE). In Eq. (3-1), there are several factors that affect the emission intensity I_i, including plasma temperature, plasma non-uniformity, and matrix effects, etc. The appropriate correction factors must be contained in $K_{i,j}$ to obtain quantitative results.

In LIBS one of the emissions in Eq. (3-1) is often selected for the elemental composition measurement. In this case $n_{(i)}$ can be recast in the form:

$$n_{(i)} = \frac{I_{(i),j}}{K_{(i),j} g_{(i),j} \exp\left(-\frac{E_{(i),j}}{kT}\right)} \tag{3-2}$$

There are several forms in which plasma correction terms can be put into Eq. (3-2). In this study, with the matrix effects considered, the following equation can be used for the quantitative analysis of the surface compositions.

$$n_{(i)} = K_{(i)} \left(I_{(i),j}\right)^{b_0} \prod_{i1} \left(\frac{I_{(i1),j1}}{I_{(i1),j2}}\right)^{b_{(i1)}} \tag{3-3}$$

where $K_{(i)}$ and b_0 are correction factors of species i, and $b_{(i1)}$ is the temperature correction factor in the emission pair of $I_{(i),j1}$ and $I_{(i),j2}$.

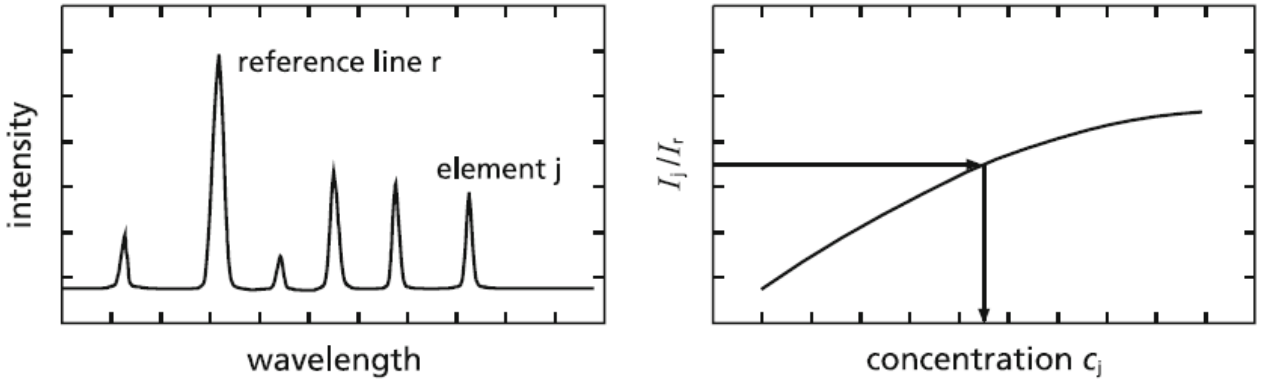

Fig. 3.5 Left: emission spectrum of laser-induced plasma with analyte and reference line. Right: calibration curve.

Fig. 3.5 illustrates the procedure for a quantitative measurement. The left diagram shows a spectrum $S(\lambda)$ with a number of emission lines depending on the composition of the sample to be analyzed. The spectral position of the lines has to be allocated to the respective elements on the basis of literature data as, e.g., those given in [1]. The height of a line is a measure of the concentration of the respective element in the sample. However, this line intensity depends also on a number of other factors, e.g., the laser pulse energy, plasma temperature, plasma size, atomic parameters of the line transition, sample surface, detector response function. Generally, the influence of these factors can be reduced by taking the ratio of the intensity of an analyte line j to the line intensity of a dominant element r of the sample, a so-called matrix element. This line acts as an internal standard or reference. To gain quantitative results, the spectral signals have to be calibrated using a set of samples with known chemical composition, e.g., certified reference samples (CRM). Fig. 3.5, right, shows a calibration curve where the intensity ratio I_j=I_r is plotted

as a function of the concentration c_j of these reference samples. In general, the calibration curve shows a nonlinear behavior. For an unknown sample, the intensity ratio I_j/I_r is measured, yielding the concentration of the analyte via the analysis function (also called working curve) which is the inverse function of the calibration curve (for simplicity, this step is illustrated by the arrows in Fig. 3.5, right).

3.2 Typical configuration of LIBS and measured signals

A typical geometric arrangement of LIBS is shown in Fig. 3.6. Lasers such as a pulsed Nd:YAG laser are used as a light source, and laser light is focused to the measurement point to make plasma. The emission signals from the plasma are collected and measured by a spectrometer. An image-intensified charge-coupled device (CCD) camera is mostly used to cut out unnecessary light (usually black-body-like emissions) from the hot plasma. It is worth noting that the reflection of a laser light from windows must be considered carefully. Because LIBS uses a high-energy laser light, its reflection often causes damage to optics. The reflection from plasma is sometimes tricky and malicious for LIBS systems. Plasma absorbs light and also reflects it. Damage to optics by the reflection from plasma causes troubles in some cases, especially in analyses of liquids.

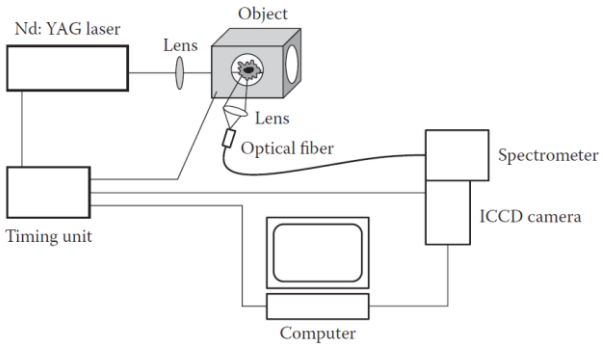

Fig. 3.6 Typical geometric arrangement of LIBS. Main components of a LIBS system are a laser, a spectrometer, and a CCD camera. A LIBS signal is highly dependent on the plasma temperature, which means it depends on the delay time from the laser input. An ICCD camera is mostly used to select the preferable delay time for a measurement element.

Fig. 3.7 shows the LIBS plasma evolution during creation and cooling processes of plasma. In the generation of plasma, the core of plasma is created by the absorption process of laser energy, such as multiphoton ionization in solids, liquids, or gases. The creation of the plasma core induces the rapid growth of plasma through the absorption of the laser light by electrons in it. After the extinction of the laser energy input, the plasma continues expanding because of its high temperature and pressure. At the same time, recombination of electrons and ions proceeds and temperature decreases gradually compared to the plasma generation process. LIBS signals arise in this plasma cooing period; the delay time, which corresponds to plasma temperature, is an important parameter for LIBS measurements. The black-body-like emission, which causes the

background noise, also appears depending on its plasma temperature, and there is an appropriate delay time, that is, in the plasma temperature to get a maximum signal-to-noise ratio. Generally, the shorter delay time is chosen in emissions from higher energy levels, and the longer delay time in those from lower energy levels.

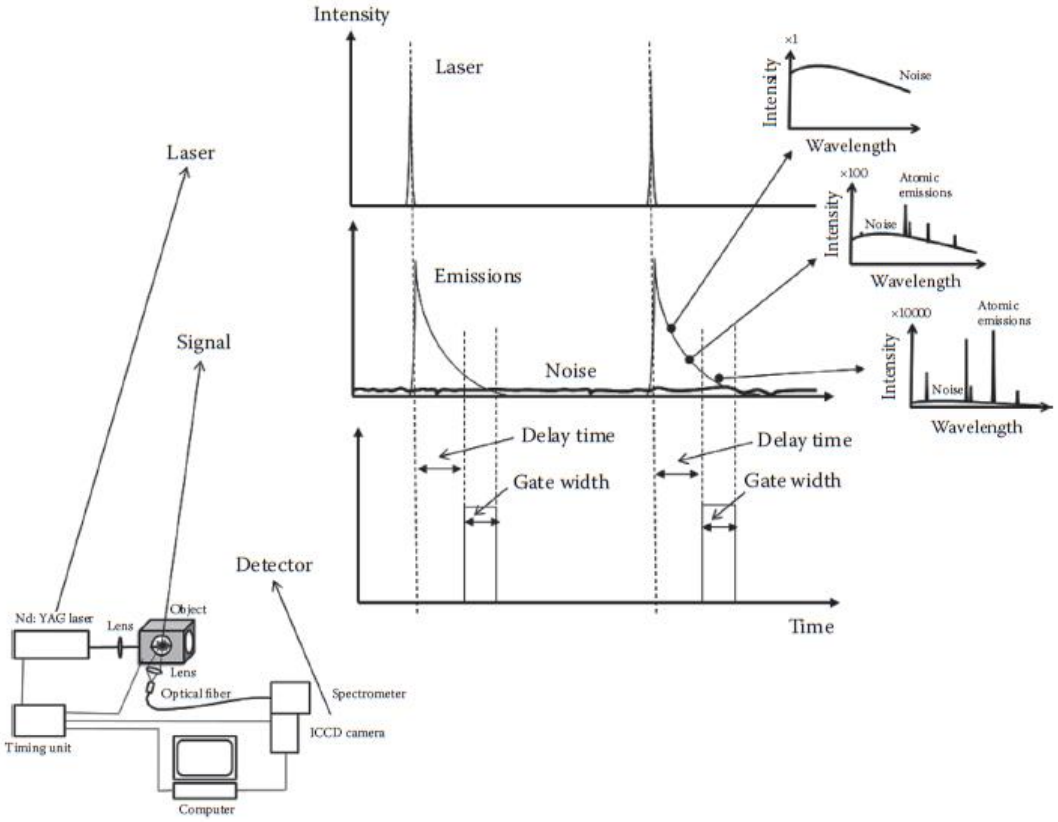

Fig. 3.7 LIBS timing chart. After the extinction of the laser energy input, the plasma continues expanding because of its high temperature and pressure. At the same time, recombination of electrons and ions proceeds and temperature decreases gradually. LIBS signals arise in this plasma cooing period; the delay time, which corresponds to plasma temperature, is an important parameter for LIBS measurements.

The LIBS signal intensities are illustrated in Fig. 3.8. Hg element is chosen as an example [178]. There are several emission lines just in one atom, and the identification of the emission lines is one of the most important tasks for LIBS. In practical applications, emissions are commonly attributed to more than 10 atoms. It is clear that emission intensities are much bigger at high temperature and tend to decrease according to temperature. Decrease rates depend on upper-level energies. As shown in Fig. 3.8, the lower the energy, the slower the decrease. The black-body-like background emission also has temperature dependence, and it is this feature that stipulates the signal-to-noise ratio. The signal-to-noise ratio tends to become better by employing an appropriate delay time, that is, in the plasma temperature.

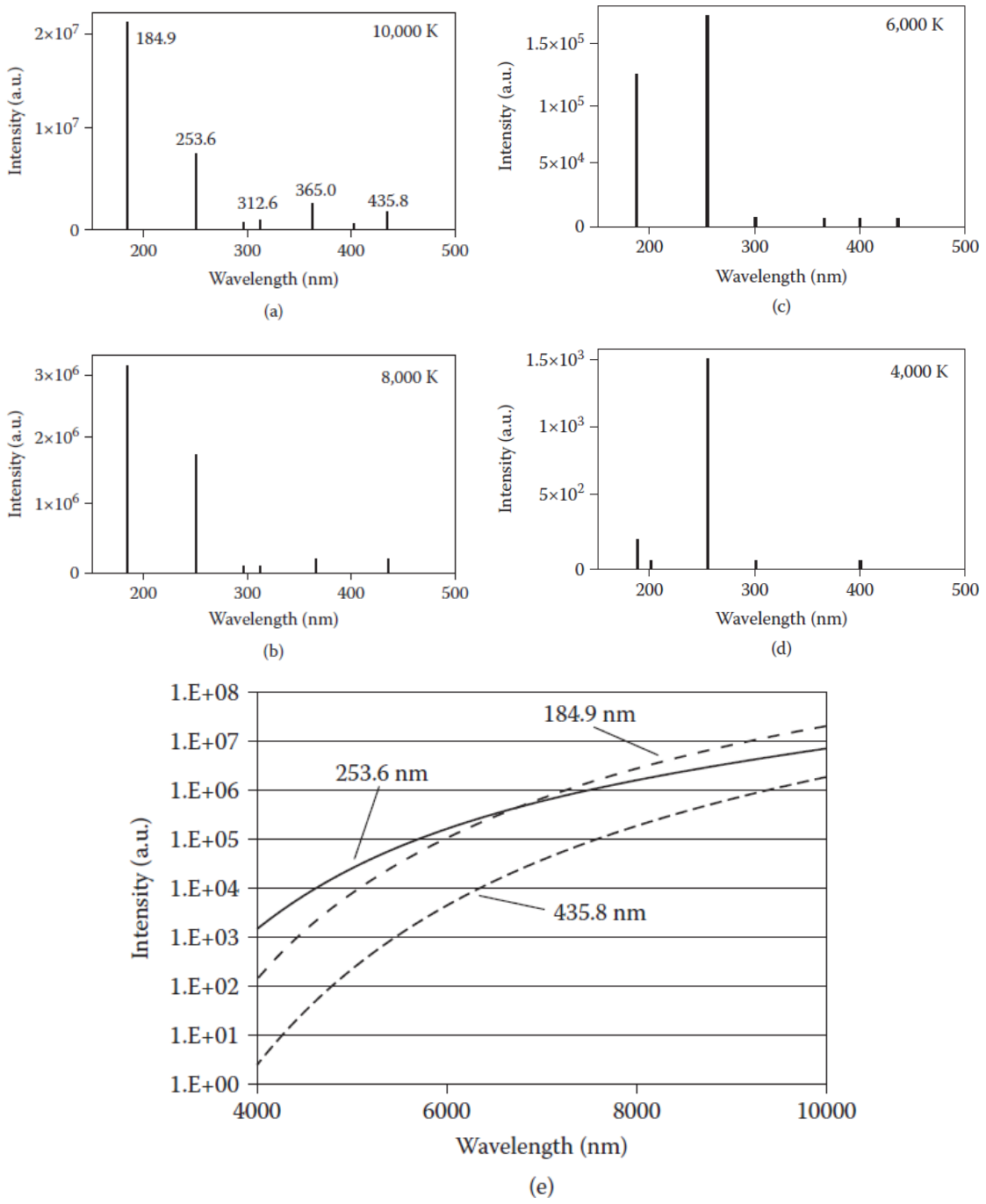

Fig. 3.8 The LIBS signal intensities of Hg. There are several emission lines just in one atom, and the emission intensity of each line has strong temperature dependence. Choosing appropriate delay time and gate width is important to get a maximum signal-to-noise ratio. Generally, the shorter delay time is chosen in emissions from higher energy levels, and the longer delay time in those from lower energy levels. The upper energy of each emission line is 54,068 cm^{-1} at 184.9 nm, 39,412 cm^{-1} at 253.6 nm, 71,396 cm^{-1} at 312.6 nm, 71,431 cm^{-1}

at 365.0 nm, and 62,350 cm^{-1} at 435.8 nm. Hg emission intensities at (a) 10,000 K; (b) 8,000 K; (c) 6,000 K; (d) 4,000 K. (e) Temperature dependence on each emission line.

3.3 Long-short double-pulse LIBS configuration

In this work, a long pulse width laser is applied to the laser-induced plasma process in order to improve the plasma condition. The long pulse width laser means that the laser duration time is long but the peak power is low. More specifically, a nanosecond Nd: YAG laser, which was operated at free running (FR) mode, was employed to generate a 1064 nm wavelength and 60 μs pulse width (FWHM) laser beam. Fig. 3.9 shows a clear explanation of the collinear long-short dual-pulse method, meanwhile the diagrams of traditional collinear LIBS methods are also provided. Using SP-LIBS, as shown in Fig. 3.9(a), the plasma is generated by short pulse width laser within a few nanoseconds or a dozen nanoseconds. Once the laser energy shut down, the plasma's temperature continuously decreases until it dies out. It is obvious that the plasma distribution is usually non-uniformly distributed spatially and temporally during the LIBS signal measurement period. The traditional collinear DP-LIBS method, which uses two short pulse width laser beams to generate the plasma, was proposed to increase the plasma temperature and lifetime, as shown in Fig. 3.9(b). Using the traditional DP-LIBS, the plasma temperature and life time had been enhanced indeed. The plasma was formed apart from the surface of target and expand to a globe shape [32, 41]. However, the plasma condition is still non-uniform and unstable because of the violent energy supply of second short pulse width laser beam. The second beam makes the LIBS process more complex since the energy of second pulse can be absorbed by the plasma, which was generated by the first pulse, and also can generate new plasma from the surface of target. It seems too difficult to establish a perfect physical-mathematical model which can describe the DP-LIBS process. Even setting up an approximation model is not simple at all. The plasma conditions still fluctuant using the traditional DP-LIBS method.

The collinear long-short DP-LIBS method was developed to generate a more uniform and stable plasma, as shown in Fig. 3.9(c). A long pulse width laser beam is focused on the surface of target before the short pulse width laser irradiation. The peak power of long pulse width laser was controlled under the minimum power which can generate noticeable plasma. The long pulse width laser beam is expected to remove the loose surface layer and heat the surface to a certain temperature. When short pulse width beam radiates in the middle of duration time of long pulse width laser, the plasma is generated on the cleaned and pre-heated surface, which means the elements composition on the surface is more close to that of the target and the plasma can also be produced at the same surface condition. Moreover, once plasma was generated, the long pulse width laser beam continuously irradiates the plasma region and provides a soft energy supply during the plasma cooling process. Thus the plasma becomes stable for a certain time and the temperature is maintained at a higher level. With a suitable delay time, the plasma temperature is

considered to be approximately constant, which is very different from that of traditional DP-LIBS.

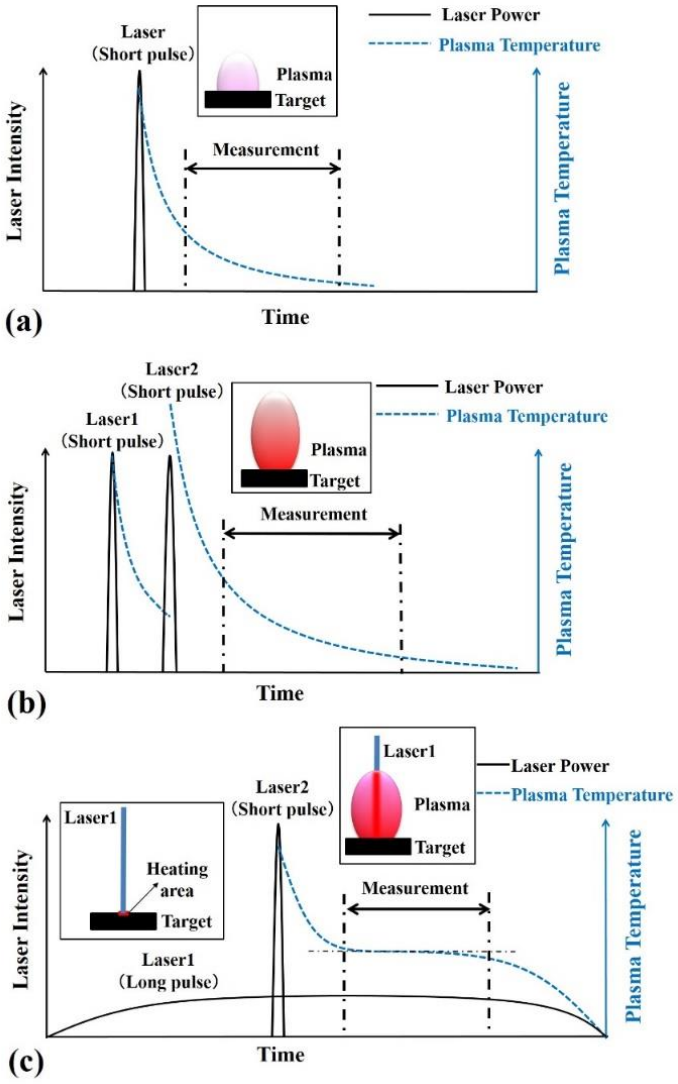

Fig. 3.9 Schematic diagram of LIBS methods. (a) SP-LIBS, (b) traditional DP-LIBS and (c) long-short DP-LIBS.

It has a positive effect on the plasma condition adding the radiation of long pulse width laser. During the plasma cooling process, the long pulse width laser beam continuously supplies energy for the hot plasma region. Thus the temporal and spatial non-uniformity is modified by the long pulse width laser. The plasma is considered to be maintained at a higher temperature and more stable condition without obvious undesirable influence. Table 3.1 shows the comparison of merits between different LIBS method [12-21, 25-29]. The collinear long-short DP-LIBS not only possesses all of the merits of traditional collinear DP-LIBS but also keeps the LIBS process in a single plasma generation condition.

Table 3.1 Comparison of merits between different LIBS methods

Merit	SP-LIBS	Traditional collinear DP-LIBS	Collinear long-short DP-LIBS
Signals enhancement	–	○ [12-21]	○ [57]
SBR enhancement	–	○ [13,17,19]	○ [57]
Low RSD	–	○ [13,18]	○ [57]
Target heating effect	–	○ [21,26-28]	○ [57]
Plasma re-heating effect	–	△ [16,19,20,25]	○ [57]
Pre-ablation effect	–	△ [27,28]	△ [57]
Single plasma generation	○	–	○ [57]
Plasma stabilization	–	–	○ [57]

Symbol "–" means "negative", symbol "○" means "positive" and symbol "△" means "still in discussion".

4 Experimental systems of long-short double-pulse LIBS

The employed experimental system of LIBS for the steel sample measurement in this study is illustrated as follows. The devices used for each experiments is explained in detail to present a clear explanation on the experimental setup. The information of the samples used in this study is also presented in this chapter as the reference information for the further discussion.

4.1 Experimental system for the analysis of solid steel samples

The experimental setup for long-short DP-LIBS configuration is illustrated in Fig. 4.1. As shown in Fig. 4.1(a), the measurement system was composed of two lasers, a digital delay generator, optical fiber, a spectrometer, an ICCD (Intensified Charge Coupled Device) camera and other auxiliary devices. The nanosecond laser 1 (LOTIS TII, LS-2137U, 6-8 ns, 10 Hz, beam diameter: 8 mm) was operated at 1064 nm and FR mode. The FR mode, which has been rarely used in LIBS, means the Q value of optical resonant cavity does not change during laser pulse formation. Thus the laser pulse can be sustained for dozens of microseconds with low peak power density. In this work, the pulse energy of long-pulse-width laser was set to 200 mJ with the pulse width of 60 μs. The pulse width was determined by an oscilloscope (Tektronix, MDO3014) with a Si photodiode sensor (Hamamatsu, S1336-18BQ). The nanosecond laser 2 (LOTIS TII, LS-2134UTF, 5-8 ns, 10 Hz, beam diameter: 6 mm) was operated at 1064 nm (Q-Switch, pulse width 5.4 ns) with the pulse energy of 20.5 mJ. The inter-pulse delay between the two pulses was adjusted by a digital delay generator (Stanford Research Systems, Model DG645) and was also verified by the oscilloscope. These two laser beams were combined using a polarization prism. The combination of the two laser beams is important for the collinear long-short DP-LIBS. In this study, the polarization prism was used to combine the two beams. The orthogonal components in short pulse and long pulse were reflected and transmitted by the prism respectively. The beam combination was realized by matching the reflection position and transmission position of the two beams. Then the combined laser beam was focused on the sample using a lens (focal length 800 mm). Moreover, the short-pulse-width laser, long-pulse-width laser and related optics can also be combined in one package for the industrial application, which has been done in our research group. The emission signals from the plasma were collected in the reverse direction and focused on the fiber entrance using a lens (focal length 100 mm). After delivered 10 meters by the optical fiber, the emission signals were detected by the combination of a spectrometer (SOL, NP-250-2M), an ICCD camera (Andor, iStar DH334T-18U-03). The delay time of ICCD was triggered by the short pulse. The detailed explanation of signal timing and the measured intensity shape of laser pulses were presented in figure 2 of Ref. [26].

The manganese with the matrix of iron was the measurement target in current study. Several reports suggest that the neutral lines of Mn and Fe in the range of 400-410 nm can be used for the quantitative analysis of Mn in steel matrix [27-29]. Therefore, the emission was detected in this range employing a grating with 3600 grooves/mm to obtain a relatively high resolution (0.0097 nm). In addition, the plasma morphology was studied in this work. ICCD coupled with a camera lens (Nikon, 602095, focus length 35 mm) and a band pass filter (Asahi Spectra, 405 nm, FWHM 10 nm) was employed to record the images of plasma, as shown in Fig. 4.1(b). Through the band pass filter, the emission images of plasma in the wavelength range of 400-410 nm were recorded. Accordingly, the recorded plasma images can be discussed with the spectra results in the wavelength range of 400-410 nm.

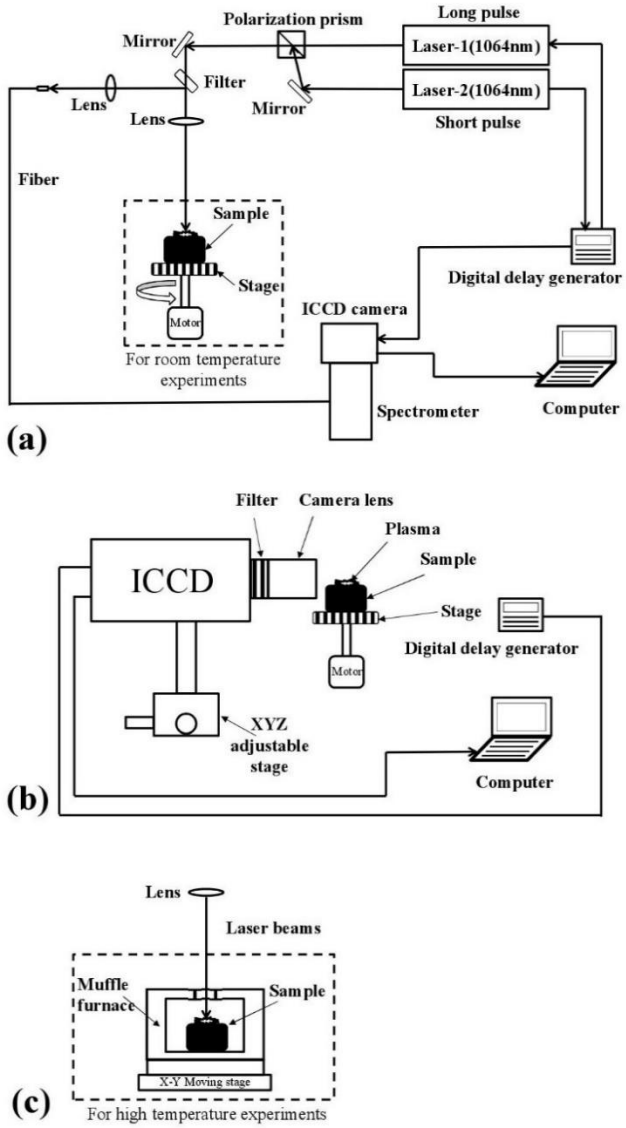

Fig. 4.1 Experimental setup. (a) Diagram of long-short DP-LIBS configuration, (b) setup for the study of plasma morphology and (c) diagram of the measurement in muffle furnace.

For the experiments at room temperature, the sample was fixed on a rotational stage. For the experiments at high temperature, a muffle furnace with a hole on the upper surface was employed to carry out the experiments. The sample was placed in the muffle furnace and heated to the specified temperature. After 30 minutes of heat preservation, the sample was measured by firing the laser pulses through the hole. During the measurement, the muffle furnace with the sample was kept moving through an X-Y moving stage, as shown in Fig. 4.1(c).

4.2 Experimental system for the analysis of liquid steel samples

In order to promote the long-short DP-LIBS method to the real industrial applications, a compact long-short double-pulse LIBS laser is designed to specially realize the new LIBS method. Fig. 4.2 shows the long-short DP-LIBS laser that is designed by our research group and manufactured by LOTIS TII co. ltd. Fig. 4.3 shows the optical diagram of the LS-2145LIBS laser.

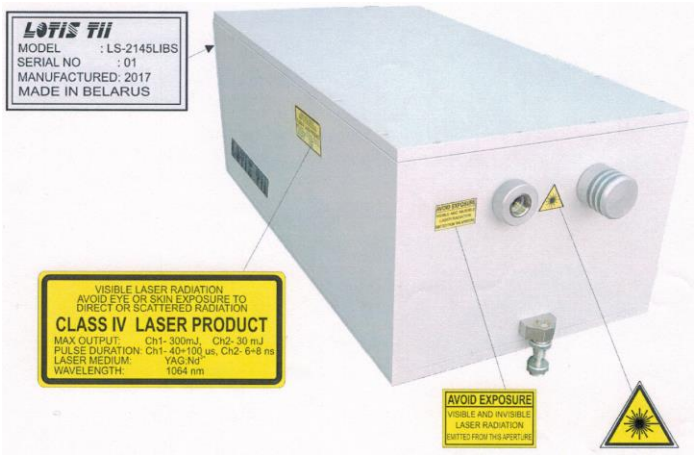

Fig. 4.2 Latest designed and manufactured laser for the long-short DP-LIBS method. (Model No. LS-2145LIBS)

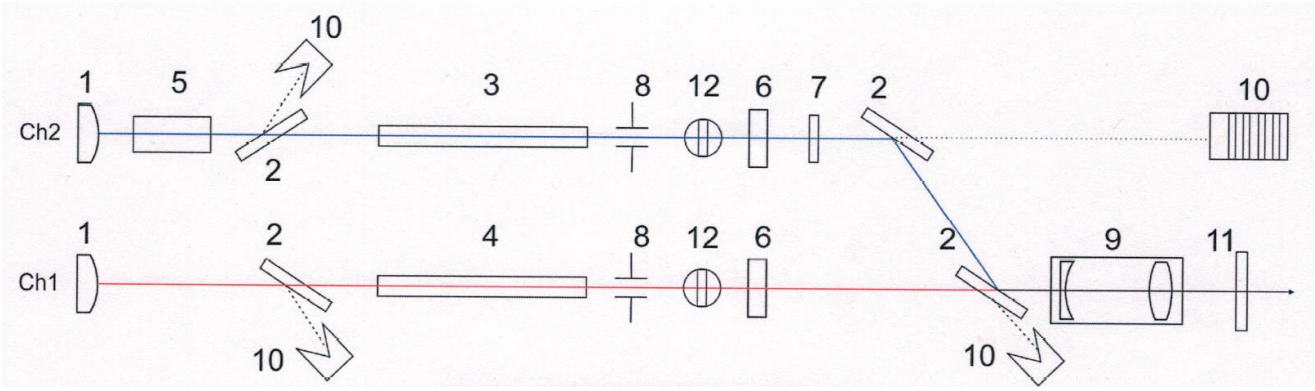

Fig. 4.3 Optical diagram of Laser LS-2145LIBS

1-Rear mirrors; 2-Polarizer; 3-active element of Channel 2; 4-active element of Channel 1; 5-Pockels cells (Q-switch); 6-Output mirrors; 7-λ/2 plate; 8-Intracavity pinhole; 9-External telescope; 10-Beam stop; 11-Protective output window; 12-Intrcavity shutter.

Based on the LS-2145LIBS laser, the study on the liquid steel samples were carried out in this work. A 15kW induction furnace was employed to supply the energy of the melting of steel samples. Fig. 4.4 shows the diagram of the experimental setup of liquid steel sample measurement. In addition, different standard steel sample were measured in this work, in order to avoid the pollution from the carbon container, which is used in induction furnace, the MgO cup were used to hold the molten steel. To obtain a basically consistent surface level, 60g of the original standard sample were used for each experiments in this work. The weight of the sample was examined by an electronic scales, as shown in Fig. 4.5.

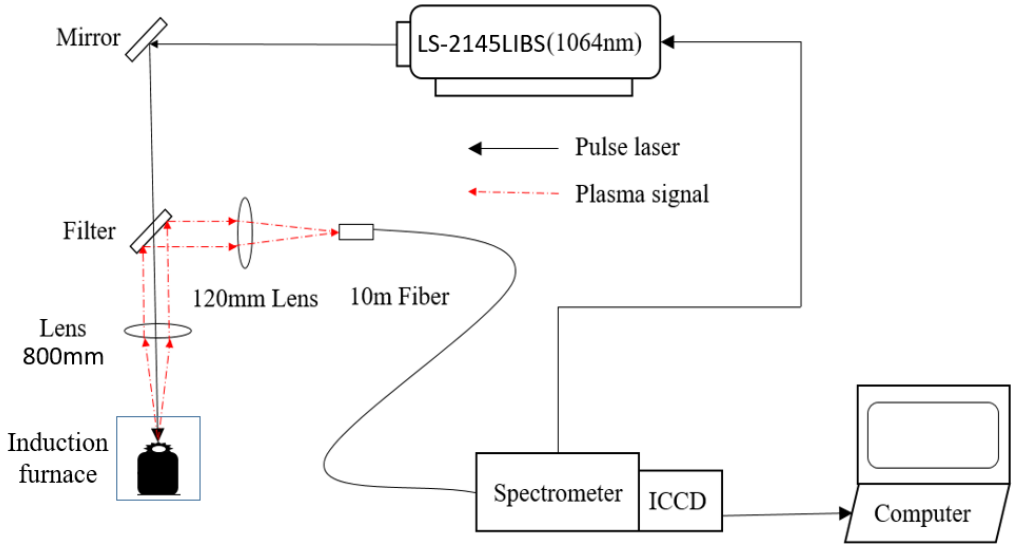

Fig. 4.4 Diagram of the experimental setup for the measurement of liquid steel.

The weight of MgO cup

The weight of MgO cup and 60g standard steel sample

Fig. 4.5 The examination of the sample weight that used for each experiments for the measurement of liquid steel using SP-LIBS and long-short DP-LIBS

4.3 Sample information

The standard steel samples were used in this study for the LIBS measurement. The samples were sold by Zhengzhou Research Institution of Mechanical Engineering (ZRIME) and with the certificate of the major contents. Fig. 4.6 shows the certificate of the samples that provided by the selling company.

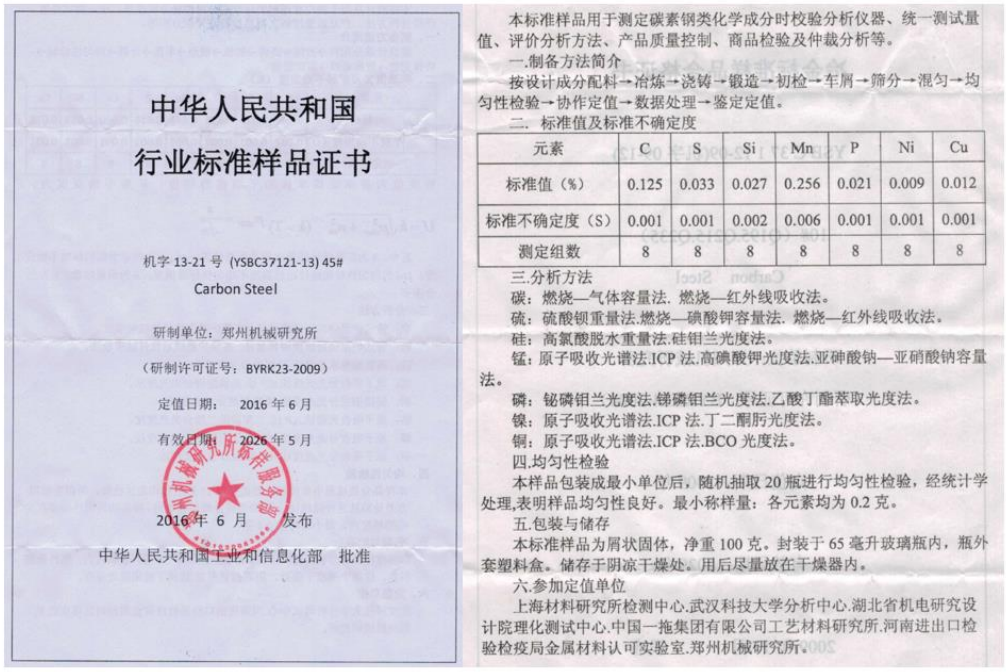

中华人民共和国

行业标准样品证书

机字 13-21 号 (YSBC37121-13) 45#

Carbon Steel

研制单位：郑州机械研究所

（研制许可证号：BYRK23-2009）

定值日期： 2016 年 6 月

有效日期： 2026 年 5 月

2016 年 6 月 发布

中华人民共和国工业和信息化部 批准

本标准样品用于测定碳素钢类化学成分时校验分析仪器、统一测试量值、评价分析方法、产品质量控制、商品检验及仲裁分析等。

一.制备方法简介

按设计成分配料→冶炼→浇铸→锻造→初检→车屑→筛分→混匀→均匀性检验→协作定值→数据处理→鉴定定值。

二. 标准值及标准不确定度

元素	C	S	Si	Mn	P	Ni	Cu
标准值（%）	0.125	0.033	0.027	0.256	0.021	0.009	0.012
标准不确定度（S）	0.001	0.001	0.002	0.006	0.001	0.001	0.001
测定组数	8	8	8	8	8	8	8

三.分析方法

碳：燃烧—气体容量法. 燃烧—红外线吸收法。

硫：硫酸钡重量法.燃烧—碘酸钾容量法. 燃烧—红外线吸收法。

硅：高氯酸脱水重量法.硅钼兰光度法。

锰：原子吸收光谱法.ICP 法.高碘酸钾光度法.亚砷酸钠—亚硝酸钠容量法。

磷：铋磷钼兰光度法.锑磷钼兰光度法.乙酸丁酯萃取光度法。

镍：原子吸收光谱法.ICP 法.丁二酮肟光度法。

铜：原子吸收光谱法.ICP 法.BCO 光度法。

四.均匀性检验

本样品包装成最小单位后，随机抽取 20 瓶进行均匀性检验，经统计学处理,表明样品均匀性良好。最小称样量：各元素均为 0.2 克。

五.包装与储存

本标准样品为屑状固体，净重 100 克。封装于 65 毫升玻璃瓶内，瓶外套塑料盒。储存于阴凉干燥处。用后尽量放在干燥器内。

六.参加定值单位

上海材料研究所检测中心.武汉科技大学分析中心.湖北省机电研究设计院理化测试中心.中国一拖集团有限公司工艺材料研究所.河南进出口检验检疫局金属材料认可实验室.郑州机械研究所。

Fig. 4.6 The certificate of the standard steel samples that sold by ZRIME

In this work, two kinds of standard samples were used for the experiments. Fig. 4.7 shows the bulk type samples which were used for the study of solid phase experiments. The major elements composition of the samples which were used for the solid phase study is also presented in Fig.4.7 which is summarized according to the certificate of ZRIME.

(a)

Name	C	S	Si	Mn	P	Cr	Ni	Fe
Pure iron	0.0032	0.0049	0.0031	0.032	0.0037	0.0053	0.016	99.7419
ZG10#	0.085	0.032	0.217	0.44	0.042	0.104	0.134	98.755
ZG25#	0.233	0.033	0.354	0.472	0.034	0.216	0.046	98.479
ZG45#	0.454	0.044	0.444	0.752	0.041	0.141	0.122	97.72
ZG60#	0.586	0.042	0.471	0.778	0.037	0.131	0.114	97.575
28CrNiMo	0.276	0.028	0.56	0.842	0.032	0.362	0.432	96.996
35CrNiMo	0.34	0.027	0.779	0.957	0.029	0.408	0.614	96.348
20MnMo	0.192	0.026	0.363	1.12	0.031	0.201	0.246	97.519
30SiMn	0.297	0.028	0.47	1.23	0.029	0.203	0.11	97.423
35SiMn	0.332	0.029	0.716	1.36	0.031	0.154	0.148	97.007

(b)

Fig. 4.7 The shape and composition of the bulk type standard steel samples. (a) The shape of the bulk type standard steel sample and (b) the composition of major elements in these steel samples.

For the experiments of liquid steel samples, the powder steel samples were used to carry out the relevant experiments. The surface level is important to obtain a good focus of the laser beam. Therefore, the weight of the original standard steel sample was examined for each experiments in the study of liquid steel measurement. Fig. 4.8 shows the shape of the powder steel samples before molten and after molten. The major elements composition of the samples which were used for the liquid steel study is also presented in Fig. 4.8

(a) (b)

Name	C	S	Si	Mn	P	Cr	Ni	Cu	Fe
10#Q195Q255Q235	0.125	0.033	0.027	0.256	0.021		0.009	0.012	99.517
10#Q195Q215Q235	0.083	0.026	0.117	0.306	0.025		0.017	0.013	99.413
8#Q195	0.083	0.031	0.173	0.426	0.049	0.24	0.2	0.24	98.558
15#Q215Q235	0.164	0.025	0.184	0.496	0.014		0.013	0.016	99.088
30#	0.308	0.031	0.232	0.517	0.026				98.886
25#	0.252	0.025	0.348	0.553	0.027	0.167	0.124	0.16	98.344
10#Q215Q235	0.134	0.037	0.315	0.606	0.036	0.086	0.102	0.142	98.542
45#	0.448	0.025	0.258	0.643	0.016	0.06	0.059	0.078	98.413
20Cr	0.233	0.017	0.356	0.683	0.023	0.907	0.084	0.124	97.573
65#	0.659	0.0074	0.275	0.742	0.012	0.107	0.056	0.113	98.0286
65Mn	0.664	0.012	0.23	0.938	0.026	0.123	0.042	0.067	97.898
27SiMn	0.245	0.016	1.24	1.27	0.026	0.276	0.084	0.022	96.76
16Mn	0.163	0.013	0.337	1.44	0.017	0.072	0.068	0.125	97.765

(c)

Fig. 4.8 The shape and composition of the powder type standard steel samples. (a) The shape of the powder type standard steel sample before molten, (b) the shape of the powder type standard steel sample after molten and (c) the composition of major elements in these steel samples.

5 Comparative study between conventional LIBS and long-short DP-LIBS

In order to certify the performance improvement of long-short DP-LIBS, the investigation on the differences between conventional LIBS and long-short DP-LIBS was carried out in this chapter. The technical parameters, such as absolute intensity, signal enhancement, plasma topography, plasma temperature were compared to clear the differences between conventional LIBS and long-short DP-LIBS.

5.1 Role of inter-pulse delay

It is reported in literature that the inter-pulse delay plays an important role in traditional DP-LIBS configuration as it influences the ablation efficiency and plasma cooling processes [30-32]. Accordingly, the inter-pulse delay between long pulse and short pulse is also vital for the long-short DP-LIBS. Fig. 5.1(a) shows the three major inter-pulse delays for the long-short DP-LIBS used in current study. For the case of inter-pulse delay = 0, the short pulse arrives at the beginning of the long pulse, therefore, the long pulse only affects the cooling processes of plasma. For the case of inter-pulse delay = 30 μs, the short pulse arrives at the middle of the long pulse, therefore, the long pulse obtains a combination effect of target pre-heating and plasma sustaining. For the case of inter-pulse delay = 60 μs, the short pulse arrives at the end of the long pulse, therefore, the long pulse only preheats the target. To investigate the role of inter-pulse delay in signal enhancement for the long-short DP-LIBS, the signal intensity were recorded according to different inter-pules delay in current study. Fig. 5.1(b) shows the role of inter-pulse delay in signal enhancement for the long-short DP-LIBS configuration. Signal intensity from long-short DP-LIBS was normalized to SP-LIBS. Generally, the signal enhancement of three spectral lines was presented. Overall the trend is same for all the three spectral lines. The peak of signal enhancement is observed at around the inter-pulse delay of 30 μs. Similar trend of signal enhancement in long-short DP-LIBS has also been observed by our group in the previous report [26].

Various mechanisms for signal enhancement reported in literature are also involved in long-short DP-LIBS arrangement, which include either pre-heating effect of target or the re-heating effect of plasma plume or a combination effect of both the mechanisms [21, 33]. The laser ablation process and plasma cooling process are significantly influenced by long-pulse-width laser beam. According to the results in Fig. 5.1(b), both these processes are directly related to inter-pulse delay between long pulse and short pulse. For very short inter-pulse delays, the long pulse mainly plays the role of plasma sustaining which means that the enhancement was mainly attributed to the absorption of laser energy by plasma. The energy of long pulse was absorbed by plasma plume according to the mechanisms include electron-ion inverse Bremsstrahlung, electron-neutral inverse Bremsstrahlung, and photoionization. All these processes are influenced by the number density of plasma [34]. Compared with SP-LIBS, the mass of laser ablation was

not obviously improved by long pulse in the case of short inter-pulse delays, therefore, the energy of long pulse can't be absorbed effectively because of low number density of plasma. For long inter-pulse delay, most of signal enhancement was caused by the increase in mass ablation. It has been showed in the results that the enhancement appears to decline in the case of long inter-pulse delay. This can be attributed to the limit of laser ablation efficiency. Due to the drilling effect, the mass ablation of laser pulse is hard to be increased when a relatively large mass ablation has been obtained [35]. Therefore, the limit of mass ablation and the rapid cooling process of plasma result in a smaller enhancement in the case of long inter-pulse delay. For the inter-pulse delays between short and long delay, signal enhancement could then be attributed to both the target pre-heating effect and plasma sustaining effect. It has been showed in Fig. 3b that the maximum enhancement was obtained around the inter-pulse delay of 30 μs. This result indicates that the optimal coupling can be obtained by firing the short pulse at the middle of long pulse. Therefore, the inter-pulse delay of 30 μs was used in current work to study the enhancement and stabilization of plasma in long-short DP-LIBS configuration.

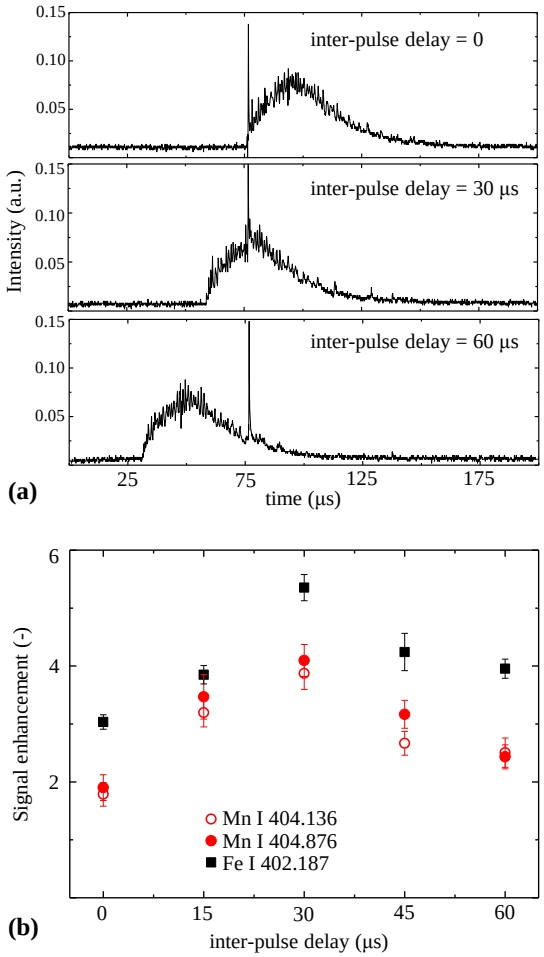

Fig. 5.1 Role of inter-pulse delay for long-short DP-LIBS configuration. (a) Measured pulse shapes for different inter-pulse delay and (b) signal enhancement observed for different

inter-pulse delay using long-short DP-LIBS with respect to SP-LIBS. Experiment conditions: gate width: 1000 ns, accumulation: 50 times, delay time: 3000 ns, SP-LIBS pulse energy: 20.5 mJ, DP-LIBS pulse energy: short pulse: 20.5 mJ, long pulse: 200 mJ (FR mode).

5.2 Signal enhancement

Fig. 5.2 shows the comparison of measured spectra using SP-LIBS, long-short DP-LIBS and long pulse LIBS respectively. Lots of emission lines of manganese and iron can be recognized from the spectra. Table 5.1 provides the information of these emission lines from the National Institute of Standards and Technology (NIST) database [36]. By observing the data of SP-LIBS and long-short DP-LIBS, it can be clearly seen that the signal intensity was enhanced in the long-short DP-LIBS condition. Enhancement in signal intensity of spectral lines with high excitation energies is considerable, which can be due to the high temperature of plasma in long-short DP-LIBS condition. Enhancement in signal intensity of spectral lines with low excitation energies is also observed although the enhancement is not as dramatic as for the spectral lines with high excitation energies. In addition, by observing the data of long pulse LIBS, it can be seen that there is no obvious spectrum. This result, as same as we expected, is due to that the peak power of the long pulse was lower than the breakdown threshold power which can generate a noticeable plasma. It suggests that the long pulse only affects the laser ablation process and the plasma cooling process without generating a new plasma. This is the most significant difference between the long-short DP-LIBS and traditional DP-LIBS.

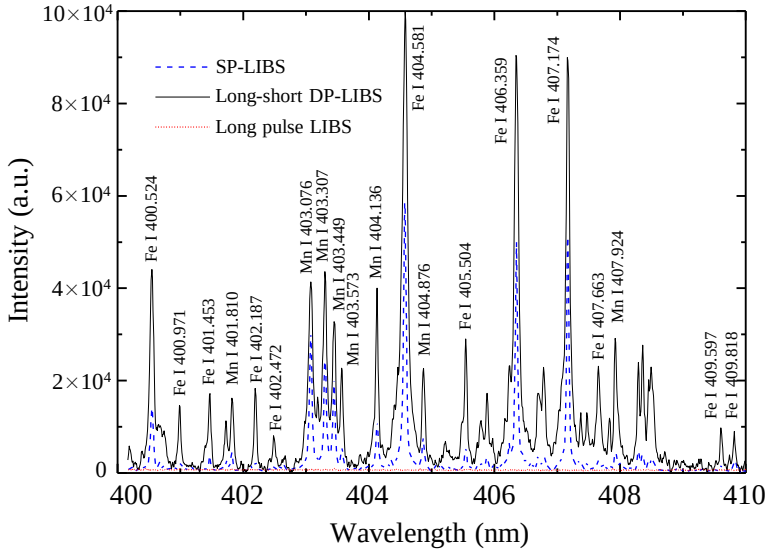

Fig. 5.2 Measured spectra of SP-LIBS, long-short DP-LIBS and long pulse LIBS. Experiment conditions: gate width: 1000 ns, accumulation: 50 times, delay time: 3000 ns, SP-LIBS pulse energy: 20.5 mJ, DP-LIBS pulse energy: short pulse: 20.5 mJ, long pulse: 200 mJ (FR mode), long pulse LIBS pulse energy: 200 mJ (FR mode).

Table 5.1 Fe and Mn specific atomic emission lines [31]

Spectral line (nm)	Lower level energy (cm^{-1})	Upper level energy (cm^{-1})	A (10^8 s^{-1})
Fe I 400.524	12560.93	37521.16	0.20
Fe I 400.971	17927.38	42859.78	0.05
Fe I 401.453	24574.66	49477.13	0.15
Fe I 402.187	22249.43	47106.48	0.09
Fe I 402.472	26140.18	50979.58	0.08
Fe I 404.581	11976.24	36686.18	0.86
Fe I 405.504	20641.11	45294.85	0.004
Fe I 406.359	12560.93	37162.75	0.67
Fe I 407.174	12968.55	37521.16	0.76
Fe I 409.597	20874.48	45281.83	0.03
Fe I 409.818	26140.18	50534.40	0.07
Mn I 401.810	17052.29	41932.64	0.25
Mn I 403.076	0	24802.25	0.17
Mn I 403.307	0	24788.05	0.17
Mn I 403.449	0	24779.32	0.16
Mn I 403.573	\	\	\
Mn I 404.136	17052.29	41789.48	0.79
Mn I 404.876	17451.52	42143.57	0.75
Mn I 407.924	17637.15	42143.57	0.38

It is also reported that the signal enhancement was shown to be dependent on gate delay time [37-39]. In this work, the signals were recorded in different delay to investigate the dependence on gate delay. Fig. 5.3 shows the enhancement of different spectral lines as a function of delay time. Compared with SP-LIBS, the enhancement for long-short DP-LIBS was 3-7 folds depends on different delay time and spectral line. The reason for the enhancement can be explained as follows. In LIBS process, the emission intensity is influenced by the plasma conditions thereby influenced by the plasma generation process and cooling process. Through the absorption of laser energy, the initial free electrons are generated from the sample surface. Once the initial free electrons generated, the laser photons are also absorbed by the plasma through inverse bremsstrahlung absorption [2]. By adding an external long-pulse-width laser beam to these processes, the energy demand of the initial free electrons generation is reduced because of the pre-heating effect. At the same time, the inverse bremsstrahlung absorption can be sustained for a longer time because of the irradiation with long pulse. Therefore, the plasma becomes bigger, more stable and higher temperature in long-short DP-LIBS situation. Accordingly, the emission

intensity from the plasma is enhanced effectively. Moreover, to quantitatively discuss the above-mentioned influence of excitation energy on enhancement, the enhancement of iron spectral lines with different excitation energies was also plotted in Fig. 5.3. The enhancement was clearly found to be larger for the Fe I 402.187 nm with higher excitation energy. This phenomenon can be attributed to that the plasma was sustained at higher temperature in long-short DP-LIBS condition, thus the enhancement of spectral lines with high excitation energies was found to be larger than those with low excitation energies. In previous reports [40,41], it has been found that the spectral lines with low excitation energies, especially the resonance spectral lines, are prone to be affected by self-absorption. It is also proved that the self-absorption effect on quantitative analysis can be weakened by selecting the spectral lines with high excitation energies [40]. Excitingly, the intensity of the spectral lines with high excitation energies was strongly enhanced by long-short DP-LIBS configuration, which is possible to improve the performance of quantitative analysis for LIBS.

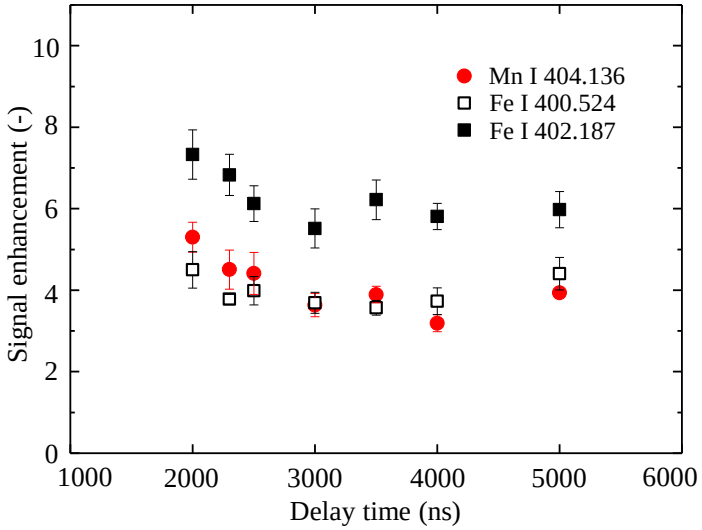

Fig. 5.3 Signal enhancement observed for long-short DP-LIBS. Experiment conditions: gate width: 1000 ns, accumulation: 50 times, delay time: 3000 ns, SP-LIBS pulse energy: 20.5 mJ, DP-LIBS pulse energy: short pulse: 20.5 mJ, long pulse: 200 mJ (FR mode).

5.3 Plasma topography

Fig. 5.4 shows the images of plasma emission region in different gate delay time using SP-LIBS, long-short DP-LIBS and long pulse LIBS respectively. It can be seen that the geometry and dynamics of plasma significantly differed from each other in SP-LIBS condition and long-short DP-LIBS condition. The plasma was enhanced obviously in long-short DP-LIBS condition. Moreover, the observed geometry shows an interesting difference. In long-short DP-LIBS condition, the plasma was a spherical structure and totally expanded to the upward side of the sample surface. It indicates that the long-pulse-width laser supplied the energy for the plasma plume. On the other hand, the emission region of plasma gradually weakened with the increasing

delay time. According to the images in the delay time of 4000 ns, the plasma emission was still observable in long-short DP-LIBS condition but it almost disappeared in SP-LIBS condition. This is also an evidence for that the long-pulse-width laser supplied the energy for the plasma and extended the lifetime of plasma. In addition, the observed results confirm that the long pulse didn't generate the plasma from sample. Only a flat and weak emission region can be observed on the surface of sample in Fig. 5.4(c). This emission was originated from the heated sample material. The long pulse has heated up the sample material on the focused area, which led to a weak emission light. In the long-short DP-LIBS process, long pulse can't generate the plasma from sample due to low power density. During the duration time of long pulse, the short pulse generated the plasma for the first time. It is different from the traditional collinear DP-LIBS, which usually generated the plasma two times because of the two short pulses [21]. Therefore, the plasma generation, evolution and cooling processes were easily controlled by long-pulse-width laser in the long-short DP-LIBS configuration.

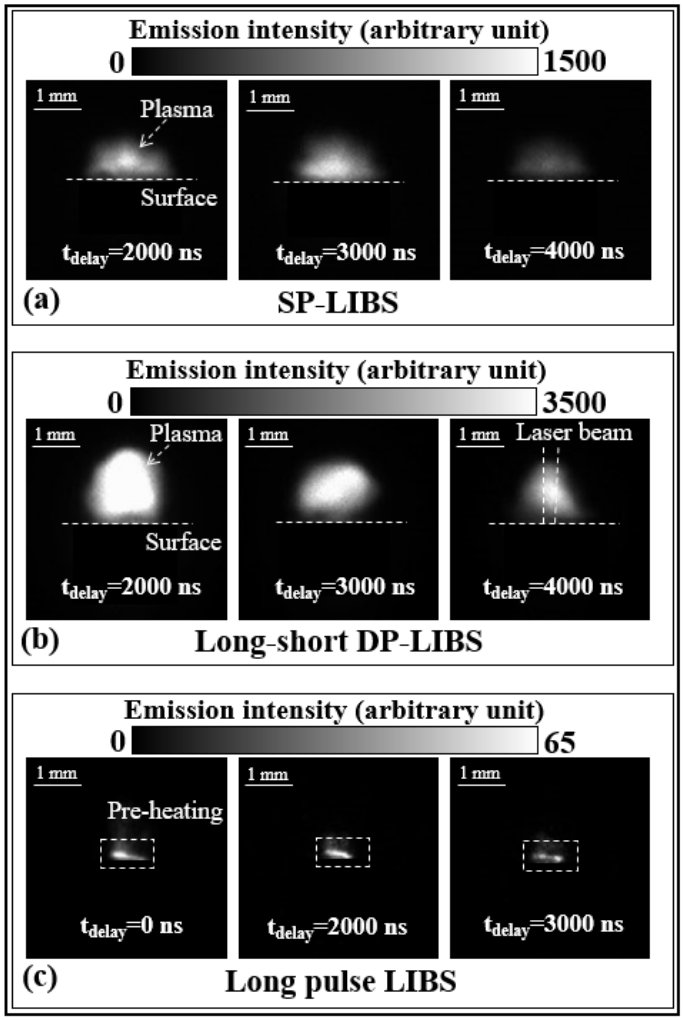

Fig. 5.4 Images of plasma emission in different delay time, (a) SP-LIBS, (b) long-short DP-LIBS and (c) long pulse LIBS. Experiment conditions: gate width: 1000 ns, accumulation: 1

time, filter central: 405 nm (FWHM 10 nm), SP-LIBS pulse energy: 20.5 mJ, DP-LIBS pulse energy: short pulse: 20.5 mJ, long pulse: 200 mJ (FR mode), long pulse LIBS pulse energy: 200 mJ (FR mode).

5.4 Plasma temperature

To further understand the fundamental of long-short DP-LIBS, the plasma temperature was estimated using Boltzmann plots. Fe I lines at 400.524, 400.971, 401.453 and 402.472 nm were used for plasma temperature estimation. Fig. 5.5 shows the variation of plasma temperature as a function of delay time. In SP-LIBS condition, it is easy to be understood that the plasma temperature continued to decrease with the delay time due to the surrounding cold air. Usually, the laser pulse ends in a very short time in LIBS process, such as several nanoseconds or dozens of nanoseconds. After the plasma generation, the hot plasma region was continuously cooled down by the air [42]. Therefore, the plasma temperature continuously decreased in SP-LIBS process. However, the situation was different in the long-short DP-LIBS. As shown in Fig. 5.5, the plasma temperature of long-short DP-LIBS was higher than that of SP-LIBS. At the same time, the plasma temperature was maintained at a stable situation. Long-short DP-LIBS generated a higher temperature and more stable plasma using the same short pulse energy. In long-short DP-LIBS process, the long pulse was added to the plasma generation and cooling processes. The long-pulse-width laser irradiated the plasma region after the ends of short pulse, which controlled the plasma cooling process. Thus, the plasma temperature was maintained at a stable state in long-short DP-LIBS situation. On the other hand, the plasma temperature can't be maintained in a stable state in conventional DP-LIBS due to the second pulse was still a short-pulse-width beam. The second pulse of conventional DP-LIBS usually supplied the energy within a few nanoseconds, which means the plasma cooling process was the same with SP-LIBS during the signal measurement period [26].

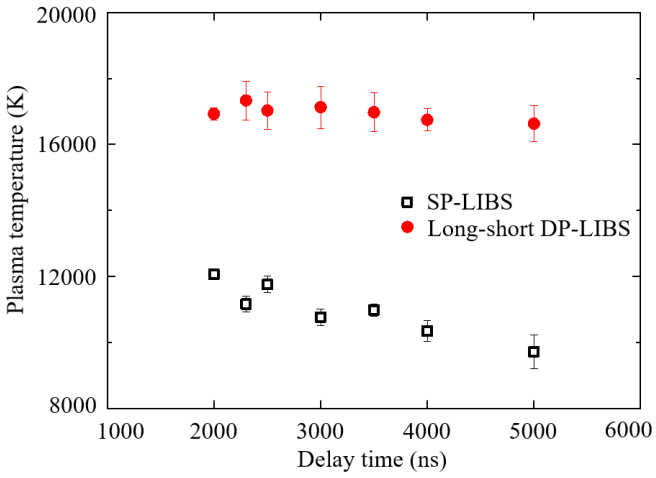

Fig. 5.5 Variation of plasma temperature with delay time for SP-LIBS method and long-short DP-LIBS method.

5.5 Time-resolved intensity ratio

According to the measured spectra in different gate delay time, the intensity ratio of manganese and iron (I_{Mn}/I_{Fe}) was calculated to investigate the time dependence of signal. Fig. 5.6 shows the delay time influence on I_{Mn}/I_{Fe}. As the delay time increased, I_{Mn}/I_{Fe} appeared an interesting tendency in long-short DP-LIBS condition. Compared with that of SP-LIBS, I_{Mn}/I_{Fe} of long-short DP-LIBS increased slowly as the delay time increased. The variation of I_{Mn}/I_{Fe} showed a remarkable stabilization around the delay time of 3000 ns using long-short DP-LIBS. This result clearly indicates that the plasma signals can be stabilized for a period of time using long-short DP-LIBS configuration. The measurement accuracy and repeatability can be improved using the signal which is stable during the recording period. It's a meaningful result for the precision improvement of LIBS. In addition, I_{Mn}/I_{Fe} also shows smaller standard deviation ratios (SDRs) in long-short DP-LIBS condition. This result further proves that the plasma was stabilized by the long-pulse-width laser beam. The lower SDRs contribute to a better measurement repeatability, which is an important performance indicator for LIBS.

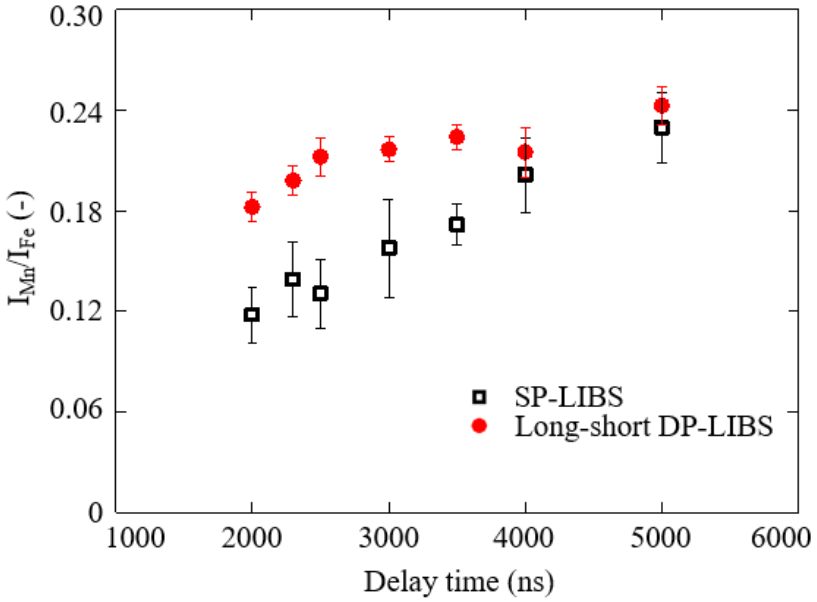

Fig. 5.6 Variation of intensity ratio with delay time for SP-LIBS and long-short DP-LIBS, "I_{Mn}/I_{Fe}" means the intensity ratio of Mn I 404.136 nm to Fe I 404.581 nm. Experiment conditions: gate width: 1000 ns, accumulation: 50 times; SP-LIBS pulse energy: 20.5 mJ, DP-LIBS pulse energy: short pulse: 20.5 mJ, long pulse: 200 mJ (FR mode).

To investigate the signal quality of long-short DP-LIBS, two kinds of standard steel samples were measured in air respectively, as shown in Fig. 5.7. The results of SP-LIBS and long-short DP-LIBS were compared to investigate the performance of the new method. The features of DP-

LIBS were discussed in various gate delay time. Fig. 5.8 shows the comparison of measured spectra using SP-LIBS and long-short DP-LIBS. The signals were deducted background and normalized with the maximum signal value of the DP-LIBS spectrum (ZG45 sample). After screening, 4 manganese emission lines and 1 iron emission line were chosen to condact the future quantitative analysis of Mn element. In order to avoid the mutual interference between the 4 Mn lines, the intensity values from 402.961 nm to 403.634 nm were summed as the integrated intensity of Mn element after deducting the continuous backgrounds.

Fig. 5.7 The sample shape used in this study. (a) ZG45# sample with bulk shape and (b) JSS 030-9 sample with powder shape

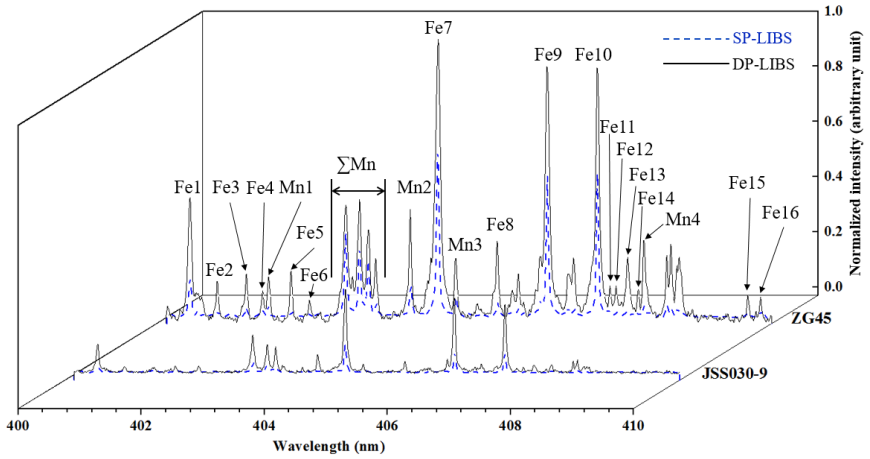

Fig. 5.8 Normalized spectra of standard samples. Conditions: gain: 3500, gate width: 1000 ns, accumulation: 50 times, delay time: 3000 ns, short pulse energy: 20.5 mJ/p, long pulse energy: 200 mJ/p.

The line information from the National Institute of Standards and Technology (NIST) database was provided in Table 5.1. In this work, the improvement of signal quality using DP-LIBS is

first discussed. When comparing the measured spectra of each sample, the signals were enhanced obviously when using DP-LIBS.

Fig. 5.9(a) and Fig. 5.9(b) showed the integrated intensity of Mn lines and the corresponding enhancement ratio of intensity at different gate delay time. The intensity was enhanced obviously at each gate delay time when using DP-LIBS. Fig. 5.10(a) and Fig. 5.10(b) provided the signal and background ratio (SBR) of Mn lines. The SBR of DP-LIBS was also enhanced remarkably. In the LIBS process, the first plasma is produced by the absorption of laser energy. Once the initial free electrons were here, the laser photons are also absorbed by the plasma through inverse bremsstrahlung absorption. When adding an external long pulse laser in this process, the energy demand of plasma generation is reduce because of pre-heating effect and the inverse bremsstrahlung absorption also can be sustained a longer time. The plasma becomes more strong, stable and uniform when using the same short pulse laser energy. Thus the lifetime of plasma is extended and the emission intensity of Mn lines from the plasma is improved obviously. In Fig.5.11(a) and Fig. 5.11(b), the ratio of Mn lines and Fe line were calculated and plotted to investigate the plasma conditions. As the gate delay time increasing, the Mn/Fe ratio shows an interesting tendency. Around 3000 ns, there was a period of stable-ratio time. This phenomenon indicates that the plasma can be stable for a period of time when using long-short DP-LIBS. It's a meaningful result for solving the precision problem of LIBS. When using signals from a stable plasma, the measurement accuracy will be improved accordingly.

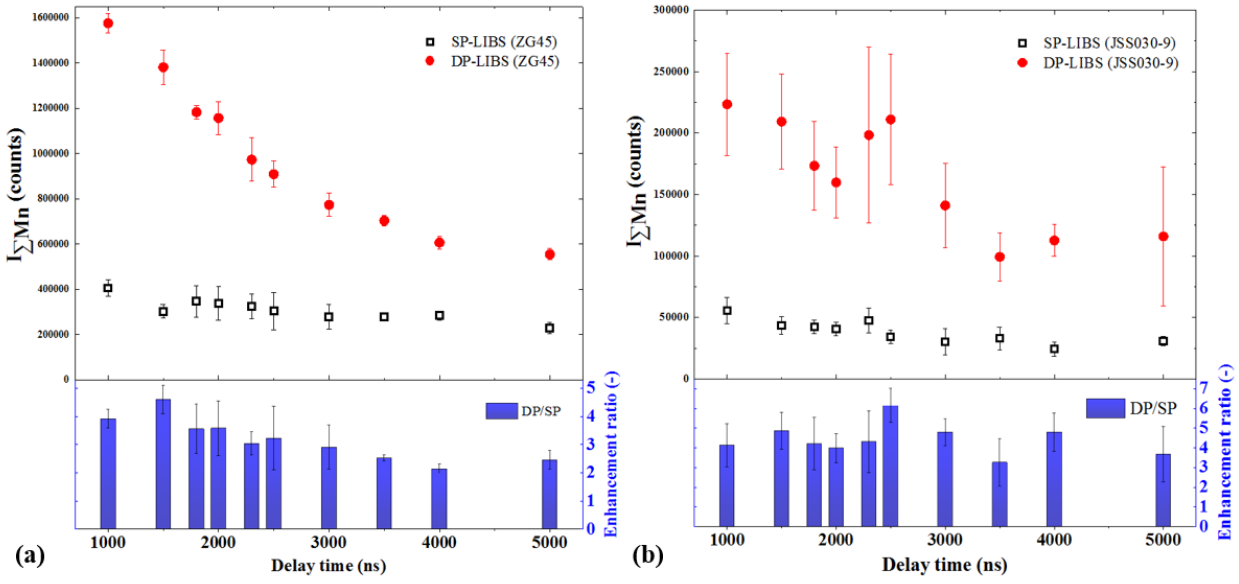

Fig. 5.9 Intensity of ∑Mn and enhancement ratio. (a) ZG45 sample, (b) JSS 030-9 sample. Condition: gain: 3500, gate width: 1000 ns, accumulation: 50 times, short pulse energy: 20.5 mJ/p, long pulse energy: 200 mJ/p, repetition: 5 times at each delay time.

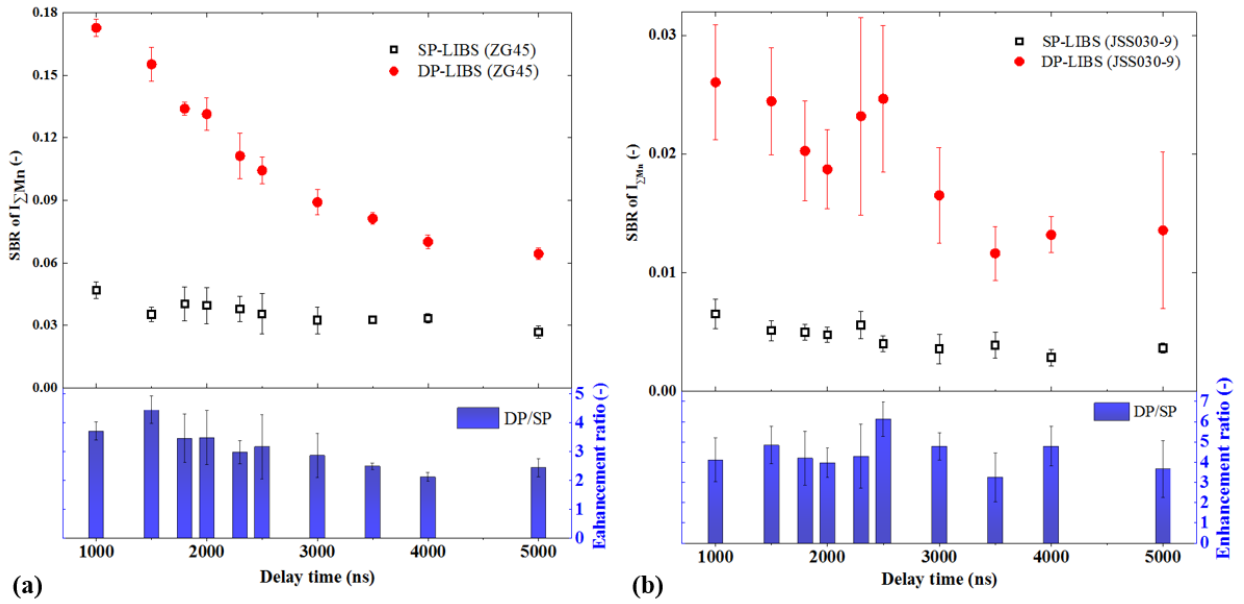

Fig. 5.10 SBR of $I_{\sum Mn}$ and enhancement ratio. (a) ZG45 sample, (b) JSS 030-9 sample. Condition: gain: 3500, gate width: 1000 ns, accumulation: 50 times, short pulse energy: 20.5 mJ/p, long pulse energy: 200 mJ/p, repetition: 5 times at each delay time.

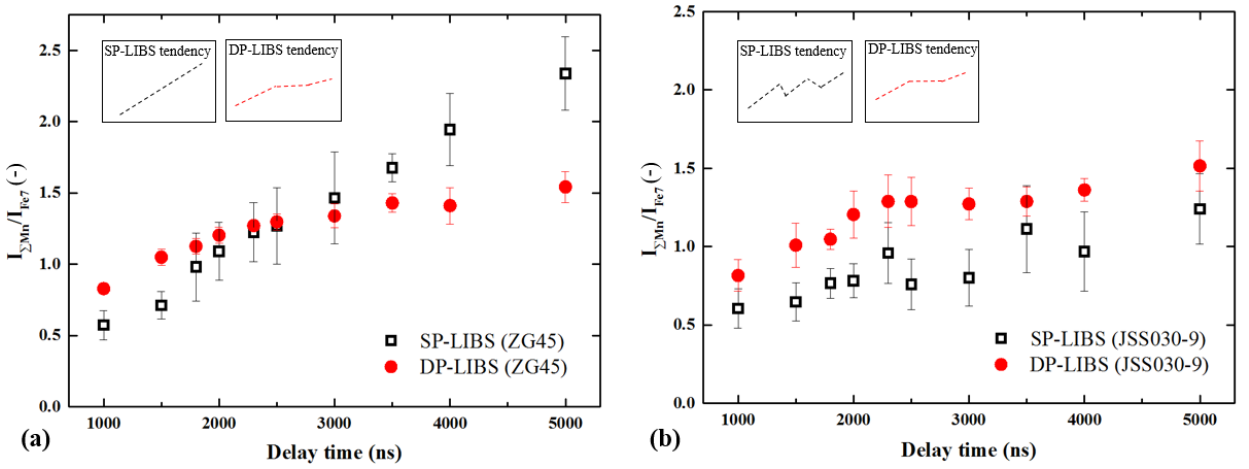

Fig. 5.11 Intensity ratio of ∑Mn and Fe7 ($I_{\sum Mn}/I_{Fe7}$). (a) ZG45 sample, (b) JSS 030-9 sample. Condition: gain: 3500, gate width: 1000 ns, accumulation: 50 times, short pulse energy: 20.5 mJ/p, long pulse energy: 200 mJ/p, repetition: 5 times at each delay time.

In addition, it can be found that the signals quality of JSS 030 sample decreased a lot due to the rough surface when comparing the results in Fig. 5.9, Fig. 5.10, Fig. 5.11 and Fig. 5.12. Apparently, the uneven surface has a negative influence on the LIBS measurement. Therefore, more attention should be paid for the signal quality enhancement in the plants application where no time for sample polishing. The long-short DP-LIBS seems to be a good method for these situations.

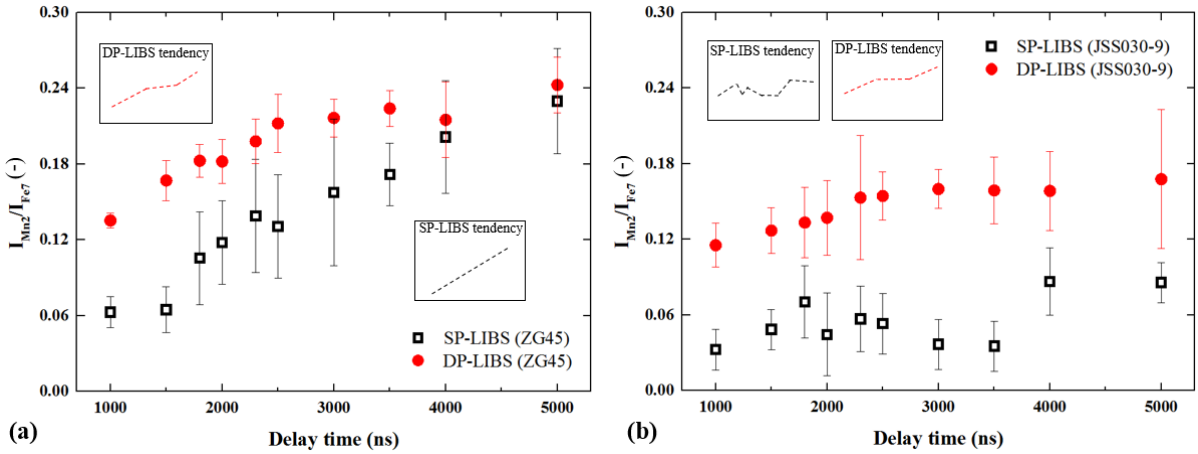

Fig. 5.12 Intensity ratio of Mn2 and Fe7 (I_{Mn2}/I_{Fe7}). (a) ZG45 sample, (b) JSS 030-9 sample. Condition: gain: 3500, gate width: 1000 ns, accumulation: 50 times, short pulse energy: 20.5 mJ/p, long pulse energy: 200 mJ/p, repetition: 5 times at each delay time.

5.6 Dependence on sample temperature

In the steel production line, the temperature of the measurement target often changes temporally and spatially. It is valuable for real application to generate a stable plasma condition from the samples with different temperatures. Therefore, the influences of sample temperature have also been discussed by measuring the signal at different environmental temperatures. Fig.5.13 shows the measured spectra of SP-LIBS and long-short DP-LIBS at different sample temperatures.

The spectra significantly differ from each other in SP-LIBS condition, whereas, the spectra show a dramatic conformity in long-short DP-LIBS condition. The results indicate that long-short DP-LIBS generated the stabilized plasma from the sample with different temperatures. As well known, before the plasma generation, a part of laser energy was absorbed by the sample material. When the initial temperature of sample was different, the laser energy involved in the plasma generation process was also different [43]. Due to the pre-heating effect of the long pulse, the short pulse generated the plasma from the surface with relatively stable temperature. Therefore, for long-short DP-LIBS, the laser energy involved in the plasma generation process was basically the same in different sample temperature conditions. On the contrary, for SP-LIBS, this part of energy was obviously affected by the initial temperature of sample. This can be called as “temperature effect”, which always exists in online measurement, especially the online measurement for steel production line [43]. According to the results in Fig. 5.13, the temperature effect was effectively eliminated by long-short DP-LIBS.

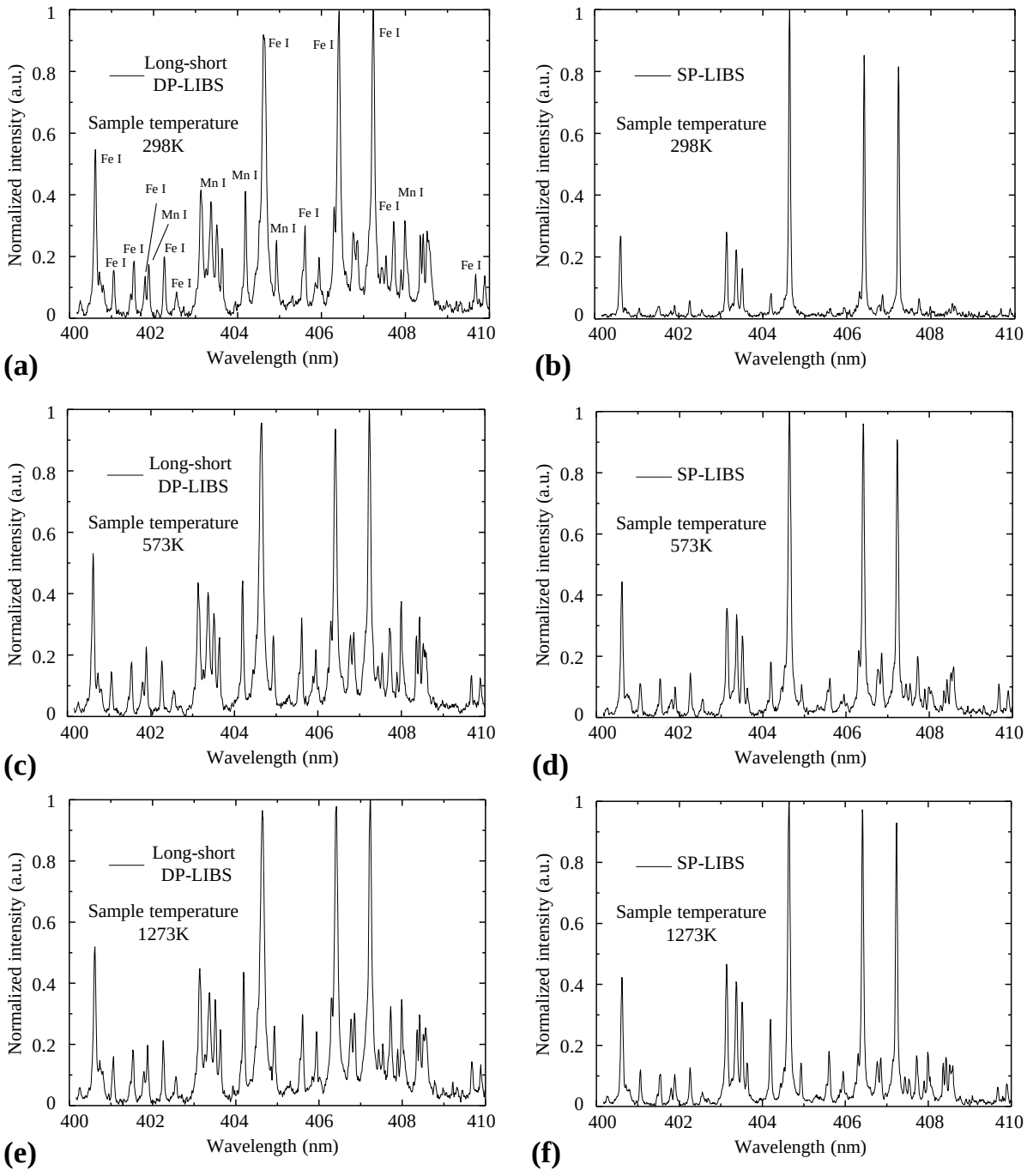

Fig. 5.12 Measured spectra of SP-LIBS and long-short DP-LIBS at different sample temperature. Experiment conditions: gate width: 1000 ns, accumulation: 50 times, delay time: 3000 ns, SP-LIBS pulse energy: 20.5 mJ, DP-LIBS pulse energy: short pulse: 20.5 mJ, long pulse: 200 mJ (FR mode).

6 Quantitative analysis of steel samples under the simulated plant conditions

6.1 Laser-induced breakdown processes for solid sample and temperature effect

In the LIBS process for solid sample, a laser beam is focused onto a small area, producing hot plasma. The material contained in plasma is atomized, and light is released corre-sponding to a unique wavelength for each element. Despite the fact that the processes involved are complex, the emission intensity from the atomized species can be described by the following equation with the assumption of a uniform plasma temperature:

$$I_{(i)} = n_{(i)} \sum_{j} \left\{ K_{(i),j} g_{(i),j} \exp\left(-\frac{E_{(i),j}}{kT} \right) \right\} \tag{6-1}$$

In the above expression, $I_{(i)}$ is the emission intensity of species i, $n_{(i)}$ is the concentration of species i, $K_{(i),j}$ is a variable that includes the Einstein A coef-ficient from the upper energy level j, $g_{(i),j}$ is the statistical weight of species i at the upper energy level j, $E_{(i),j}$ is the upper energy level of species i, k is the Boltzmann constant, and T is the plasma temperature. In Eq. (6-1), there are several factors that affect the emission intensity $I_{(i)}$. These include plasma temperature, plasma nonuniformity, and matrix effects. The appropriate correction factors must be included in $K_{(i),j}$ to obtain quantita-tive results.

A calibration of the LIBS signal is necessary for quantitative analyses. The signal intensity of LIBS depends on several factors, including plasma tem-perature, and its signal essentially fluctuates. Because of these intrinsic char-acteristics of LIBS, the signal intensity ratio has often been used for elemental composition analyses. This procedure can eliminate some of the fluctuation factors. It is, however, necessary to cancel out the plasma temperature effects from the signal intensity ratio. According to Eq. (6-1), the emission intensities of species $i1$ at the upper energy levels jl and $j2$ are given by

$$I_{(i),j1} = n_{(i)} K_{(i),j1} g_{(i),j1} \exp\left(-\frac{E_{(i),j1}}{kT} \right) \tag{6-2}$$

$$I_{j(1),j2} = n_{(i)} K_{(i),j2} g_{(i),j2} \exp\left(-\frac{E_{(i),j2}}{kT} \right) \tag{6-3}$$

From Eq. (6-2) and Eq. (6-3), the plasma temperature T has the following relation with the emission intensity ratio $I_{(i),j1}/I_{(i),j2}$:

$$\exp\left(-\frac{1}{kT} \right) = \left(\frac{I_{(i),j1}}{I_{(i),j2}} \frac{K_{(i),j2}}{K_{(i),j1}} \frac{g_{(i),j2}}{g_{(i),j1}} \right)^{\frac{1}{(E_{(i),j1} - E_{(i),j2})}} \propto \left(\frac{I_{(i),j1}}{I_{(i),j2}} \right)^{b_{(i)}} \tag{6-4}$$

where $b_{(i)}$ is a plasma temperature correction factor. It is inferred from Eq. (6-4) that the effect of plasma temperature is corrected by the emission intensity ratio $I_{(i),j1}/I_{(i),j2}$. It means that different emission lines from the same species can be selected to cancel the plasma temperature dependence of the emission intensity.

In LIBS one of the emissions in Eq. (6-1) is often selected for the ele-mental composition measurement. In this case $n_{(i)}$ can be recast in the form

$$n_{(i)} = \frac{I_{(i),j}}{K_{(i),j} g_{(i),j} \exp\left(-\frac{E_{(i),j}}{kT}\right)} \tag{6-5}$$

There are several forms in which plasma correction terms can be put into Eq. (6-5). With the matrix effects considered, one of the forms may have the following relation:

$$n_{(i)} = K_{(i)} \left(I_{(i),j}\right)^{b_0} \prod_{i1} \left(\frac{I_{(i1),j1}}{I_{(i1),j2}}\right)^{b_{(i1)}} \tag{6-6}$$

where $K_{(i)}$ and b_0 are correction factors of species i, and $b_{(i1)}$ is the temperature correction factor in the emission pair of $I_{(i),j1}$ and $I_{(i),j2}$.

A typical correction curve of the plasma temperature is shown in Fig. 6.1 In this case, the two Mg lines, shown Mg_1 and Mg_2 in the figure, are used for the plasma temperature correction. It is clear from Fig. 6.1(b) that the ratios are influenced by the plasma condition, which is directly related in the ratio Mg_1/Mg_2. The results are shown in Fig. 6.1(c). By applying the temperature correction scheme, the I_{si}/I_{A1} ratios become con-stant even for different plasma conditions, that is, Mg_1/Mg_2. These correc-tion factors are dependent on the pressure, emission detection delay time, detection time width, laser intensity, and other factors. Remember that LIBS employs the plasma generation process using pulsed laser energy, which is not in the equilibrium condition at all. There are also matrix effects in LIBS signal intensities that cannot be predicted using Eq. (6-4). Therefore, the calibration method described above is an empirical one, and the correction factors are valid only in the specific experimental conditions. These factors have to be determined in each measurement condition.

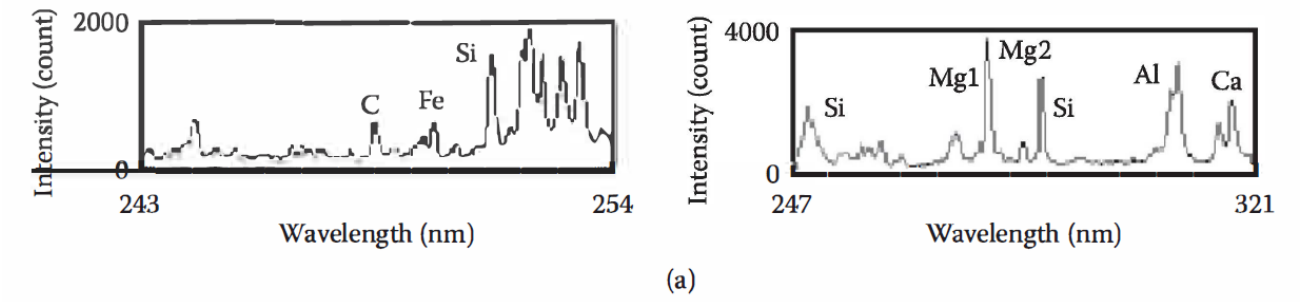

(a)

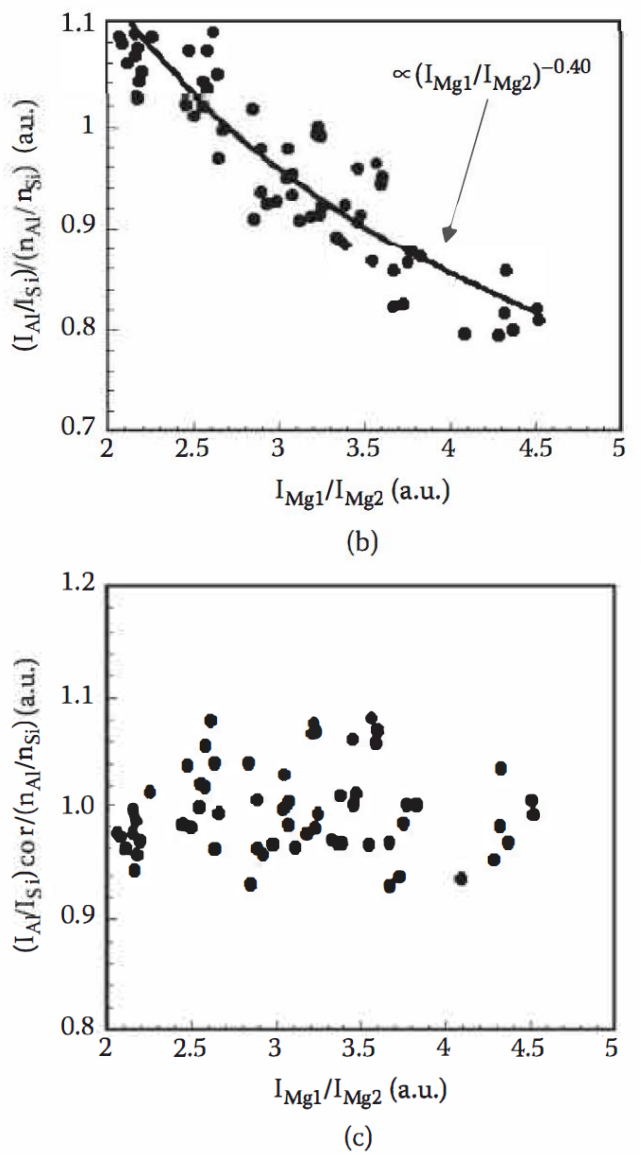

Fig. 6.1 Typical correction curve of the plasma temperature. Data were collected using several differ-ent fly ash samples and different plasma conditions. The effect of the species concentration in different fly ash samples was canceled by dividing I_C/I_{Si} by n_C/n_{Si}. It is clear that the ratio I_C/I_{Si} is influenced by the condition of plasma, which is directly related in the ratio Mg_1/Mg_2. By applying the temperature correction scheme, these ratios become constant even for different plasma conditions. (a) Fly ash LIBS spectrum from. (b) Correction factor for the I_C/I_{Si} ratio. (c) Corrected Results for the I_C/I_{Si}. [2]

The above mentioned method is using a calculation method to weak the temperature effect on the LIBS measurement. However, it is still required an effective method to generate a stable plasma for the LIBS analysis. Therefore, we have used the conventional LIBS and long-short DP-LIBS to carry out the relevant experiments. After the experiments, we have used the same plot method to investigate the plasma temperature effect on the signal intensity ratio of LIBS.

Fig.6.2 shows the experimental results of conventional LIBS and long-short DP-LIBS. It can be seen that the signal intensity ratio is fluctuant in the condition of conventional LIBS method. Differently, the experimental results in the condition of long-short DP-LIBS shows a remarkable stable compared that SP-LIBS. Both of the intensity fluctuation and plasma temperature fluctuation are decreased by the long-short pulse laser beam. This is an exciting results for the improvement of LIBS method. The results indicated that the long pulse laser beam can stabilize the plasma to a relative stable conditions which is benefit for the measurement of LIBS signal.

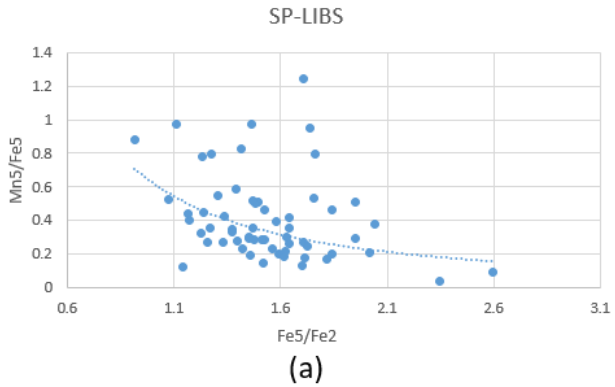

(a)

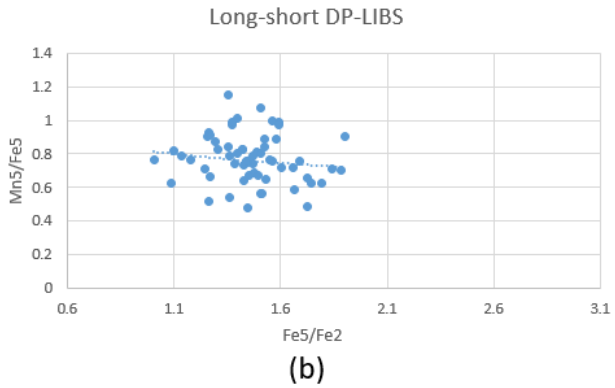

(b)

Fig. 6.2 The dependence of signal intensity ratio on the plasma temperature. (a) Conventional SP-LIBS and (b) long-short DP-LIBS. Experiment conditions: gate width: 1000 ns, accumulation: 50 times, delay time: 3000 ns, SP-LIBS pulse energy: 20.5 mJ, DP-LIBS pulse energy: short pulse: 20.5 mJ, long pulse: 200 mJ (FR mode). Sample temperature: From room temperature to 700 ºC.

6.2 Detection ability for steel samples

The steel washers with rusty surface and clean surface were tested using SP-LIBS and long-short DP-LIBS, respectively. The detection ability was discussed according to the testing results. Fig. 6.3 shows the recorded spectra from the rusty steel washers. SP-LIBS was unable to obtain a clear spectrum for further analysis. On the contrary, long-short DP-LIBS had obtained a satisfactory spectrum from the rusty steel washers. Many spectral lines of iron and manganese

can be distinguished from the spectrum which was recorded by long-short DP-LIBS. The comparison of the testing results from rusty steel washers indicated that long-short DP-LIBS possesses the excellent detection ability for steel samples. The results suggested that long-short DP-LIBS can be applied in some worse situations, such as actual steel products with rusty and dirty surface, molten metals with oxide layers and steel sheets in production line with oil film on surface.

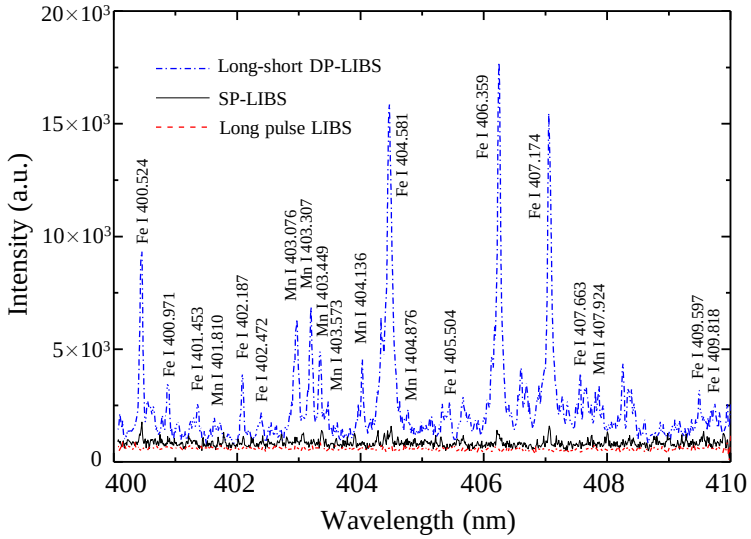

Fig. 6.3 Measured spectra from the rusty steel washers. Experimental conditions: gate width: 1000 ns, accumulation: 20 times, delay time: 2000 ns, SP-LIBS pulse energy: 20.5 mJ, long-short DP-LIBS pulse energy: short pulse 20.5 mJ, long pulse 200 mJ, long pulse LIBS pulse energy: 200 mJ.

Fig. 6.4 shows the recorded spectra from the steel washers with clean surface. The signal intensity was enhanced by long-short DP-LIBS. For the spectral lines with higher excitation energies, such as Fe atom lines at 400.971, 401.453, 402.187, 402.472, 405.504, 407.663, 409.597 and 409.818 nm, Mn atom lines at 401.810, 404.136, 404.876 and 407.924 nm, the enhancement was considerable. Enhancement in signal intensity of the spectral lines with lower excitation energies, such as Fe atom lines at 400.524, 404.581, 406.359 and 407.174 nm, Mn atom lines at 403.076, 403.307 and 403.449 nm, was also observed although the enhancement was not as dramatic as for the spectral lines with higher excitation energies. The enhancement can be attributed to the effects of long pulse. For the long-short DP-LIBS method, the long pulse per-heated the focus point on sample surface before the short pulse was fired, thus the breakdown threshold of material was reduced. With the same short pulse energy, the mass of laser ablation was increased by the preheating effect of long pulse. Furthermore, the long pulse continued to reheat the plasma after the short pulse was ended. The cooling process of plasma was controlled by the long pulse hence the plasma was maintained at higher temperature. Because of the larger ablation mass and the higher plasma temperature, the signal intensity from

the plasma was enhanced. Especially for the spectral lines with higher excitation energies, the enhancement was more notable.

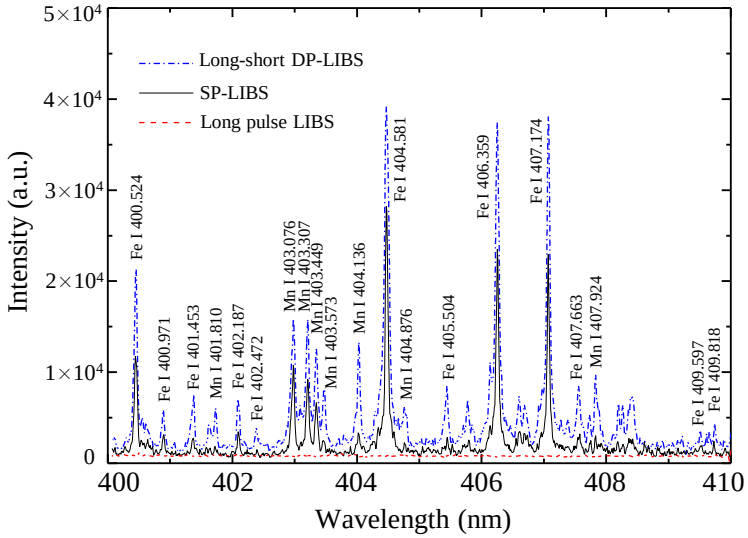

Fig. 6.4 Measured spectra from the steel washers with clean surface. Experimental conditions: gate width: 1000 ns, accumulation: 20 times, delay time: 2000 ns, SP-LIBS pulse energy: 20.5 mJ, long-short DP-LIBS pulse energy: short pulse 20.5 mJ, long pulse 200 mJ, long pulse LIBS pulse energy: 200 mJ.

In addition, the results in Fig. 6.3 and Fig. 6.4 is plotted in the same figure to clearly compare the different results using SP-LIBS and long-short DP-LIBS, as shown in Fig. 6.5.

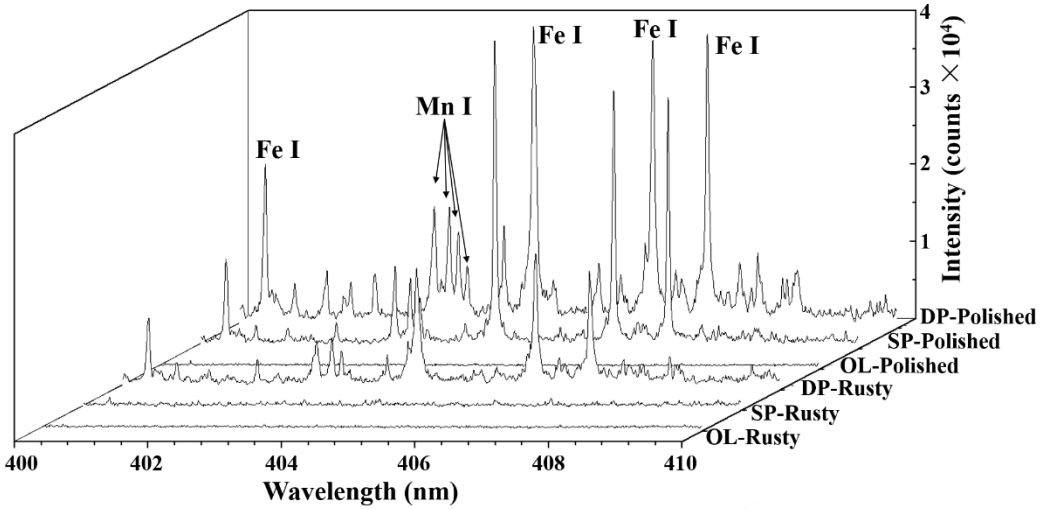

Fig. 6.5 Measured spectra of steel washers. OL-Rusty, only long pulse width laser result using rusty washers; SP-Rusty, SP-LIBS using rusty washers; DP-Rusty, long-short DP-LIBS using rusty washers; OL-Polished, only long pulse width laser result using polished washers; SP-Polished, SP-LIBS using polished washers; DP-Polished, long-short DP-LIBS using polished washers. Condition: gate width: 1000 ns, accumulation: 20 times, delay time:

2000 ns, inter-pulse delay time: 30 μs, short pulse width laser power: 20.5 mJ/p, long pulse width laser power: 200 mJ/p.

Fig. 6.5 also shows the spectra of steel washers after deducted continuous backgrounds in the delay time of 2000 ns. For rusty steel washers, SP-LIBS was not able to generate a clear spectrum for further analysis. Encouragingly, the DP-LIBS generated a sharp spectrum from the rusty steel washers. Several iron lines and manganese lines can be distinguished from the spectrum. The results indicate that the DP-LIBS can be applied in some worse situations, such as actual steel samples (rust and dirty surface), molten metals (some oxide layers on the surface) and materials in production lines (oil film on the surface). Comparing the spectra of polished steel washers, the LIBS signals are obviously enhanced using the long-short dual-pulse method. From the results it can be speculated that the long-short DP-LIBS method may enhance the limit of detection (LOD) of the microelements in target.

Whether rusty or clean steel washers, long pulse LIBS can't record obvious signal from the samples. It indicated that only the long pulse can't generate the observable plasma because of the low power density. The result demonstrated that the plasma in the long-short DP-LIBS process was generated by the short pulse, although the long pulse was fired firstly. In the literature of traditional collinear DP-LIBS, there is a discussion on whether the second pulse was absorbed by plasma plume or it generated new plasma from the sample surface [32, 43]. However, the generation and evolution processes of plasma are simpler for long-short DP-LIBS. The plasma was generated by short pulse and re-heated by long pulse in long-short DP-LIBS process. It is easier to describe the plasma using the present quantitative analysis models.

6.3 Crater morphology

It is worthy to notice the difference between the SP-LIBS spectrum and DP-LIBS spectrum. The reason is considered to be the cleaning and heating effects of long pulse laser. When long pulse laser irradiation, it provides an energy supply for 200 milli-joule per pulse, which is remarkable because of the focus lens. Although its peak power is not enough to produce plasma, the long pulse laser does made something on the target surface. If there are some loose surface layers on the target, they will be removed by the focused laser beam. It is called cleaning effect of long pulse. Coincidentally, it is reported that a series of short pulses were used to remove the surface layer of target []. However, sometimes the short pulses already generated plasmas and made a crater on the surface before the detection laser pulse coming. It has a negative influence on the LIBS process. Without this risk, it is more effective, easier control and lower cost using a soft long pulse laser to solve the surface layer problem of LIBS.

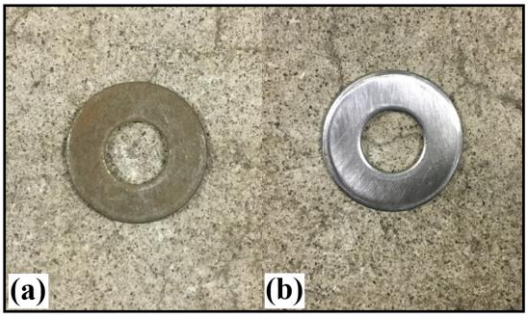

Fig. 6.6 The target used in the crater morphology study. (a) rusty washer ring and (b) polished washer ring.

To support the above opinion, the study on the crater morphology was carried out to discuss the differences on the crater characteristics. The rusty washer rings and polished washer rings were employed to investigate the crater morphology, as shown in Fig. 6.6. Scanning electron microscope (SEM) was employed to take the pictures of laser craters. The optical microscope and scanning electron microscope (SEM) were employed to take pictures of sample surface. Fig.6.7 and Fig. 6.8 show the observed results of rusty rings and polished rings respectively.

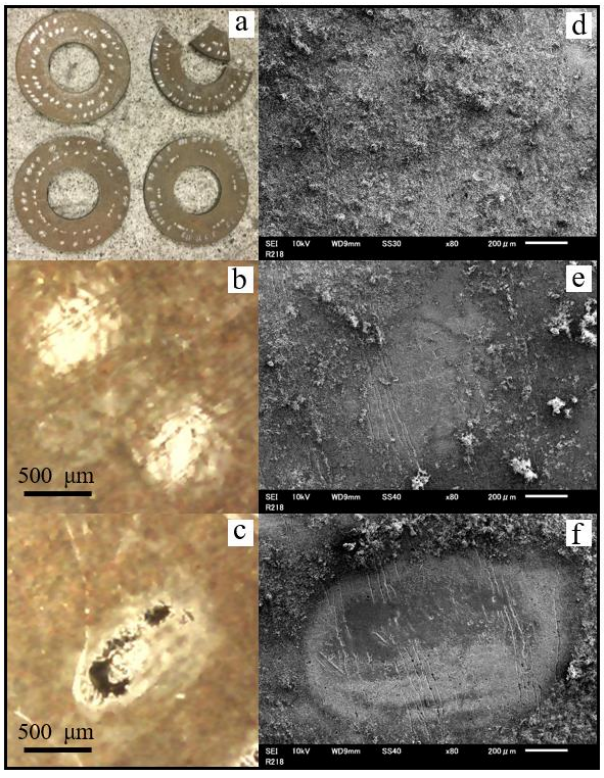

Fig. 6.7 Observed results of the rusty steel gaskets. (a) Irradiated steel gaskets, (b) optical picture of SP-LIBS ablation point, (c) optical picture of DP-LIBS ablation point, (d) SEM picture of rust layer, (e) SEM picture of SP-LIBS ablation point and (f) SEM picture of DP-LIBS ablation point.

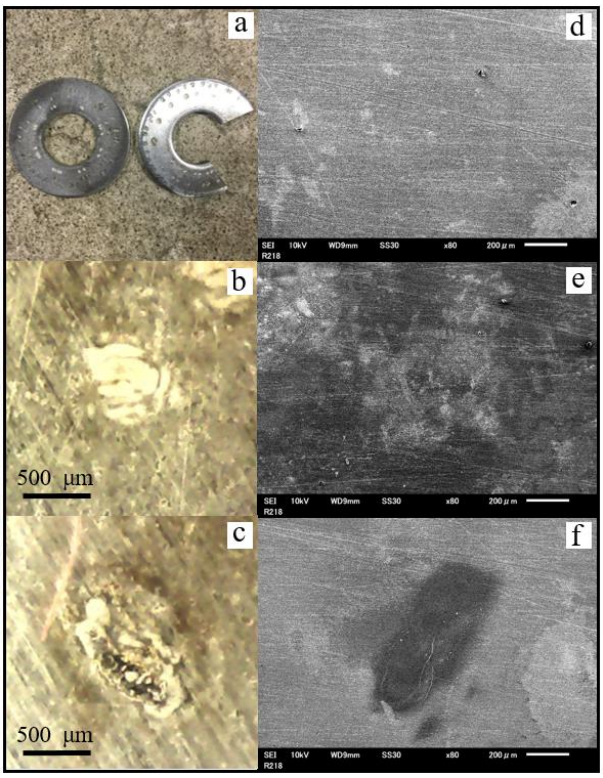

Fig. 6.8 Observed results of the polished steel gaskets. (a) Irradiated steel gaskets, (b) optical picture of SP-LIBS ablation point, (c) optical picture of DP-LIBS ablation point, (d) SEM picture of blank area, (e) SEM picture of SP-LIBS ablation point and (f) SEM picture of DP-LIBS ablation point.

Through the comparing of Fig. 6.7(f) and Fig. 6.7(g), the differences can be clearly seen. A large area of rust was totally removed when using the DP-LIBS. However, the SP-LIBS only made the upper rust slightly be brushed off. That's why the SP-LIBS got very weak signals in the rusty steel rings but DP-LIBS got satisfying results. In addition, another phenomenon can be found in Fig. 6.7 and Fig. 6.8 when making a careful comparison between the SP-LIBS and DP-LIBS results. The color of laser points is changed using the DP-LIBS (Fig. 6.7c and f, Fig. 6.8c and f). The reason is considered to be the heating effect of long pulse laser. During the long pulse laser radiation, the material of the focus point region was heated to high temperature (even to the melting temperature). Then, it is cooled to room temperature within a few seconds after DP-LIBS process finished. Due to the heating and cooling process, there were some traces left on the target surface. This pre-heating effect also has been observed in the plasma pictures. Once understood the effects of long pulse laser, the spectrum results of polished steel rings in Fig. 6.4 can be well explained. In the SP-LIBS process, a part of the laser energy is used to increase the temperature of sample material to above melting point before the plasma generation. This part of energy comes from the short pulse but not participates in the plasma generation process. For the long-short DP-LIBS, things are different. Before the short pulse coming, the temperature of

focus point already be heated to high temperature. Therefore, the signal intensity obviously increased in DP-LIBS process when using the same short pulse laser energy.

Fig. 6.9 shows the observed results from rusty and clean steel washers using SEM method. A definite difference in crater characteristic from rusty steel washers can be observed. A large area of rust on the surface was removed from the rusty steel washers by long-short DP-LIBS. Whereas, SP-LIBS was unable to efficiently remove the rusty layer. Therefore, SP-LIBS recorded very weak signal from the rusty steel washers but long-short DP-LIBS obtained a satisfactory spectrum. For the crater images observed from the clean steel washers, a large area of laser ablation can be found in the image of long-short DP-LIBS. It can be attributed to the preheating effect of long pulse. During the irradiation of long pulse, the material on the focus point was heated to high temperature, thus the efficiency of laser ablation was improved. Therefore, the crater size of long-short DP-LIBS was larger than that of SP-LIBS due to the increased mass of laser ablation.

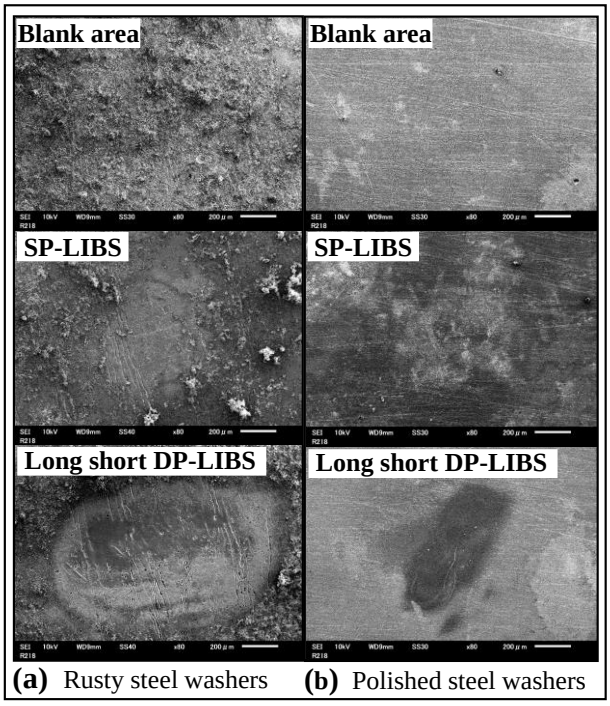

Fig. 6.9 SEM images for laser craters. (a) Results from rusty steel washers and (b) results from polished steel washers.

6.4 The analysis of solid steel samples under room temperature

The calibration curves for SP-LIBS and long-short DP-LIBS were compared in this study. All of the data obtained from 10 samples were used to establish the calibration curves. The experiment for each sample was repeated 5 times to weaken the influence of unstable laser energy. The selected spectral lines (Mn I 404.876 nm and Fe I 402.187 nm)

were used to calculate the intensity ratio of LIBS measurement. Fig. 6.10 shows the calibration curves for SP-LIBS and long-short DP-LIBS. The determination coefficients (R^2) of calibration curve was only 0.810 for SP-LIBS, whereas, it was 0.988 for long-short DP-LIBS. From this aspect, the linearity of calibration curve was dramatically improved by long-short DP-LIBS. In Fig. 6.10(a), R2 was lower than 0.9, which meant a weak correlation between the concentration ratio and the line intensity ratio. SP-LIBS did not obtain a satisfactory calibration curve for quantitative analysis, mainly because of the long optical distance in our experiments. On the contrary, long-short DP-LIBS has obtained the ideal calibration curve for quantitative analysis.

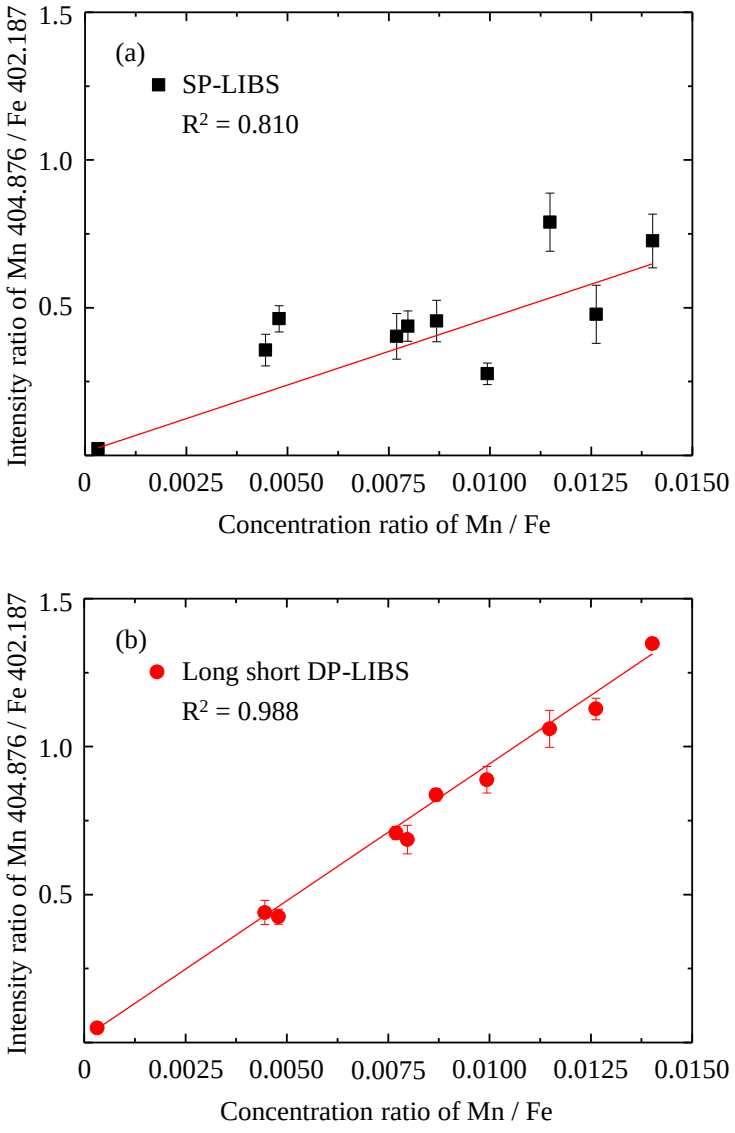

Fig. 6.10 Calibration curves for (a) SP-LIBS and (b) long-short DP-LIBS. Experimental conditions: gate width: 1000 ns, accumulation: 50 times, delay time: 4000 ns, SP-LIBS

pulse energy: 20.5 mJ, long-short DP-LIBS pulse energy: short pulse 20.5 mJ, long pulse 200 mJ.

If comparing the slope of the calibration curves, it can be found that the slope for long-short DP-LIBS was larger than SP-LIBS. This result suggests that the self-absorption effect of LIBS was efficiently eliminated by long-short DP-LIBS. In LIBS, the local temperature in plasma varied with the spatial location. Usually, the temperature in the outer region of plasma was lower than the core region. The emission from the core plasma could be absorbed by the outer plasma. Therefore, it was reported that LIBS has suffered the effect of self-absorption, which caused a decrease in the slope of calibration curve [44, 45]. Obviously, the measurement results were less affected by this effect in long-short DP-LIBS. It can be attributed to the reheating effect of long pulse. In long-short DP-LIBS, the plasma continued to be heated by the long-pulse-width laser, hence the cooling process of plasma was controlled. The uniformity and stability of plasma were improved by the energy from the long pulse. Therefore, the self-absorption phenomenon was weak in long-short DP-LIBS. In addition, it can be found in Fig. 6.9 that the standard deviation of measurement was smaller for long-short DP-LIBS, which also can be attributed to the reheating effect of long pulse.

The prediction models for Mn concentration were evaluated using the cross validation method. The unknown sample was selected from all of the samples individually, and the remaining 9 samples were employed to establish the prediction model. Fig. 6.11 shows the prediction models for Mn concentration using SP-LIBS. The R^2 of the prediction models were all lower than 0.9, except for that of the prediction model for S7 sample. The quantitative analysis based on these prediction models are unreliable for industrial application under such low R^2 coefficient. Fig. 6.12 shows the prediction models using long-short DP-LIBS. It can be seen that all of the models of long-short DP-LIBS has obtained the fine R^2 coefficient in the same experimental conditions. These results suggest that long-short DP-LIBS improved the analytical performance of LIBS.

To quantitatively compare the accuracy and precision between SP-LIBS and long-short DP-LIBS, the statistical factors like RSD and REP were calculated in current study. More

specifically, RSD factor was used to evaluate the precision of measurement and REP factor was used to evaluate the accuracy of measurement. Precision can be defined as the degree of harmonization among single test data when the measurement was carried out repeatedly [46]. Therefore, the RSD factor was calculate according to the Eq. (6-1) and Eq. (6-2).

$$s = \left[\frac{\sum(x_i - M)^2}{n-1}\right]^{1/2} \tag{6-1}$$

$$\%\text{RSD} = 100\% \times [s/M] \tag{6-2}$$

In these equations, x_i is the measured value from LIBS, n is the number of parallel experiments, M is the average value of all parallel experiments, s is the standard deviation and RSD is the relative standard deviation.

Accuracy describes the nearness of agreement between the measured experimental values and the reference value (either as a true value or the value observed by standard process). In this study, the Mn concentration provided by the seller of samples was used to testify the accuracy of long-short DP-LIBS. The REP factor was calculated using the following equation [47]:

$$\%\text{REP} = \frac{100\%}{Y_\text{m}} \sqrt{\frac{1}{N}\sum_{i=0}^{N}(Y_\text{s} - Y_\text{p})^2} \tag{6-3}$$

where Y_m is the average reference concentration of the prediction samples, N is total number of samples, Ys is the reference concentration of the sample, Y_p is the predicted concentration using the established calibration model of the sample and REP is the relative error of prediction also known as relative average root mean square error. For a fine calibration model, REP should be as small as possible. The overall efficiency of calibration models was compared using REP in this study.

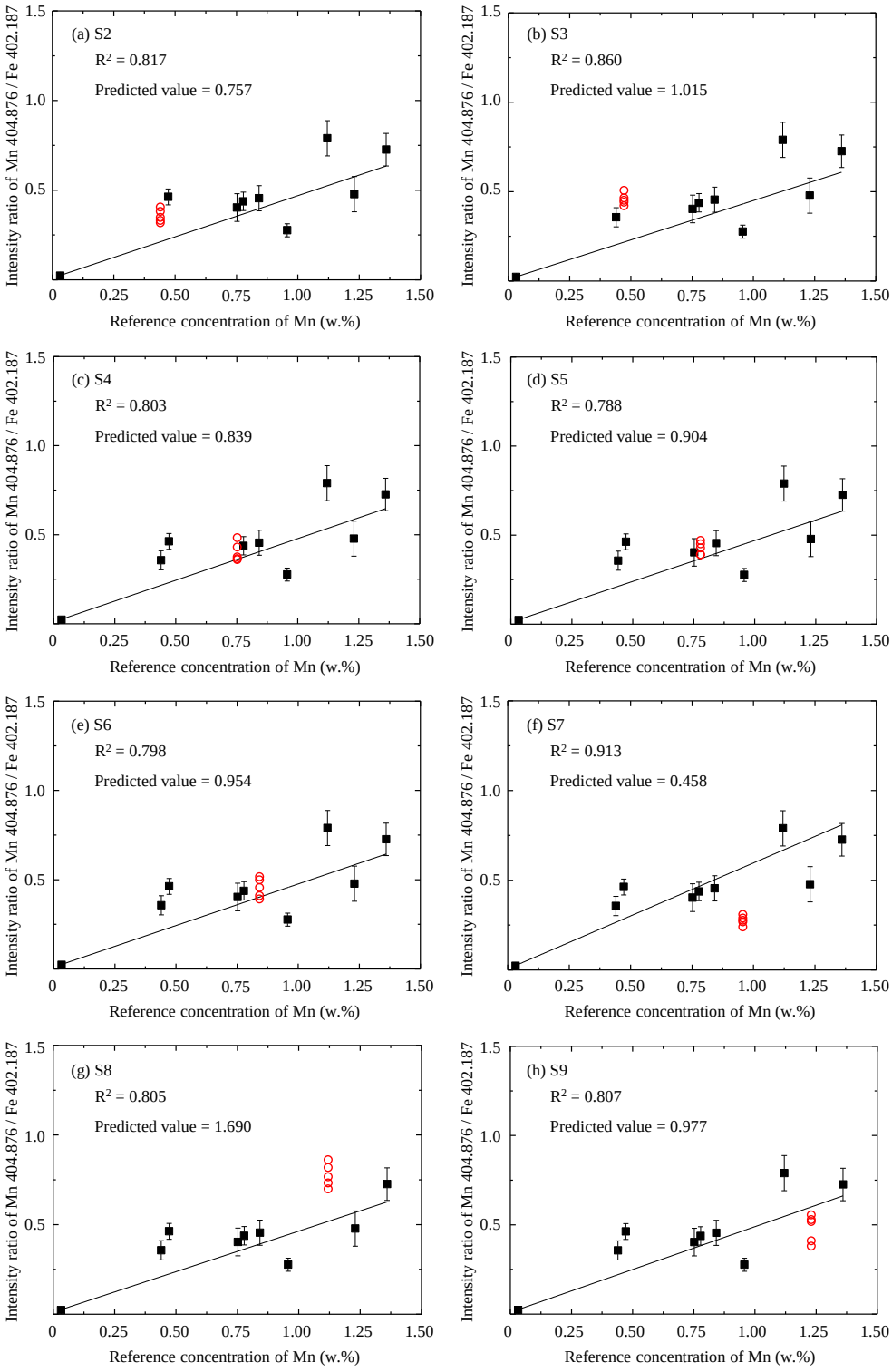

Fig. 6.11 Prediction models for SP-LIBS. (a-h) are the models for predicted sample (S2-S9), respectively. Experimental conditions: gate width: 1000 ns, accumulation: 50 times, delay time: 4000 ns, SP-LIBS pulse energy: 20.5 mJ, long-short DP-LIBS pulse energy: short pulse 20.5 mJ, long pulse 200 mJ.

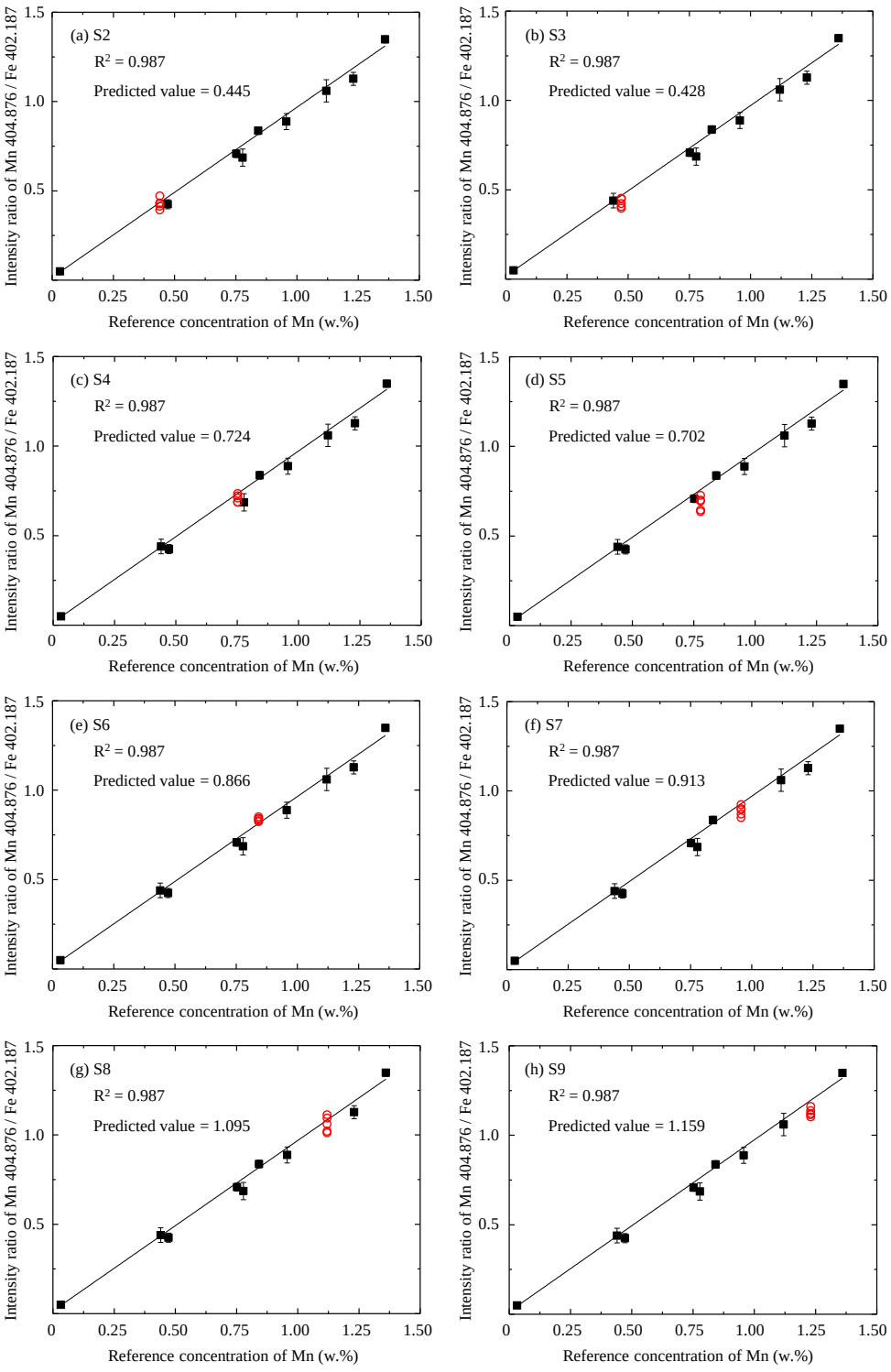

Fig. 6.12 Prediction models for long-short DP-LIBS. (a-h) are the models for predicted sample (S2-S9), respectively. Experimental conditions: gate width: 1000 ns, accumulation: 50 times, delay time: 4000 ns, SP-LIBS pulse energy: 20.5 mJ, long-short DP-LIBS pulse energy: short pulse 20.5 mJ, long pulse 200 mJ.

Table 6.1 shows a comparison of RSD and REP for SP-LIBS and long-short DP-LIBS. The precision and accuracy of long-short DP-LIBS measurement were found to be better than those of SP-LIBS measurement. The average value of RSD% was reduced from 29.3% to 10.5%, meanwhile, the average value of REP% was reduced from 94.9% to 4.9%. This result demonstrated that the use of long pulse is valuable for better analytical results of LIBS. The improvement of measurement precision and accuracy is attributed to the stabilization of plasma using long-pulse-width laser beam. Show that long-short DP-LIBS has a better analytical performance.

Table 6.1 Precision and Accuracy

Tested sample	RSD (%)		REP (%)	
	SP-LIBS	Long short DP-LIBS	SP-LIBS	Long short DP-LIBS
ZG10#	30.1	18.6	75.7	1.1
ZG25#	19.2	11.9	101.5	9.4
ZG45#	38.3	6.0	83.9	3.8
ZG60#	23.6	14.1	90.4	9.8
28CrNiMo	31.0	5.0	95.4	2.8
35CrNiMo	26.4	10.1	45.8	4.6
20MnMo	24.9	11.8	169.0	2.2
30SiMn	41.0	6.5	97.7	5.7

6.5 The analysis of solid steel samples under high temperature

In the steel production plant, the temperature of steel products is usually at high temperature. Only in the final stage of the production, the steel products are cooled down to room temperature. Therefore, the measurement of steel composition under high temperature is important for the application of LIBS to real industry. In fact, the steel products on the production line is at a certain temperature from 100 ^{o}C to 700 ^{o}C. Therefore, the analysis of solid steel samples under high temperature was carried out in this study to investigate the performance of conventional LIBS and long-short DP-LIBS under the simulated plant conditions.

The carbon steel samples were measured at different temperature using the SP-LIBS and DP-LIBS respectively (temperature region: 300K, 773K and 1273K). The spectral signals at different delay time are recorded and calculated in each temperature (delay time: 2000ns, 3000ns and 4000ns). Fig. 6.13 shows the spectra using SP-LIBS and long-short DP-LIBS. As is well known, there are many alloy elements in steel. For example, the iron and manganese are selected to analyze. According to the measurement results, several

representative wavelength regions of Fe emission were determined. Meanwhile, serval Fe and Mn lines can also be distinguished from the spectra of high resolution channel. The spectra of the steel samples at different temperatures are quite similar in the long-short DP-LIBS condition. However, the spectra show different characteristics in the SP-LIBS condition. The results indicate that the long-short DP-LIBS has a satisfactory performance in the situation of different sample temperatures. The long pulse width laser is considered to supply the enough energy for the steel samples. It leads to that the steel samples are heated to the melting point before the short pulse laser ablation. Therefore, the plasma is generated from the molten steel although the initial temperatures of the samples are different. The long-short DP-LIBS is considered to be a promising method to reduce the influences of the sample temperature.

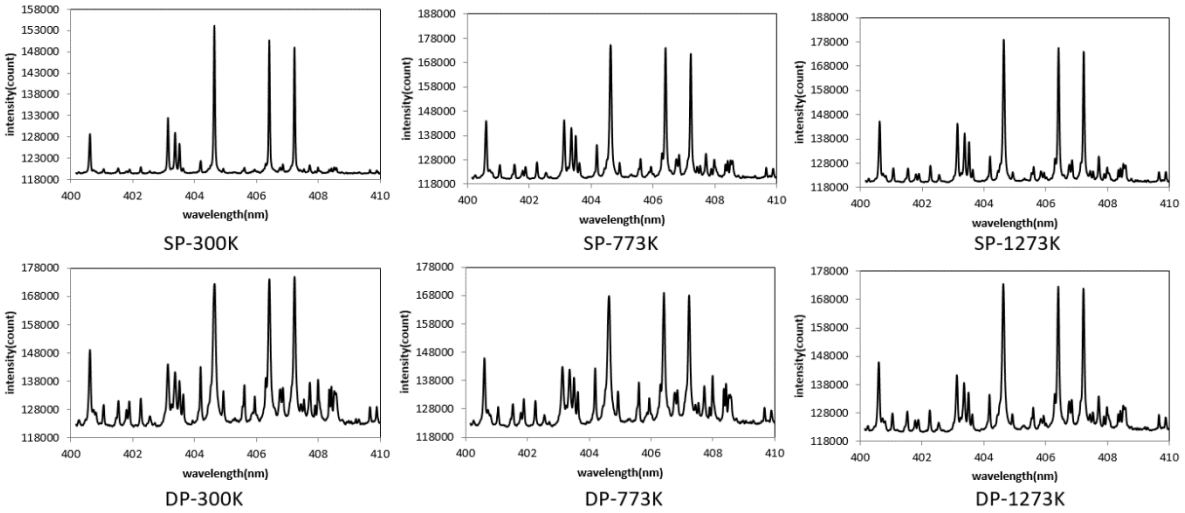

Fig. 6.13 Spectra results of SP-LIBS and long-short DP-LIBS

To compare the results of SP-LIBS and DP-LIBS, the ratios of Mn and Fe signal are calculated in each temperature. Fig. 6.14 and Fig. 6.15 show the quantitative analysis results of Mn composition respectively. After plasma temperature correction, the percentage amplitude of standard deviation is 19.0% for SP-LIBS and it is 8.4% for DP-LIBS. This indicates the plasma more stable at the DP-LIBS condition. The phenomenon could be explained as the result of power supply from long laser pulse. In LIBS process, the core of plasma is first produced by the absorption of the incident laser energy, such as multi-photon ionization process. Once the initial free electrons are produced, laser photons are strongly absorbed through inverse bremsstrahlung absorption to induce rapid expansion of plasma. When introducing the external energy from the long pulse laser in the plasma cooling process, the inverse bremsstrahlung absorption can appear in this process to maintain the plasma at higher temperature and extend its lifetime. Therefore the stability of plasma can be improved using DP-LIBS.

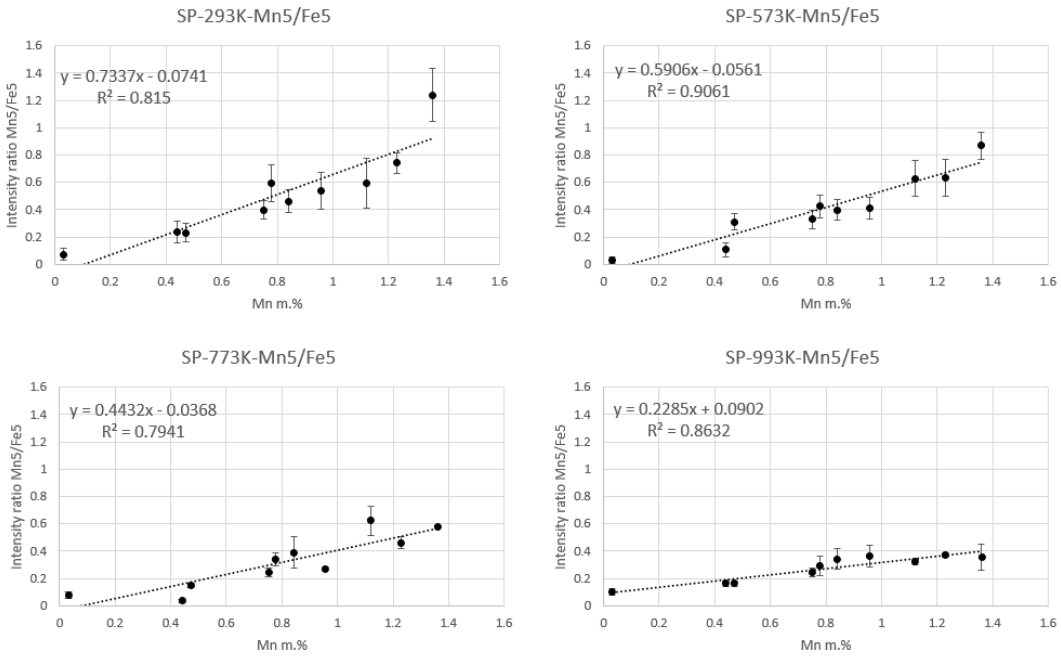

Fig. 6.14 Quantitative analysis results of Mn composition using SP-LIBS under the simulated plant conditions (sample temperature from 20 ºC to 700 ºC).

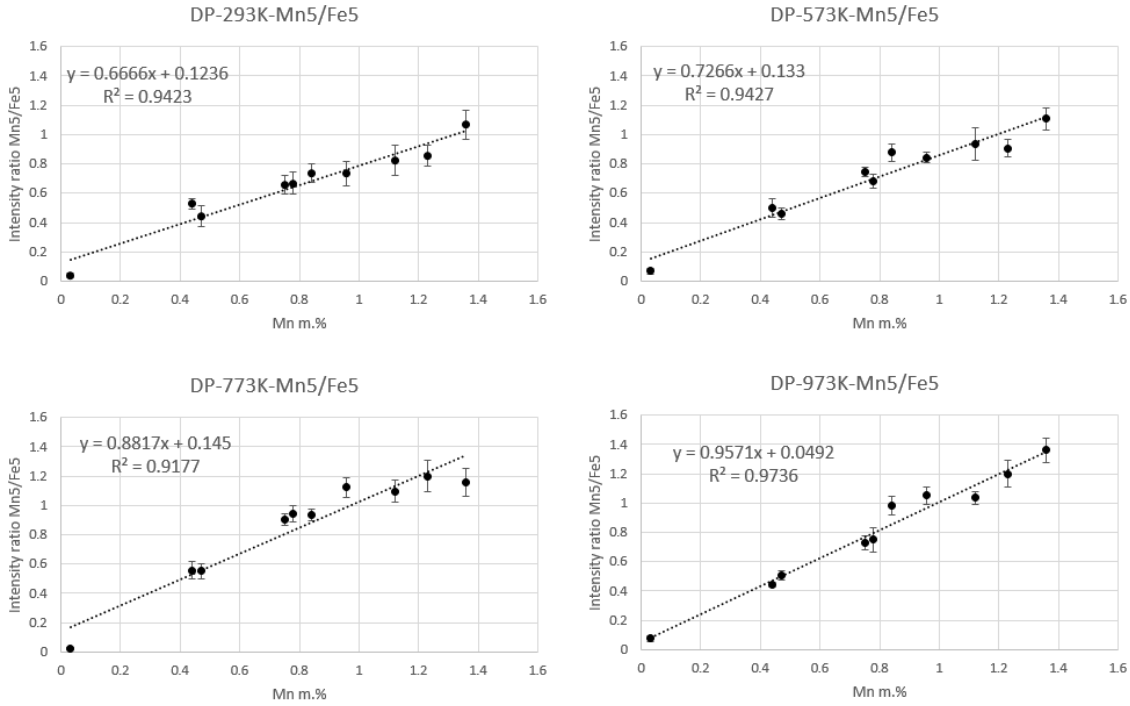

Fig. 6.15 Quantitative analysis results of Mn composition using long-short DP-LIBS under the simulated plant conditions (sample temperature from 20 ºC to 700 ºC).

Another phenomenon can be found in the results of Fig. 6.14 and Fig. 6.15 is that the parameters of the calibration curves. In Fig. 6.14, the calibration curves show a

remarkable different according to the sample temperature. As the sample temperature increasing, the slope of the calibration curves decreased. However, the phenomenon is quite different when using long-short DP-LIBS. The slope of the calibration curves is relative stable when the sample temperature changed. The results indicate that the long-short DP-LIBS can generate a stable plasma condition in the different sample temperature conditions. In the plant conditions, the temperature of measured target is usually unknown. Thus, if we want to apply LIBS technique to the real plant, an improved LIBS method is necessary. Long-short DP-LIBS seems a good choice for the measurement of steel products on the production line. Therefore, the combined temperature calibration curves are discussed in this study. Fig. 6.16 shows the compared results of the SP-LIBS and long-short DP-LIBS.

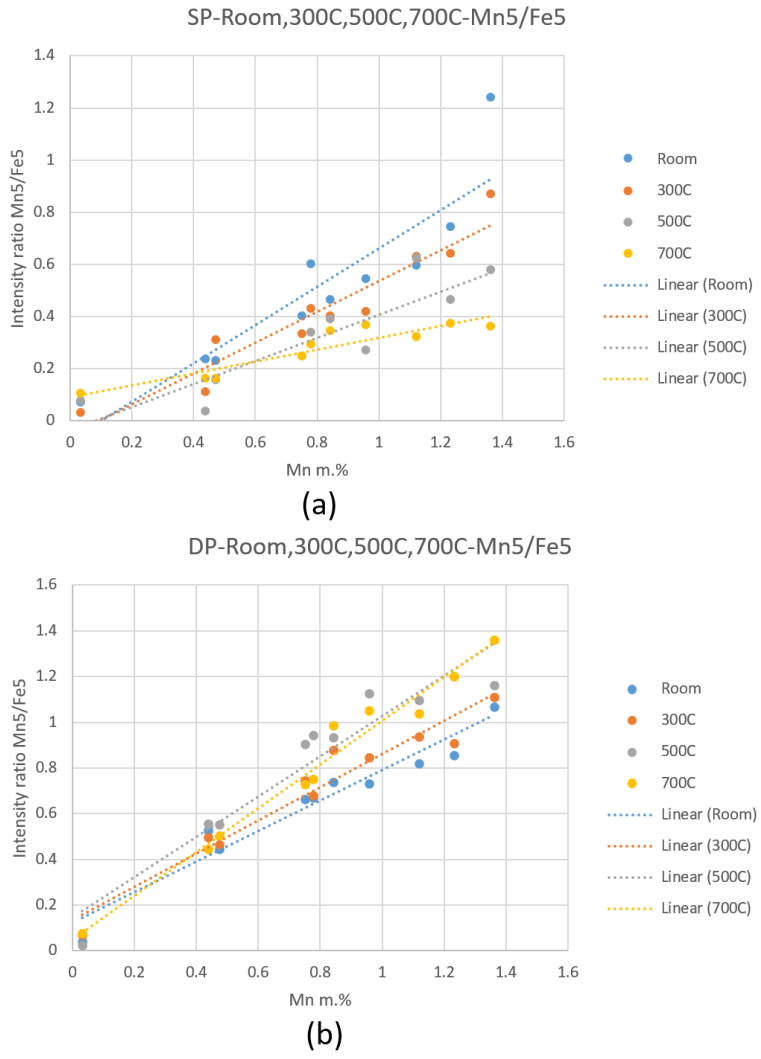

Fig. 6.16 Compared results of calibration curves using SP-LIBS and long-short DP-LIBS under the different sample temperature (Room, 300ºC, 500ºC and 700ºC). (a)

The calibration curves using SP-LIBS and (b) the calibration curves using long-short DP-LIBS.

According to Fig. 6.16, it can be seen that the calibration curves is fluctuant as the sample temperature changed from room temperature to 700^{o}C. However, the results using long-short DP-LIBS show a remark different with SP-LIBS. Under the different sample temperatures, the calibration curves of long-short DP-LIBS is relative stable and keep in a small range. It indicates that the long-short DP-LIBS is possible to be applied to the steel production line where the sample temperature is unknown. The influence of sample temperature is minor for the measurement of long-short DP-LIBS. This is another important merit for long-short DP-LIBS method.

6.6 Emission characteristics from the liquid steel samples

For the real application in the steel making plant, the measurement of liquid steel samples is very important for the monitoring and control of the composition of steel products. Compared than other chemical analysis methods, LIBS has a huge advantage in the measurement of liquid steel samples which are usually at a high temperature over than 1650 ^{o}C. The first experiment that used LIBS to directly analyze liquid steel was performed in 1991 [30]. A laser was mounted on an 80 t AOD converter used in the production of high-alloy steel. The beam entered the melt via a gas-flushed hole in the side-wall of the converter hole. A limit of detection (LOD) for carbon of ~200 μg/g was demonstrated in plant trials. The analysis of molten steel in a small crucible heated by an induction furnace was investigated with a laser beam that hit the free melt surface from the top [47]. LODs for carbon of 250 μg/g were reported for low-alloy steel samples with low carbon contents (150 to 1100 ppm).

A significant improvement in these detection limits was achieved by using double- and triple-pulse excitation [29]. Detection limits for the elements carbon, phosphorus, sulfur, manganese, nickel and chromium in solid low-alloy samples of less than 10 μg/g were achieved for the first time with LIBS using this approach. Dr. Noll's group from ILT Aachen also applied this technique of multiple pulse excitation to the multi-elemental analysis of liquid steel [46]. They investigated low-alloy steel grades, focusing on the light elements phosphorus, sulfur and carbon, using emission wavelengths in the vacuum ultraviolet. Calibration curves were determined for these light elements and also for nickel and chromium in a steel melt of 100 kg. It was demonstrated by them that LIBS can be used to analyze the light elements carbon, phosphorus and sulfur in liquid steel with estimated LODs in the range of 5–21 μg/g. VAI performed its first experiments with LIBS on liquid stainless steel samples in a laboratory in order to check the ability of the LIBS-based instrumentation to be applied online in the production of high-alloy steel [45]. Later on, Gruber's group carried out experiments with LIBS at the vacuum degassing plant of BÖHLER Edelstahl in Kapfenberg, Austria, where calibration curves for the main

elements were obtained at a working pressure of 1 mbar [179]. Another group started experiments on stainless steel samples that were heated up to 1200 °C in a laboratory furnace [180], and performed experiments based on a remote LIBS approach that investigated stainless steel samples above a melting temperature of ~1420 °C under atmospheric conditions [73].

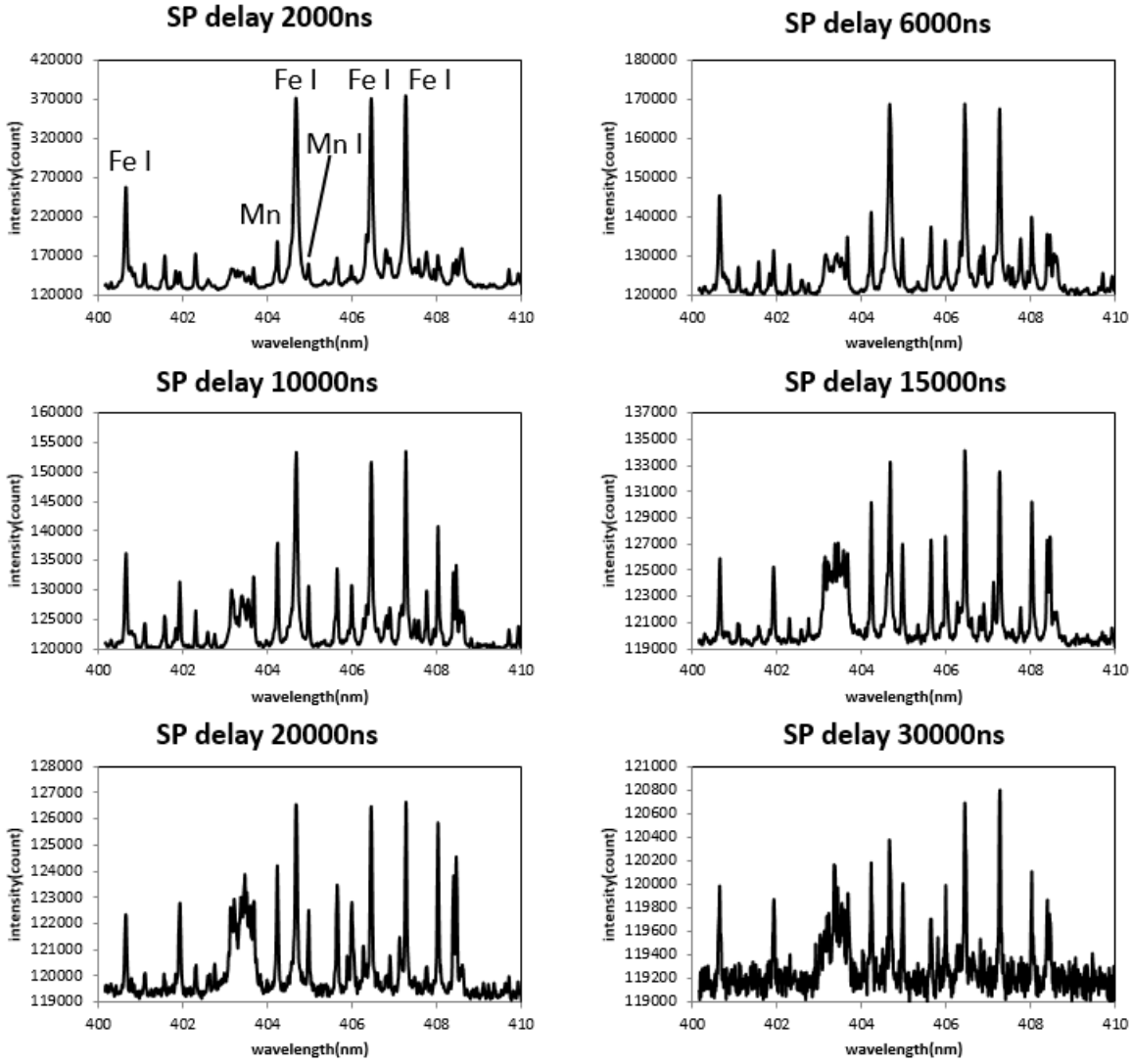

Fig. 6.17 Time resolved spectra from the liquid steel sample 30# using conventional SP-LIBS. SP means conventional SP-LIBS method.

In this work, we are trying to apply the long-short DP-LIBS to the composition measurement of liquid steel samples. In the condition of liquid steel, the temperature of sample is very high. Therefore, the stabilization of the plasma is important for the LIBS process. One of the merit of the long-short DP-LIBS method is the stabilization of plasma. To investigation the emission characteristics of the plasma generated from liquid steel samples, we have carried out the related experiments in the laboratory. Fig. 6.17 and Fig. 6.18 show the time resolved spectra of liquid

steel samples using SP-LIBS and long-short DP-LIBS respectively. The carbon steel sample with the name of 30# was selected to carry out the time resolved spectrum study.

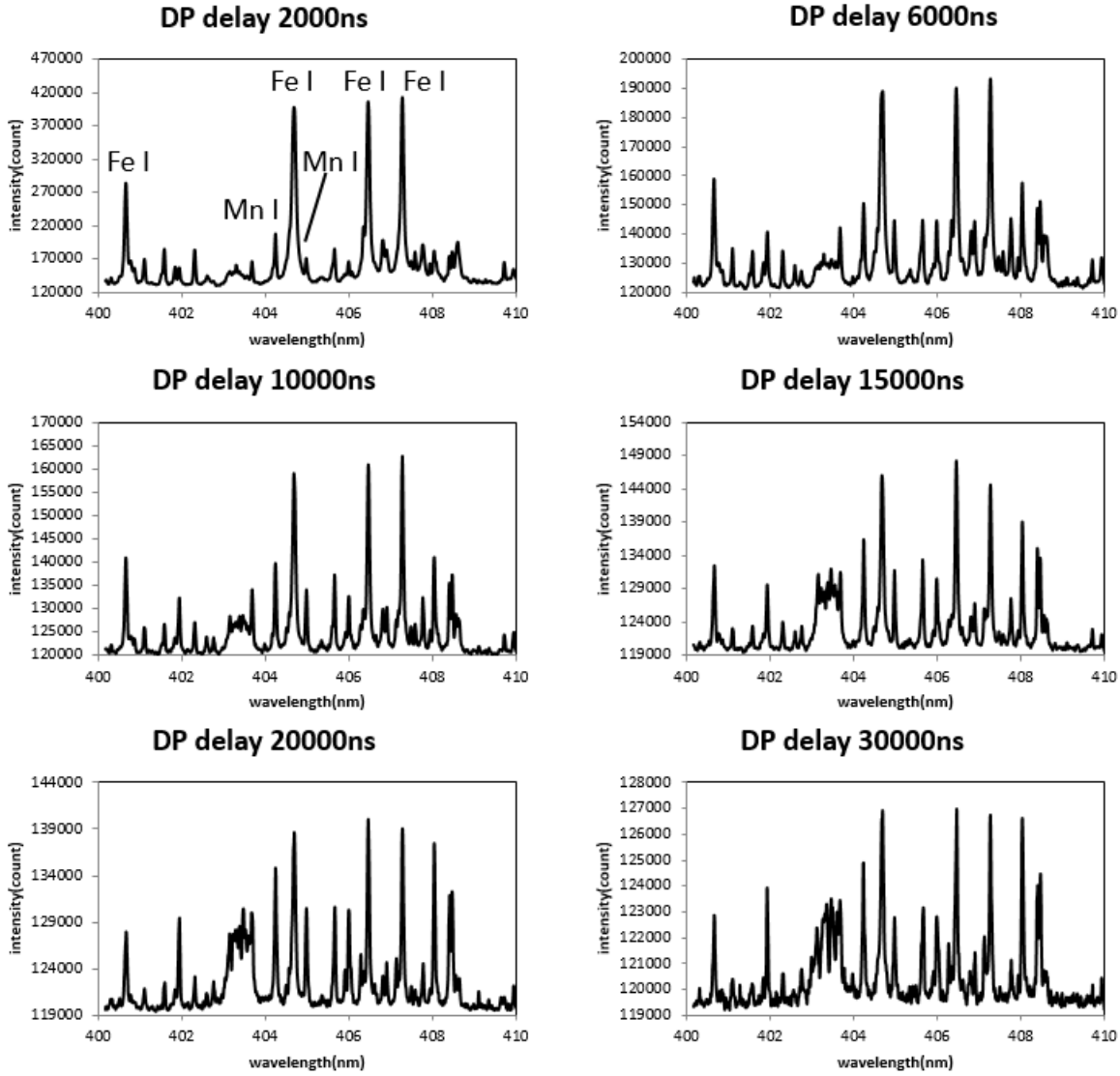

Fig. 6.18 Time resolved spectra from the liquid steel sample 30# using long-shrot DP-LIBS. DP means long-short DP-LIBS method.

According to the results of liquid steel in Fig. 6.18 and Fig. 6.19, it can be seen that the signal intensity was increased compared than room temperature for both of the method (conventional SP-LIBS and long-short DP-LIBS). At the same time, the plasma life time was extended because of the sample is already molting before the laser irradiation. Thus more laser energy is involved to the plasma generation process compared than room temperature and other solid phase experiments. When comparing the results of SP-LIBS and long-short DP-LIBS, it can be found that the signal intensity was increased in every delay time. It indicates that the plasma in long-short DP-LIBS conditions is stronger than that in conventional SP-LIBS. It is a meaningful results for the measurement ability of LIBS method. Another result is that the lifetime of plasma

in long-short DP-LIBS conditions is longer than that in SP-LIBS conditions. In the delay time of 30 us, there are still many iron and manganese lines can be used for the further analysis in the spectrum of long-short DP-LIBS. However, the signal of plasma becomes very weak in the spectrum of conventional SP-LIBS. This result indicates that the long pulse laser can extend the lifetime of the plasma in LIBS process.

6.7 Calibration curves for the analysis of liquid steel samples

According to the study on the emission characteristics of liquid steel, the further studies on the quantitative analysis of steel samples was carried out in this work. The steel samples with different Mn contents was molten by an induction furnace firstly. Then the molten samples were measured by conventional SP-LIBS and long-short DP-LIBS respectively. The measured results are compared between these two methods. Fig. 6.19 shows the calibration curves of SP-LIBS and long-short DP-LIBS.

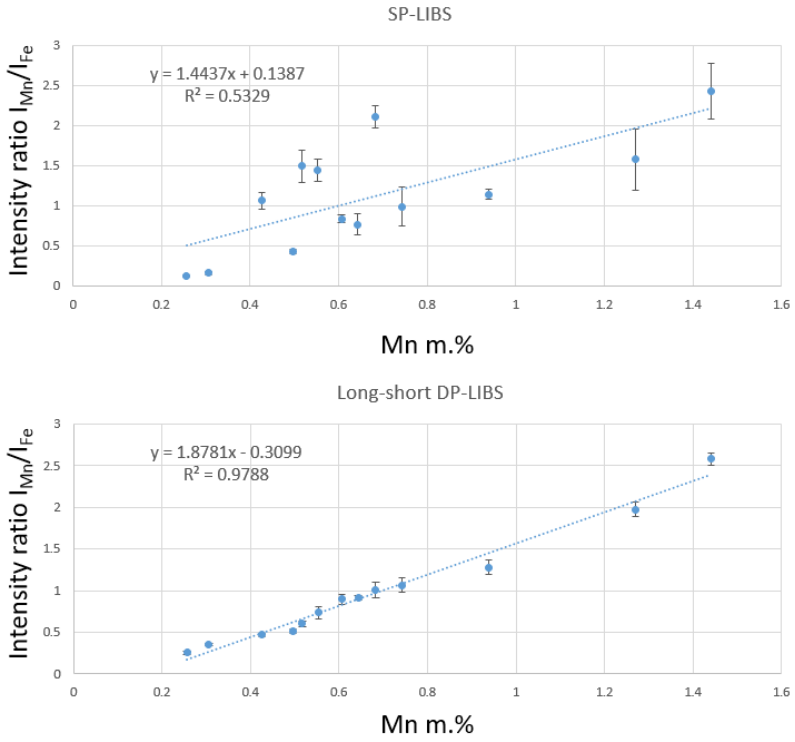

Fig. 6.19 The calibration curves of conventional SP-LIBS and long-short DP-LIBS which were measured according to a series of standard steel samples.

The calibration curve of long-short DP-LIBS is remarkable different with that of SP-LIBS. As well known, LIBS process is influenced by the matrix effects from the measured target. When the sample is molten, it means the sample condition is at a very hot temperature and in an unstable situation. Especially for the surface layer of the liquid steel, the content of this layer is unstable usually. However, the conventional SP-LIBS method can only measure the surface layer of the liquid steel, which of course increase the uncertainty of the LIBS measurement. Therefore,

for the liquid steel, conventional SP-LIBS can only obtain a calibration curve with a very low fitting parameter (R^2=0.5329). It is exciting that long-short DP-LIBS has obtained a stratified results for the measurement of liquid steel samples. The fitting parameters of the calibration curve is 0.9788 which is acceptable for the online analysis of steel composition. In addition, it can be found in Fig. 6.19 that the standard deviation of each experiment point in long-short DP-LIBS is lower than that in conventional SP-LIBS. It indicates that the long pulse laser also has the effect of plasma stabilization, which is consistent with the results of solid phase experimental results.

7 Conclusions and Outlook

7.1 Conclusions

The performance of collinear long-short DP-LIBS for steel samples was studied in this work. According to the experimental results, the performance improvement was discussed in several aspects hence the conclusions are drawn as follows.

7.1.1 Merits of long-short DP-LIBS

(1) The role of inter-pulse delay in signal enhancement for long-short DP-LIBS was investigated by experiments, the results showed that the optimal coupling of pre-heating and re-heating effects can be obtained by firing the short pulse at the middle of long pulse. Compared with SP-LIBS, long-short DP-LIBS has obtained 3-7 folds signal enhancement in the optimal inter-pulse delay.

(2) Through the observation of plasma, the plasma images showed the remarkable differences between SP-LIBS and long-short DP-LIBS. The plasma was bigger and had a longer lifetime in long-short DP-LIBS condition. Moreover, the observed images of long pulse LIBS suggested that the long pulse can't generate the plasma due to the low power density.

(3) The variation of plasma temperature showed that the plasma was maintained at a high and stable temperature. The variation of time-resolved intensity ratio was different for SP-LIBS and long-short DP-LIBS. I_{Mn}/I_{Fe} linearly increased with delay time in SP-LIBS condition, whereas, it showed a remarkable stabilization around the delay time of 3000 ns in long-short DP-LIBS condition. These phenomena indicated that the plasma was stabilized by using the long-pulse-width laser beam.

(4) Through the testing at different sample temperatures, the measured spectra were consistent for long-short DP-LIBS, whereas, the spectra were significantly different for SP-LIBS. The results demonstrated that long-short DP-LIBS can be used for the online measurement of steel production line, in where the temperature of target is unknown.

7.1.2 Measurement of steel samples under the simulated plant conditions

(1) The long pulse made it possible to obtain clear spectra from the steel washers which had an obvious rusty layer. Through the study on the crater morphology, the improvement of detection ability can be attributed to the cleaning effect of long pulse. This result indicated that long-short DP-LIBS can be used in steel production lines, in where severe oxidation is difficult to be avoided.

(2) The emission intensity was obviously enhanced by long-short DP-LIBS because of the preheating effect of the long pulse. The comparison of spectra showed that more spectral lines were available for quantitative analysis from the spectrum of long-short DP-

LIBS. This result suggested that long-short DP-LIBS can obtain more spectral information under the same experimental conditions.

(3) The measured results of long-short DP-LIBS showed a better linearity. The determination coefficients (R2) was 0.988 for the calibration curve of long-short DP-LIBS, which is acceptable for the industrial application. Moreover, the larger slope of calibration curve for long-short DP-LIBS indicated that the effect of self-absorption was eliminated by the long pulse, which therefore improved the analytical performance of LIBS.

(4) The prediction results showed that the precision and accuracy of long-short DP-LIBS were better than those of SP-LIBS. The mean RSD% was reduced from 29.3% to 10.5% and the mean REP% was reduced from 94.9% to 4.9%.The improvement can be attributed to the stabilized plasma which was generated by long-short DP-LIBS process. The simulated prediction experiments demonstrated that the analytical performance of LIBS can be improved by adding a long pulse to the traditional SP-LIBS.

(5) The measurement results of liquid steel showed that the conventional SP-LIBS can’t obtain a satisfied calibration curve due to the unstable sample condition. However, long-short DP-LIBS showed an acceptable performance for the measurement of liquid steel samples. The fitting parameters of the calibration curve is 0.9788 for the long-short DP-LIBS, which is only 0.5329 for the SP-LIBS. At the same time, the standard deviation of the measured intensity ratio values are relative low in the long-short DP-LIBS results. It proved that the plasma is stabilized by the long pulse laser beam.

7.2 Outlooks

Based on the experiment results in this dissertation, there are also some outlooks for the long-short DP-LIBS. The quantitative analysis of other elements in steel samples will be further studied using the long-short DP-LIBS method. The quantitative measurement of multi-elements in some terrible plants situations are expected to be acceptable using long-short DP-LIBS. The LOD of non-metallic element in steel samples will also be investigated using the long-short DP-LIBS method, such as carbon, silicon, sulphur, phosphorus, et al. Moreover, there is a requirement of underwater measurement of steel target in the fields such as mineral production, environmental protection, et al. The plasma will disappear soon under the water due to the cooling effect and pressure of water. The effects of long pulse laser in long-short DP-LIBS are desirable for the underwater application of LIBS.

References

[1] R. Noll, Laser-Induced Breakdown Spectroscopy: Fundamentals and Applications, Springer-Verlag, Berlin Heidelberg, 2012.
[2] Y. Deguchi, Industrial Applications of Laser Diagnostics, CRS Press, Taylor & Francis: New York, 2011.
[3] A. Miziolek, V. Palleschi, I. Schechter, Laser-Induced Breakdown Spectroscopy (LIBS), Cambridge University Press, New York, 2006.
[4] S. Qiao, Y. Ding, D. Tian, L. Yao, G. Yang, A review of Laser-Induced Breakdown Spectroscopy for analysis of geological materials, Appl. Spectros. Rev. 50(2015)1-26.
[5] A. M. Popov, F. Colao, R. Fantoni, Enhancement of LIBS signal by spatially confining the laser-induced plasma, J. Anal. At. Spectrom. 24(2009)602-604.
[6] A. Hussain, Q. Li, Z. Hao, X. Gao, J. Lin, The effect of an external magnetic field on the plume expansion dynamics of laser-induced aluminum plasma, Plasma Sci. Technol. 17(2015)693-698.
[7] K. X. Li, W. D. Zhou, Q. M. Shen, Z. J. Ren, B. J. Peng, Laser ablation assisted spark induced breakdown spectroscopy on soil samples, J. Anal. At. Spectrom. 25(2010)1475-1481.
[8] M. V. Belkov, V. S. Burakov, A. De Giacomo, V. V. Kiris, S. N. Raikov, N. V. Tarasenko, Comparison of two laser-induced breakdown spectroscopy techniques for total carbon measurement in soils, Spectrochim. Acta Part B 64(2009)899-904.
[9] K. Ali, M. Tampo, K.Akaoka, M. Miyabe, I. Wakaida, Enhancement of LIBS emission using antenna-coupled microwave, Opt. Express. 21(2013)29755-29768.
[10] Jan Viljanen, ZhiweiSun, Zeyad T. Alwahabi, Microwave assisted laser-induced breakdown spectroscopy at ambient conditions, Spectrochim. Acta Part B 118(2016)29-36.
[11] Y. Liu, M. Baudelet, M. Richardson, Elemental analysis by microwave-assisted laser-induced breakdown spectroscopy: Evaluation on ceramics, J. Anal. At. Spectrom. 25(2010)1316-1323.
[12] G. Cristoforetti, S. Legnaioli, V. Palleschi, A. Salvetti, E. Tognoni, Characterization of a collinear double pulse laser-induced plasma at several ambient gas pressures by spectrally- and time-resolved imaging, Appl. Phys. 80(2005)559-568.
[13] R. Sanginés, V. Contreras, H. Sobral, A. Robledo-Martinez, Optimal emission enhancement in orthogonal double-pulse laser-induced breakdown spectroscopy, Spectrochim. Acta Part B 110(2015)139-145.
[14] Chao Song, Xun Gao, Yan Shao, Pre-ablation laser parameter effects on the spectral enhancement of 1064 nm/1064 nm dual-pulse laser induced breakdown spectroscopy, Optik 127(2016)3979–3983.

[15] M. E. Asgill, M. S. Brown, K. Frische, W. M. Roquemore, D. W. Hahn, Double-pulse and single-pulse laser-induced breakdown spectroscopy for distinguishing between gaseous and particulate phase analytes, Appl. Opt. 49(2010)C110-C119.
[16] S. S. Harilal, P. K. Diwakar, A. Hassanein, Electron-ion relaxation time dependent signal enhancement in ultrafast double-pulse laser-induced breakdown spectroscopy, Appl. Phys. Lett. 103(2013)041102.
[17] V. I. Babushok, F. C. DeLucia, J. L. Gottfried, C. A. Munson, A. W. Miziolek, Double pulse laser ablation and plasma: Laser Induced Breakdown Spectroscopy signal enhancement, Spectrochim. Acta Part B. 61(2006)999-1014.
[18] Y. Lu, V. Zorba, X. L. Mao, R. Zheng, R. E. Russo, UV fs–ns double-pulse laser induced breakdown spectroscopy for high spatial resolution chemical analysis, J. Anal. At. Spectrom. 28(2013)743-748.
[19] R. Ahmed, M. A. Baig, A comparative study of single and double pulse laser induced breakdown spectroscopy, J. Anal. At. Spectrom. 106(2009)033307.
[20] C. Duke, H. Fischer, H.J. Kluge, H. Kremmling, Th. K¨uhl, E.W. Otten, Determination of isotope shift of 190Hg by on-line laser spectroscopy. Phys. Lett. 60A, 303–306 (1977).
[21] G. Gerber, Die Momentaufnahme der Molek¨ulspaltung. Phys. Bl¨atter 55, 23–25 (1999).
[22] M. Proffitt, A. Langford, Ground based differential LIDAR system for day or night measurement of ozone throughout the free troposphere. Appl. Optics 36, 2568–2585 (1997).
[23] R. Mihalcea, D. Baer, R. Hanson, A diode-laser absorption sensor system for combustion emission measurements. Meas. Sci. Technol. 9, 327–338 (1998).
[24] L. Paksy, B. Nemet, A. Lengyel, L. Kozma, J. Czekkel, Production control of metal alloys by laser spectroscopy of molten metals. Part 1. Preliminary investigation. Spectrochim. Acta B 51 279–290 (1996).
[25] R. Noll, L. Peter, I. M¨onch, V. Sturm, Automatic laser-based identification and marking of high-grade steel qualities, in Progress in Analytical Chemistry in the Steel and Metals Industries, ed. by R. Tomellni (European Communities, Luxembourg, 1999), pp. 345–351.
[26] D. Cremers, The analysis of metals at a distance using laser-induced breakdown spectroscopy. Appl. Spectrosc. 41, 572–579 (1987).
[27] R. Adrain, J. Watson, Laser microspectral analysis: a review of principles and applications. J. Phys. D Appl. Phys. 17, 1915–1940 (1984).
[28] E. Runge, R. Minck, F. Bryan, Spectrochemical analysis using a pulsed laser source. Spectrochim. Acta 20, 733–736 (1964).
[29] V. Sturm, L. Peter, R. Noll, Steel analysis with laser-induced breakdown spectrometry in the vacuum ultraviolet. Appl. Spectrosc. 54, 1275–1278 (2000).
[30] C. Carlhoff, Laserinduzierte Emissionsspektroskopie f¨ur die Direktanalyse von fl¨ussigem Stahl im Konverter. Laser Optoelektr. 23, 50–52 (1991).

[31] H. Sattler, Metallschrotte nach Analyse automatisch sortieren. Materialpr¨ufung 35, 312–315 (1993).
[32] P. Peuser, N. Schmitt, Dioden-gepumpte Festk¨orperlaser (Springer-Verlag, New York, 1995).
[33] J. R. Freeman, P. K. Diwakar, S. S. Harilal, A. Hassanein, Improvements in discrimination of bulk and trace elements in long-wavelength double pulse LIBS. Spectrochim. Acta Part B. 102(2014)36-41.
[34] R. Noll, R. Sattmann, V. Sturm, S. Winkelmann, Space- and time-resolved dynamics of plasmas generated by laser double pulses interacting with metallic samples, J. Anal. At. Spectrom. 19(2004)419-428.
[35] D. K. Killinger, S. D. Allen, R. D. Waterbury, C. Stefano, E. L. Dottery, Enhancement of Nd:YAG LIBS emission of a remote target using a simultaneous CO2 laser pulse, Opt. Express. 15(2007)12905-12915.
[36] A. Pal, R. D. Waterbury, E. L. Dottery, D. K. Killinger, Enhanced temperature and emission from a standoff 266 nm laser initiated LIBS plasma using a simultaneous 10.6 μm CO2 laser pulse, Opt. Express. 17(2009)8856-8870.
[37] M. Weidman, M. Baudelet, S. Palanco, M. Sigman, P. J. Dagdigian, M. Richardson, Nd:YAG-CO2 double-pulse Laser Induced Breakdown Spectroscopy of organic films, Opt. Express. 18(2010)259-266.
[38] J. Vrenegor, R. Noll, V. Sturm. “Investigation of matrix effects in laser-induced breakdown spectroscopy plasmas of high-alloy steel for matrix and minor elements”. Spectrochim. Acta Part B 2005. 60: 1083-1091.
[39] C.M. Li, Z.M. Zou, X.Y. Yang, Z.Q. Hao, L.B. Guo, X.Y. Li, Y.F. Lu, X.Y. Zeng. “Quantitative analysis of phosphorus in steel using laser-induced breakdown spectroscopy in air atmosphere”. J. Anal. At. Spectrom. 2014. 29: 1432-1437.
[40] H. Balzer, M. Hoehne, R. Noll, V. Sturm. “New approach to online monitoring of the Al depth profile of the hot-dip galvanised sheet steel using LIBS”. Anal. Bioanal. Chem. 2006. 385: 225-233.
[41] M. A. Khater. “Laser-induced breakdown spectroscopy for light elements detection in steel: State of the art”. Spectrochim. Acta Part B 2013. 81: 1-10.
[42] H. Balzer, S. Hölters, V. Sturm, R. Noll. “Systematic line selection for online coating thickness measurements of galvanised sheet steel using LIBS”. Anal. Bioanal. Chem. 2006. 385: 234-239.
[43] C. Meinhardt, V. Sturm, R. Fleige, C. Fricke-Begemann, R. Noll. “Laser-induced breakdown spectroscopy of scaled steel samples taken from continuous casting blooms”. Spectrochim. Acta Part B 2016. 123: 171-178.

[44] S. Yao, J. Lu, K. Chen, S. Pan, J. Li, M. Dong. “Study of laser-induced breakdown spectroscopy to discriminate pearlitic/ferritic from martensitic phases”. Appl. Surf. Sci. 2011. 257: 3103-3110.
[45] J. Gruber, J. Heitz, H. Strasser, D. Bauerle, N. Ramaseder. “Rapid in-situ analysis of liquid steel by laser-induced breakdown spectroscopy”. Spectrochim. Acta Part B 2001. 56: 685-693.
[46] L. Peter, V. Sturm, R. Noll. “Liquid steel analysis with laser-induced breakdown spectrometry in the vacuum ultraviolet”. Appl. Optics. 2003. 42: 6199-6204.
[47] C. Aragon, J.A. Aguilera, J. Campos. “Determination of carbon content in molten steel using laser-induced breakdown spectroscopy”. Appl. Spectrosc. 1993. 47: 606-608.
[48] H. K. Sanghapi, K. K. Ayyalasomayajul, F. Y. Yueh, J. P. Singh, D. L. McIntyre, J. C. Jain, J. Nakano. “Analysis of slags using laser-induced breakdown spectroscopy”. Spectrochim. Acta Part B 2016. 115: 40-45.
[49] C.M. Ahamer, S. Eschlböck-Fuchs, P.J. Kolmhofer, R. Rössler, N. Huber, J.D. Pedarnig. “Laser-induced breakdown spectroscopy of major and minor oxides in steel slags: Influence of detection geometry and signal normalization”. Spectrochim. Acta Part B 2016. 122: 157-164.
[50] F. Boué-Bigne. “Laser-induced breakdown spectroscopy and multivariate statistics for the rapid identification of oxide inclusions in steel products”. Spectrochim. Acta Part B 2016. 119: 25-35.
[51] A. Demidov, S. Eschlböck-Fuchs, A.Y. Kazakov, I.B. Gornushkin, P.J. Kolmhofer, J.D. Pedarnig, N. Huber, J. Heitz, T. Schmid, R. Rossler, U. Panne. “Monte Carlo standardless approach for laser induced breakdown spectroscopy based on massive parallel graphic processing unit computing”. Spectrochim. Acta Part B 2016. 125: 97-102.
[52] J.D. Pedarnig, M.J. Haslinger, M.A.Bodea, N.Huber, H. Wolfmeir, J. Heitz. “Sensitive detection of chlorine in iron oxide by single pulse and dual pulse laser-induced breakdown spectroscopy”. Spectrochim. Acta Part B 2014. 101: 183-190.
[53] N. Hubera, S. Eschlböck-Fuchsa, H. Scherndlb, A. Freimundb, J. Heitza, J.D. Pedarnig. “In-line measurements of chlorine containing polymers in an industrial waste sorting plant by laser-induced breakdown spectroscopy”. Appl. Surf. Sci. 2014. 302: 280-285.
[54] L. Sun, H. Yu, Z. Cong, Y. Xin, Y. Li, L. Qi. “In situ analysis of steel melt by double-pulse laser-induced breakdown spectroscopy with a Cassegrain telescope”. Spectrochim. Acta Part B 2015. 112: 40-48.
[55] F. Boué-Bigne. “Laser-induced breakdown spectroscopy applications in the steel industry: Rapid analysis of segregation and decarburization”. Spectrochim. Acta Part B 2008. 63: 1122-1129.
[56] R. Noll, V. Sturm, Ü. Aydin, D. Eilers, C. Gehlen, M. Höhne, A. Lamott, J. Makowe, J. Vrenegor, Laser-induced breakdown spectroscopy—From research to industry, new frontiers for process control, Spectrochim. Acta Part B 63(2008)1159-1166.

[57] Z. Wang, Y. Deguchi, R. Liu, A. Ikutomo, Z. Zhang, D. Chong, J. Yan1., J. Liu, F.J. Shiou, Emission characteristics from laser-induced plasma using collinear long and short dual-pulse LIBS, Appl. Spectrosc. 71(2017)2187-2198.
[58] P.J. Kolmhofer, S. Eschlböck-Fuchs, N. Huber, R. Rössler, J. Heitz, J.D. Pedarniga, Calibration-free analysis of steel slag by laser-induced breakdown spectroscopy with combined UV and VIS spectra, Spectrochim. Acta Part B 106(2015)67-74.
[59] G. Lorenzetti, S. Legnaioli, E. Grifoni, S. Pagnotta, V. Palleschi, Laser-based continuous monitoring and resolution of steel grades in sequence casting machines, Spectrochim. Acta Part B 112(2015)1-5.
[60] L.F. Qi, L.X. Sun, Y. Xin, Z.B. Cong, Y. Li, H.B. Yu, Application of stand-off double-pulse Laser-Induced Breakdown Spectroscopy in elemental analysis of magnesium alloy, Plasma Sci. Technol. 17(2015)676-681.
[61] P.K. Diwakar, S.S. Harilal, J.R. Freeman, A. Hassanein, Role of laser pre-pulse wavelength and inter-pulse delay on signal enhancement in collinear double-pulse laser-induced breakdown spectroscopy, Spectrochim. Acta Part B 87(2013)65-73.
[62] X. Jiang, P. Hayden, R. Laasch, J.T. Costello, E.T. Kennedy, Inter-pulse delay optimization in dual-pulse laser induced breakdown vacuum ultraviolet spectroscopy of a steel sample in ambient gases at low pressure, Spectrochim. Acta, Part B 86(2013) 66-74.
[63] R.W. Coons, S.S. Harilal, S.M. Hassan, A. Hassanein, The importance of longer wavelength reheating in dual-pulse laser-induced breakdown spectroscopy, Appl. Phys. B 107(2012) 873-880.
[64] G. Cristoforetti, S. Legnaioli, L. Pardini, V. Palleschi, A. Salvetti, E. Tognoni, Spectroscopic and shadow graphic analysis of laser induced plasmas in the orthogonal double pulse pre-ablation configuration, Spectrochim. Acta, Part B 61 (2006) 340-350.
[65] M. Corsi, G. Cristoforetti, M. Giuffrida, M. Hidalgo, S. Legnaioli, V. Palleschi, A. Salvetti, E. Tognoni, C. Vallebona, Three-dimensional analysis of laser induced plasmas in single and double pulse configuration, Spectrochim. Acta, Part B 59(2004) 723-735.
[66] H. Sobral, C. Sánchezaké, R. Sanginés, E. Alvarezzauco, K., Jiménezdurán, Photoacoustic and spectroscopic characterization of the ablation process in orthogonal double-pulse configuration, J. Phys. D: Appl. Phys. 44(2011)085201.
[67] National Institute of Standards and Technology, NIST Atomic Spectra Database Lines Form. http://physics.nist.gov/PhysRefData/ASD/lines_form.html, 2009 (accessed 17.10.10).
[68] Y. Wang, A. Chen, S. Li, L. Sui, D. Liu, D. Tian, Y. Jiang, M. Jin, Enhancement of laser-induced Fe plasma spectroscopy with dual-wavelength femtosecond double-pulse, J. Anal. At. Spectrom. 31(2015)497-505.
[69] D.X. Sun, M.G. Su, C.Z. Dong, G.H. Wen, A comparative study of the Laser Induced Breakdown Spectroscopy in single- and collinear double-pulse laser geometry, Plasma Sci. Technol. 16(2014)374-379.

[70] R. Sanginés, H. Sobral, Time resolved study of the emission enhancement mechanisms in orthogonal double-pulse laser-induced breakdown spectroscopy, Spectrochim. Acta, Part B 88(2013) 150-155.
[71] Z. Hao, L. Guo, C. Li, M. Shen, X. Zou, X. Li, Y. Lu, X. Zeng, Sensitivity improvement in the detection of V and Mn elements in steel using laser-induced breakdown spectroscopy with ring-magnet confinemen, J. Anal. At. Spectrom. 29(2014)2039-2314.
[72] G. Hubmer, R. Kitzberger, K. Morwald, Application of LIBS to the in-line process control of liquid high-alloy steel under pressure, Anal. Bioanal. Chem. 385 (2006) 219–224.
[73] S. Palanco, S. Conesa, J.J. Laserna, Analytical control of liquid steel in an induction melting furnace using a remote laser induced plasma spectrometer, J. Anal. Atom. Spectrom 19 (2004) 462–467.
[74] L. Sun, Haibin Yu, Y. Xin, Zhibo Cong, H. Kong, On-line monitoring of molten steel compositions by laser-induced breakdown spectroscopy, Chin. J. Lasers 38 (2011) 0915002.
[75] L. Sun, H. Yu, Z. Cong, Y. Xin, On-line semi-quantitative analysis of molten steel composition using laser-induced breakdown spectroscopy, Chin. J. Sci. Instrum. 32 (2011) 2602–2608.
[76] L. Sun, Y. Xin, Z. Cong, Y. Li, L. Qi, Online compositional analysis of molten steel by laser-induced breakdown spectroscopy, Adv. Mater. Res. 694–697 (2013) 1260–1266.
[77] Li YY, Zhao SD, Fan SQ, Yan GH (2013) Study on the material characteristic and process parameters of the open-die warm extrusion process of spline shaft with 42CrMo steel, J Alloys Comp 571: 12–20.
[78] Zhang DW, Li YT, Fu JH (2007) Mechanics analysis on precise forming process of external spline cold rolling, Chin J Mech Eng-En 20: 54-58.
[79] Neugebauer R, Klug D, Hellfritzsch U (2007) Description of the interactions during gear rolling as a basis for a method for the prognosis of the attainable quality parameters, Prod Eng Res Devel 1: 253-257.
[80] Zou L, Xia JC, Wang XY, Hu GA (2003) Optimization of die profile for improving die life in the hot extrusion process, J Mater Process Technol 142: 659–664.
[81] Lee RS, Sheu JJ, Gau YJ (1991) Optimum die-surface design of gear-spline extrusions using a general surface model, J Mater Process Technol 28:365–382.
[82] Neugebauer R, Putz M, Hellfritzsch U (2007) Improved process design and quality for gear manufacturing with flat and round rolling. Ann CIRP 56(1):307–312.
[83] Zhang DW, Zhao SD (2014) New method for forming shaft having thread and spline by rolling with round dies. Int J Adv Manuf Technol 70:1455–1462.
[84] Kao YC, Cheng HY, She CH (2006) Development of an integrated CAD/CAE/CAMsystemon taper-tipped thread-rolling die-plates. J Mater Process Technol 177:98–103.

[85] Domblesky JP, Feng F (2002) A parametric study of process parameters in external thread rolling. J Mater Process Technol 121:341–349.
[86] Quan GZ, Tong Y, Luo G, Zhou J (2010) A characterization for the flow behavior of 42CrMo steel, Comput Mater Sci 50: 167-171.
[87] Lin YC, Chen MS, Zhang J (2009) Modeling of flow stress of 42CrMo steel under hot compression, Mater Sci Eng A 499: 88-92.
[88] Li YY, Zhao SD, Fan SQ, Zhong B (2013) Plastic properties and constitutive equations of 42CrMo steel during warm forming process, Mater Sci Technol 30(6): 645-652.
[89] Liu ZQ, Song JL, Qi HP, Li YT, Li XD (2010) Parameters and experiments on the precision forming process of spline cold rolling. Appl Mech Mater 34–35:646–650.
[90] Zhang DW, Zhao SD, Wu SB, Zhang Q, Fan SQ, Li JX (2015) Phase characteristic between dies before rolling for thread and spline synchronous rolling process. Int J Adv Manuf Technol 81:513–528.
[91] Faiz J and Moayed-Zadeh K. Design of switched reluctance machine for starter/generator of hybrid electric vehicle. Electric Power Systems Research 2005; 75: 153-160.
[92] Rannan MA, Azidin FA and Mohamed A. Hybrid electric vehicles and their challenges: a review. Renew Sustain Energy Rev 2014; 29: 135-150.
[93] Xu W, Zhu J, Guo Y, Wang S, Wang Y and Shi Z. Survey on electrical machines in electrical vehicles. In: International Conference on Applied Superconductivity and Electromagnetic Devices, Chengdu, China, 25-27 September 2009, pp.167-170. ASEMD2009.
[94] Kamiya M. Development of traction drive starters for the Toyota hybrid systems. IEEE Trans. Industry Application 2006; 4:473-479.
[95] Gladwin D, Stewart P and Stewart J. A novel genetic programming approach to the design of engine control systems for the voltage stabilization of hybrid electric vehicle generator outputs. Proceedings of the Institution of Mechanical Engineers Part D Journal of Automobile Engineering 2011; 225: 1334-1346.
[96] Bojoi R, Cavagnino A, Cossale M and Tenconi A. Design trade-off and experimental validation of multiphase starter generators for 48V mini-hybrid powertrain. Electric Vehicle Conference IEEE 2015; 223: 471-484.
[97] Sun X, Xue Z, Xu X, Chen L, Yang Z and Han S. Thermal analysis of a segmented rotor switched reluctance motor used as the belt-driven starter/generator for hybrid electric vehicles. Journal of Low Power Electronics 2016; 12:277-284.
[98] Wang C-L, Yin C-L, Luo G, Guo Z-Q and Gai F-X. Start and acceleration optimization of a parallel hybrid electric vehicle. Proceedings of the Institution of Mechanical Engineers Part D Journal of Automobile Engineering 2011; 225: 591-607.
[99] Lee C and Krishnan R. New designs of a two-phase e-core switched reluctance machine by optimizing the magnetic structure for a specific application: concept, design, and analysis. IEEE Trans. Industry Application 2009; 45:1804-1814.

[100] Siadatan A, Afjei E, Torkaman H and Rafie M. Design, simulation and experimental results for a novel type of two-layer 6/4 three-phase switched reluctance starter/generator. Energy Convers Manage 2013; 71:199-207.
[101] Oh SG and Krishnan R. Two-phase SRM with flux-reversalfree stator: concept, analysis, design, and experimental verification. IEEE Trans. Industry Application 2007; 43: 1247-1257.
[102] Torkaman H and Afjei E. Comparison of three novel types of two-phase switched reluctance starters using finite element method. Prog Electrom Res 2012; 125: 151-164.
[103] Wang HJ, Lee DH, Park TH and Ahn JW. Hybrid stator-pole switched reluctance starter to improve radial force for bearingless application. Energy Convers Manage 2012; 52: 1371–1376.
[104] Arihara H and Akatsu K. Basic properties of an axial-type switched reluctance starter. IEEE Trans. Industry Application 2013; 49: 59–65.
[105] Ding W. Comparative study on dual-channel switched reluctance generator performances under single- and dual-channel operation modes. IEEE Trans Energy Convers 2012; 27: 680–688.
[106] Daldaban F and Ustkoyuncu N. Multi-layer switched reluctance starter to reduce torque ripple. Energy Convers Manage 2008; 49: 974–979.
[107] Torkaman H, Afjei E and Toulabi MS. New double-layer-per-phase isolated switched reluctance starter: concept, numerical analysis, and experimental confirmation. IEEE Trans Industry Electron 2012; 59: 830–838.
[108] Daldaban F and Ustkoyuncu N. A novel linear switched reluctance starter for railway transportation systems. Energy Convers Manage 2010; 51: 465–469.
[109] Daldaban F and Ustkoyuncu N. New disc type switched reluctance starter for high torque density. Energy Convers Manage 2007; 48: 2424–2431.
[110] Li XG and Lipo TA. A synchronous/permanent magnet hybrid AC machine. IEEE Trans on Energy Conversion 2000; 15: 203-210.
[111] Dorrell D, Parsa L and Boldea I. Automotive electric motors, generators, and actuator drive systems with reduced or no permanent magnets and innovative design concepts. IEEE Transactions on Industrial Electronics 2014; 61: 5693-5695.
[112] Tutelea LN, Deaconu SI, Boldea I and Popa GN. Dual rotor single- stator axial air gap PMSM motor/generator drive for high torque vehicles applications. IOP Conference Series Materials Science and Engineering 2014; 57:127-132.
[113] Fodorean D, Djerdir A, Viorel IA and Miraoui A. A double excited synchronous machine for direct drive application-Design and prototype tests. IEEE Trans on Energy Convers 2007; 22: 656-665.
[114] Ferreira C, Jones SR, Heglund WS and Jones WD. Detailed design of a 30-kW switched reluctance starter/generator system for a gas turbine engine application. Industry Applications Society Meeting Conference Record of the IEEE 1993; 31: 553-561.

[115] Ding W, Liu L, Hu Y and Liu Y. Modular switched reluctance machine with e-core stators and segmental rotors for high reliability applications. International Journal of Electrical Power & Energy Systems 2014; 62: 496-506.
[116] Zan X, Huo Y and Gu J. Optimization research of turn-on angle and turn-off angle based on switched reluctance starter/generator system. Electrical and Computer Engineering 2015; 864-869.
[117] Lee CS, Kim JH and Hong JP. Core loss effects on electrical steel sheet of wound rotor synchronous motor for integrated starter generator. Journal of Magnetics 2015; 20: 148-154.
[118] Wrobel R. Design of a brushless pm starter-generator for low-cost manufacture and a high-aspect-ratio mechanical space envelope. IEEE Energy Conversion Congress & Exposition 2015; 813-820.
[119] Sulaiman E, Ahmad MZ, Kosaka T and Matsui N. Design optimization studies on high torque and high power density hybrid excitation flux switching starter for HEV. Procedia Engineering, 2013; 53: 312-322.
[120] Sulaiman E, Kosaka T and Matsui N. Design and analysis of high-power/high-torque density dual excitation switched-flux machine for traction drive in HEVs. Renewable and Sustainable Energy Reviews 2014; 34: 517-524.
[121] Amara Y, Vido L, Gabsi M, Hoang E, Ben Ahmed AH and Lecrivain M. Hybrid excitation synchronous machines: Energy-efficient solution for vehicles propulsion. IEEE Transaction Vehicle Technology 2009; 58: 2137-2149.
[122] Sulaiman E, Kosaka T and Matsui N. Design optimization and performance of a novel 6-Slot 5-Pole PMFSM with hybrid excitation for hybrid electric vehicle. IEEJ Transaction on Industrial Application 2011; 132: 312-322.
[123] Ahmad MZ, Sulaiman E, Haron ZA and Kosaka T. Impact of rotor pole number on the characteristics of outer-rotor hybrid excitation flux switching starter for in-wheel drive EV. The 4th International Conference on Electrical Engineering and Informatics 2013; 11: 593-601.
[124] Ze Q, Kou P, Liang D and Liang Z. Fault-tolerant performances of switched reluctance machine and doubly salient permanent magnet machine in starter/generator system. IEEE International Conference on Electrical Machines and Systems 2015; 46: 549-55.
[125] Mcgehee J and Yoon HS. Optimal torque control of an integrated starter-generator using genetic algorithms. Proceedings of the Institution of Mechanical Engineers Part D Journal of Automobile Engineering 2014; 229: 875-884.
[126] Lambiase F, Di Ilio A (2014) An experimental study on clinched joints realized with different dies. Thin-Walled Struct 85:71–80.
[127] Varis JP (2002) The suitability of round clinching tools for high strength structural steel. Thin-Walled Struct 40:225–238.
[128] Mucha J (2011) The analysis of lock forming mechanism in the clinching joint. Mater Des 32:4943–4954.

[129] Mucha J (2014) The numerical analysis of the effect of the joining process parameters on self-piercing riveting using the solid rivet. Arch Civ Mech Eng 14:444–454.
[130] Mucha J, Kaščák L, Spišák E (2011) Joining the car-body sheets using clinching process with various thickness and mechanical property arrangements. Arch Civ Mech Eng 11(1):135–148.
[131] Mucha J, Witkowski W (2013) The experimental analysis of the double joint type change effect on the joint destruction process in uniaxial shearing test. Thin-Walled Struct 66:39–49.
[132] Lambiase F (2013) Influence of process parameters in mechanical clinching with extensible dies. Int J Adv Manuf Technol 66:2123–2131.
[133] Lambiase F, Di Ilio A, Paoletti A (2015) Joining aluminium alloys with reduced ductility by mechanical clinching. Int J Adv Manuf Technol 77:1295–1304.
[134] Eshtayeh MM, Hrairi M, Mohiuddin AKM (2016) Clinching process for joining dissimilar materials state of the art. Int J AdvManuf Technol 82:179–195.
[135] Eshtayeh MM, Hrairi M (2016) Recent and future development of the application of finite element analysis in clinching process. Int J Adv Manuf Technol 84:2589–2608.
[136] Lee CJ, Kim JY, Lee SK, Ko DC, KimBM(2010) Parametric study on mechanical clinching process for joining aluminum alloy and high-strength steel sheets. J Mech Sci Technol 24:123–126.
[137] Coppieters S, Cooreman S, Lava P, Sol H, Van Houtte P, Debruyne D (2011) Reproducing the experimental pull-out and shear strength of clinched sheet metal connections using FEA. Int JMater Form 4:429–440.
[138] Coppieters S, Lava P, Baes S, Sol H, Van Houtte P, Debruyne D (2012) Analytical method to predict the pull-out strength of clinched connections. Thin-Walled Struct 52:42–52.
[139] Lambiase F, Di Ilio A (2016) Damage analysis in mechanical clinching: experimental and numerical study. J Mater Process Technol 230:109–120.
[140] Jiang T, Liu ZX,Wang PC (2015) Effect of aluminum pre-straining on strength of clinched galvanized SAE1004 steel-to-AA6111-T4 aluminum. J Mater Process Technol 215:193–204.
[141] Lee CJ, Kim JY, Lee SK, Ko DC, Kim BM (2010) Design of mechanical clinching tools for joining of aluminium alloy sheets. Mater Des 31:1854–1861.
[142] Lambiase F, DuranteM, Di Ilio A (2016) Fast joining of aluminum sheets with glass fiber reinforced polymer (GFRP) by mechanical clinching. J Mater Process Technol 236:241–251.
[143] Lambiase F (2015) Clinch joining of heat-treatable aluminum AA6082-T6 alloy under warm conditions. J Mater Process Technol 225:421–432.
[144] Lambiase F (2015)Mechanical behaviour of polymer–metal hybrid joints produced by clinching using different tools. Mater Des 87: 606–618.
[145] Lambiase F (2015) Joinability of different thermoplastic polymers with aluminium AA6082 sheets by mechanical clinching. Int J Adv Manuf Technol 80:1995–2006.

[146] Eshtayeh M, Hrairi M, Mohiuddin AKM (2016) Multi objective optimization of clinching joints quality using Grey-based Taguchi method. Int J Adv Manuf Technol. doi:10.1007/s00170-016-8471-1.
[147] Jiang T, Liu ZX, Wang PC (2015) Quality inspection of clinched joints of steel and aluminum. Int J Adv Manuf Technol 76:1393–1402.
[148] Abe Y, Mori K, Kato T (2012) Joining of high strength steel and aluminium alloy sheets by mechanical clinching with dies for control of metal flow. J Mater Process Technol 212:884–889.
[149] He XC, Zhao L, Yang HY, Xing BY, Wang YQ, Deng CJ, FS G, Ball A (2014) Investigations of strength and energy absorption of clinched joints. Comput Mater Sci 94:58–65.
[150] Saberi S, Enzinger N, Vallant R, Cerjak H, Hinterdorfer J, Rauch R (2008) Influence of plastic anisotropy on the mechanical behavior of clinched joint of different coated thin steel sheets. Int J Mater Form Suppl 1:273–276.
[151] He XC, Liu FL, Xing BY, Yang HY, Wang YQ, Deng CJ, FS G, Ball A (2014) Numerical and experimental investigations of extensible die clinching. Int J Adv Manuf Technol 74:1229–1236.
[152] Mucha J, Witkowski W (2014) The clinching joints strength analysis in the aspects of changes in the forming technology and load conditions. Thin-Walled Struct 82:55–66.
[153] Wen T,Wang H, Yang C, Liu LT (2014) On a reshaping method of clinched joints to reduce the protrusion height. Int J Adv Manuf Technol 71:1709–1715.
[154] Mucha J, Kaščák L, Spišák E (2013) The experimental analysis of forming and strength of clinch riveting sheet metal joint made of different materials. Adv Mech Eng 5:1–11.
[155] Chen C, Zhao SD, Han XL, Cui MC, Fan SQ (2016) Optimization of a reshaping rivet to reduce the protrusion height and increase the strength of clinched joints. J Mater Process Technol 234:1–9.
[156] Chen C, Zhao SD, Cui MC, Han XL, Fan SQ (2016) Mechanical properties of the two-steps clinched joint with a clinch-rivet. J Mater Process Technol 237:361–370.
[157] Chen C, Zhao SD, CuiMC, Han XL, Fan SQ (2016) Numerical and experimental investigations of the reshaped joints with and without a rivet. Int J Adv Manuf Technol. doi:10.1007/s00170-016-8889-5.
[158] Chen C, Zhao SD, Han XL, Cui MC, Fan SQ (2016) Investigation of mechanical behavior of the reshaped joints realized with different reshaping forces. Thin-Walled Struct 107:266–273.
[159] S.M. Zaytsev, A.M. Popov, E.V. Chernykh, R.D. Voronina, N.B. Zorov, T.A. Labutin, Comparison of single- and multivariate calibration for determination of Si, Mn, Cr and Ni in high-alloyed stainless steels by laser-induced breakdown spectrometry, J. Anal. At. Spectrom. 29(2014)1417-1424.
[160] S.D. Zhang, X.H. Wang, M.H. He, Y.B Jiang, B.C. Zhang, W. Hang, B.L. Huang, Laser-induced plasma temperature, Spectrochim. Acta, Part B 97(2014) 13-33.

[161] C. Hanson, S. Phongikaroon, J.R. Scott, Temperature effect on laser-induced breakdown spectroscopy spectra of molten and solid salts, Spectrochim. Acta, Part B 97(2014) 79-85.
[162] H. Loudyi, K. Rifaï, S. Laville, F. Vidal, M. Chaker, M. Sabsabi. “Improving laser-induced breakdown spectroscopy (LIBS) performance for iron and lead determination in aqueous solutions with laser-induced fluorescence (LIF)”. J. Anal. At. Spectrom. 2009. 24: 1421-1428.
[163] H.M. Solo-Gabriele, T.G. Townsend, D.W. Hahn, T.M. Moskal, N. Hosein, J. Jambeck, and G. Jacobi, "Evaluation of XRF and LIBS technologies for on-line sorting of CCA-treated wood waste," Waste Management, 24(4), 413-424, 2004.
[164] T.M. Moskal and D.W. Hahn, "On-line sorting of wood treated with chro-mated copper arsenate using laser-induced breakdown spectroscopy," Applied Spectroscopy, 56(10), 1337-1344, 2002.
[165] M.N. Siddiqui, M.A. Gondal, and M.M. Nasr, "Determination of trace met-als using laser induced breakdown spectroscopy in insoluble organic mate-rials obtained from pyrolysis of plastics waste," Bulletin of Environmental Contamination and Toxicology, 83, 141-145, 2009.
[166] J. Anzano, B. Bonilla, B. Montull-Ibor, R.-J. Lasheras, and J. Casas-Gonzalez, "Classifications of plastic polymers based on spectral data analysis with laser induced breakdown spectroscopy," Journal of Polymer Engineering, 30(3-4), 177-187, 2010.
[167] M.A. Gondal and M.N. Siddiqui, "Identification of different kinds of plastics using laser-induced breakdown spectroscopy for waste manage-ment," Journal of Environmental Science and Health Part A, 42(13), 1989- 1997, 2007.
[168] G. Asimellis, N. Michos, I. Fasaki, and M. Kompitsas, "Platinum group met-als bulk analysis in automobile catalyst recycling material by laser-induced breakdown spectroscopy," Spectrochimica Acta Part B, 63(11), 1338-1343, 2008.
[169] W. L. Yip, N. H. Cheung. “Analysis of aluminum alloys by resonance-enhanced laser-induced breakdown spectroscopy: How the beam profile of the ablation laser and the energy of the dye laser affect analytical performance”. Spectrochim. Acta Part B 2009. 64: 315-322.
[170] C. Goueguel, S. Laville, F. Vidal, M. Sabsabi, M. Chaker. “Investigation of resonance-enhanced laser-induced breakdown spectroscopy for analysis of aluminium alloys”. J. Anal. At. Spectrom. 2010. 25: 635-644.
[171] J. Uebbing, J. Brust, W. Sdorra, F. Leis, K. Niemax. “Reheating of a laser-produced plasma by a second pulse laser”. Appl. Spectrosc. 1991. 45: 1419-1423.
[172] V.N. Lednev, S.M. Pershin, A.F. Bunkin, A.A. Samokhvalov, V.P. Veiko, S.I. Kudryashov, A.A. Ionin. “Double pulse laser induced breakdown spectroscopy with Gaussian and multimode beams”. Spectrochim. Acta Part B 2016. 124: 47-55.
[173] T. Fujimoto. Plasma Spectroscopy, Oxford University Press on Demand, 2004.
[174] X.B. Zhang, Y. Deguchi, J.P. Liu. “Numerical simulation of laser induced weakly ionized helium plasma process by lattice boltzmann method”. Jpn. J. Appl. Phys. 2012. 51: 01AA04-1-01AA04-6.

[175] O. Barthelemy, J. Margot, S. Laville, F. Vidal, M. Chaker, B. Le Drogoff, T.W. Johnston, M. Sabsabi. “Investigation of the State of Local Thermodynamic Equilibrium of a Laser-Produced Aluminum Plasma”. Appl. Spectrosc. 2005. 59: 529-536.
[176] M. Skočić, S. Bukvić. “Laser Induced Plasma Expansion and Existence of Local Thermodynamic Equilibrium”. Spectrochim. Acta Part B 2016. 125: 103-110.
[177] J.N. Miller, J.C. Miller. Statistics and Chemometrics for Analytical Chemistry, 6th ed., Prentice Hall, England, 2006.
[178] A. Sarkar, X.L. Mao, G. C.-Y. Chan, R. E. Russo. “Laser ablation molecular isotopic spectrometry of water for ${}_1D^2/{}_1H^1$ ratio analysis”. Spectrochim. Acta Part B. 2013. 88: 46-53.
[179] Gruber, J., Heitz J., Arnold N., Bäuerle D., Ramaseder N., Meyer W., Hochörtler J., Koch F. “In situ analysis of metal melts in metallurgic vacuum devices by laser-induced breakdown spectroscopy.” Applied spectroscopy 2004. 58(4): 457-462.
[180] S. Palanco, L. M. Cabalin, D. Romero and J. J. Laserna, Infrared laser ablation and atomic emission spectrometry of stainless steel at high temperatures, J. Anal. At. Spectrom. 1999, 14: 1883-1887.

Acknowledgements

The author moved into this challenging double Ph. D. program in October 2016 and the present dissertation has grown out of work performed at the Laser & Plasma Laboratory in Tokushima University, Japan and the Intelligent Control Systems Laboratory in Xi'an Jiaotong University, China. Thanks are due to all people who have instructed and helped for the present work in the past few years.

This dissertation can be completed successfully and the author can graduate from doctor course early less than two years. The author likes to express his deepest gratitude goes to the professors including Prof. Deguchi, the supervisor in Tokushima University, and Prof. Zhao, the supervisor in Xi'an Jiaotong University for their continued encouragement and guidance at all the stages. The author is also greatly indebted to the members and the staffs in Tokushima University who gave the author their help as possible as they could. Especially, the author would like to extend his gratitude to the members of LIBS research group in Laser & Plasma Laboratory, Mr. Fujita, Mr. Tanaka, Mr. Furukawa and Mr. Hayashi, thanks to the kind help for the experiments and discussion.

The author owes his sincere gratitude to his parents for their loving considerations and great confidence in the author all through these years.

Very special thanks go to the author's wife for her help, patience, and encouragement in the past 7 years.

Minchao Cui

Tokushima,
July, 2018

Achievements

International Journal Papers

[1] **Minchao Cui**, Yoshihiro Deguchi, Zhenzhen Wang, Yuki Fujita, Renwei Liu, Fang-Jung Shiou, Shengdun Zhao. "Enhancement and stabilization of plasma using collinear long-short double-pulse laser-induced breakdown spectroscopy". Spectrochimica Acta Part B: Atomic Spectroscopy. Doi: 10.1016/j.sab.2018.02.002. (SCI Indexed)

[2] **Minchao Cui**, Shengdun Zhao, Chao Chen, Da-Wei Zhang, Jingxiang Li, Yongyi Li. "Study on warm forming effects of the axial-pushed incremental rolling process of spline shaft with 42CrMo steel". Proceedings of the Institution of Mechanical Engineers, Part E: Journal of Process Mechanical Engineering. Doi: 10.1177/0954408917727214. (SCI Indexed)

[3] **Minchao Cui**, Shengdun Zhao, Chao Chen, Fei Jing. "Study on the 12-10 flux switching integrated-starter-generator for hybrid electric vehicle application". Proceedings of the Institution of Mechanical Engineers, Part D: Journal of Automobile Engineering. Doi: 10.1177/0954407017733887. (SCI Indexed)

[4] **Min-Chao Cui**, Sheng-Dun Zhao, Da-Wei Zhang, Chao Chen, Yong-Yi Li. "Finite element analysis on axial-pushed incremental warm rolling process of spline shaft with 42CrMo steel and relevant improvement". The International Journal of Advanced Manufacturing Technology. Doi: 10.1007/s00170-016-9566-4. (SCI Indexed)

[5] **Min-Chao Cui**, Sheng-Dun Zhao, Chao Chen, Da-Wei Zhang, Yong-Yi Li. "Process parameter determination of the axial-pushed incremental rolling process of spline shaft". The International Journal of Advanced Manufacturing Technology. Doi: 10.1007/s00170-016-9604-2. (SCI Indexed)

[6] **Min-Chao Cui**, Sheng-Dun Zhao, Da-Wei Zhang, Chao Chen, Shu-Qin Fan, Yongyi Li. "Deformation mechanism and performance improvement of spline shaft with 42CrMo steel by axial-infeed incremental rolling process". The International Journal of Advanced Manufacturing Technology. Doi: 10.1007/s00170-016-8997-2. (SCI Indexed)

[7] **Minchao Cui**, Shengdun Zhao, Chao Chen, Dawei Zhang, Yongyi Li. "Finite element modeling and analysis for the integration–rolling–extrusion process of spline shaft". Advances in Mechanical Engineering. Doi: 10.1177/1687814016688585. (SCI Indexed)

[8] **Minchao Cui**, Shengdun Zhao, Yoshihiro Deguchi, Chao Chen, Dengzhu Fan. "Performance of Flux Switching Integrated Starter-Generator system with dual-mode control circuit". International Journal of Mechatronics and Automation. (Accepted on May, 17th , 2018)

[9] Da-Wei Zhang, **Min-Chao Cui**, Miao Cao, Ning-Yu Ben, Sheng-Dun Zhao. “Determination of friction conditions in cold-rolling process of shaft part by using incremental ring compression test”. The International Journal of Advanced Manufacturing Technology. Doi: 10.1007/s00170-017-0087-6. (SCI Indexed)

[10] Hongxing Sun, **Min-Chao Cui**, Yishuai Zhang, Sheng-Dun Zhao, Da-Wei Zhang, Yoshihiro Deguchi. “Performance of AC servo axial-infeed incremental warm rolling equipment and simulated production of spline shafts”. The International Journal of Advanced Manufacturing Technology. Doi: 10.1007/s00170-017-1003-9. (SCI Indexed)

[11] Chao Chen, Shengdun Zhao, **Minchao Cui**, Xiaolan Han, Shuqin Fan, Tohru Ishida. “An experimental study on the compressing process for joining Al6061 sheets”. Thin-Walled Structures. Doi: 10.1016/j.tws.2016.08.007. (SCI Indexed)

[12] Chao Chen, Shengdun Zhao, **Minchao Cui**, Xiaolan Han, Xuzhe Zhao, Tohru Ishida. “Effects of geometrical parameters on the strength and energy absorption of the height-reduced joint”. The International Journal of Advanced Manufacturing Technology. Doi: 10.1007/s00170-016-9619-8. (SCI Indexed)

[13] Chao Chen, Shengdun Zhao, **Minchao Cui**, Xiaolan Han, Shuqin Fan, Xuzhe Zhao. “Comparative investigation of auxiliary processes for increasing the strength of clinched joints”. Proceedings of the Institution of Mechanical Engineers, Part E: Journal of Process Mechanical Engineering. Doi: 10.1177/0954408916686998. (SCI Indexed)

[14] Chao Chen, Shengdun Zhao, **Minchao Cui**, Xiaolan Han, Shuqin Fan. “Mechanical properties of the two-steps clinched joint with aclinch-rivet”. Journal of Materials Processing Technology. Doi: 10.1016/j.jmatprotec.2016.06.024. (SCI Indexed)

[15] Chao Chen, Shengdun Zhao, **Minchao Cui**, Xiaolan Han, Ningyu Ben. “Numerical and experimental investigations of the reshaped joints with and without a rivet”. The International Journal of Advanced Manufacturing Technology. Doi: 10.1007/s00170-016-8889-5. (SCI Indexed)

[16] Chao Chen, Shengdun Zhao, Xiaolan Han, **Minchao Cui**, Xuzhe Zhao, Tohru Ishida. “Experimental investigation of the mechanical reshaping process for joining aluminum alloy sheets with different thicknesses”. Journal of Manufacturing Processes. Doi: 1 0.1016/j.jmapro.2017.01.015. (SCI Indexed)

[17] Chao Chen, Shengdun Zhao, Xiaolan Han, **Minchao Cui**, Shuqin Fan. “Investigation of mechanical behavior of the reshaped joints realized with different reshaping forces”. Thin-Walled Structures. Doi: 10.1016/j.tws.2016.06.020. (SCI Indexed)

[18] Chao Chen, Shengdun Zhao, Xiaolan Han, **Minchao Cui**, Shuqin Fan. "Optimization of a reshaping rivet to reduce the protrusion height and increase the strength of clinched joints". Journal of Materials Processing Technology. Doi: 10.1016/j.jmatprotec.2016.03.006. (SCI Indexed)

[19] Chao Chen, Shengdun Zhao, Xiaolan Han, **Minchao Cui**, Shuqin Fan. "Investigation of the height-reducing method for clinched joint with AL5052 and AL6061". The International Journal of Advanced Manufacturing Technology. Doi: 10.1007/s00170-016-9266-0. (SCI Indexed)

[20] Chao Chen, Shuqin Fan, Xiaolan Han, Shengdun Zhao, **Minchao Cui**, Tohru Ishida. "Experimental study on the height-reduced joints to increase the cross-tensile strength". The International Journal of Advanced Manufacturing Technology. Doi: 10.1007/s00170-016-9939-8. (SCI Indexed)

[21] Chao Chen, Shuqin Fan, Xiaolan Han, Shengdun Zhao, **Minchao Cui**, Tohru Ishida. "Experimental research on the compressed joints with different geometrical parameters". Proceedings of the Institution of Mechanical Engineers, Part B: Journal of Engineering Manufacture. Doi: 10.1177/0954405417711735. (SCI Indexed)

[22] **Minchao Cui**, Shengdun Zhao, Chao Chen, Dengzhu Fan, Jing Hao. "Study on the Control Circuits of Flux Switching Integrated Starter and Generator for HEV Application". Proceedings of 2017 IEEE International Conference on Mechatronics and Automation. Doi: 10.1109/ICMA.2017.8015980. (EI Indexed)

[23] Dazhou Liu, Shengdun Zhao, **Minchao Cui**, Shuaipeng Liu, Jiaming Gao. "Study and Improvements on the Rolling Loads of Axial Incremental Rolling Process for Spline Shaft Based on Finite Element Method". Proceedings of 2017 IEEE International Conference on Mechatronics and Automation. Doi: 10.1109/ICMA.2017.8015791. (EI Indexed)

International symposiums and conferences

[1] **M.C. Cui**, S.D. Zhao, C. Chen, D.Z. Fan, J. Hao, Study on the Control Circuits of Flux Switching Integrated Starter and Generator for HEV Application (doi: 10.1109/ICMA.2017.8015980). Proceedings of 2017 IEEE International Conference on Mechatronics and Automation (IEEE ICMA 2017), August 6th -9th, Takamatsu, Japan.（Oral Presentation）

[2] **M.C. Cui**, Y. Deguchi, Z.Z. Wang, Y. Fujita, R.W. Liu, Dynamics and Parameters of Plasma Generated by Long and Short Dual Pulses Laser Interacting with Steel Sample. Colloquium

Spectroscopicum Internationale XL & 9th Euro-Mediterranean Symposium on LIBS (CSI XL & EMSLIBS 2017), June 11th-16th, Pisa, Italy. （Oral Presentation）

[3] **M.C. Cui**, Y. Deguchi, Z.Z. Wang, C.X. Wang, B.W. Xue, Quantitative analysis of manganese in steel samples at different temperatures using long-short DP-LIBS. 2nd Asian Symposium on Laser Induced Breakdown Spectroscopy (ASLIBS 2017), August 27th-31st, Tokushima, Japan. （Oral Presentation）

[4] **M.C. Cui**, Y. Deguchi, R.W. Liu, Y. Fujita, Application of collinear long and short dual-pulse LIBS to carbon steel samples. 3rd International Forum on Advanced Technologies (IFAT 2017), March 9th-11th, Hualien, Taiwan. （Poster Presentation）

[5] **M.C. Cui**, Y. Deguchi, Z.Z. Wang, C.X. Wang, B.W. Xue, Z.F. Miao, Reduction of sample temperature influences on LIBS by long pulse laser beam. 2nd Asian Symposium on Laser Induced Breakdown Spectroscopy (ASLIBS 2017), August 27th-31st, Tokushima, Japan. （Poster Presentation）

[6] **M.C. Cui**, Y. Deguchi, Z.Z. Wang, S.D. Zhao, Application of collinear long-short DP-LIBS to iron and steel samples under different temperatures. 4th International Forum on Advanced Technologies (IFAT 2018), March 8th-9th, Tokushima, Japan. （Poster Presentation）

[7] Y. Deguchi, Z.Z. Wang, **M.C. Cui**, Y. Fujita, R.W. Liu, J.J. Yan, Improved Detection Ability Using Collinear Long and Short DP-LIBS. Colloquium Spectroscopicum Internationale XL & 9th Euro-Mediterranean Symposium on LIBS (CSI XL & EMSLIBS 2017), June 11th-16th, Pisa, Italy. （Oral Presentation）

[8] D.Z. Liu, S.D. Zhao, **M.C. Cui**, S.P. Liu, J.M. Gao, Study and Improvements on the Rolling Loads of Axial Incremental Rolling Process for Spline Shaft Based on Finite Element Method (doi: 10.1109/ICMA.2017.8015791). Proceedings of 2017 IEEE International Conference on Mechatronics and Automation (IEEE ICMA 2017), August 6th -9th, Takamatsu, Japan. （Poster Presentation）

[9] Y. Deguchi, Z.Z. Wang, **M.C. Cui**, F.J. Shiou, Development of Long and Short Pulse DP-LIBS with 3D Profile Measurement to Iron and Steel Making Processes. 2nd Asian Symposium on Laser Induced Breakdown Spectroscopy (ASLIBS 2017), August 27th-31st, Tokushima, Japan. （Oral Presentation）

[10] Y. Fujita, Y. Deguchi, **M.C. Cui**, S. Tanaka, R. Furukawa, Development of long and short double-pulse LIBS to porous materials put on water. 2nd Asian Symposium on Laser Induced Breakdown Spectroscopy (ASLIBS 2017), August 27th-31st, Tokushima, Japan. （Poster Presentation）

[11] S. Tanaka, Y. Deguchi, Y. Fujita, R. Furukawa, **M.C. Cui**, Development of real time measurement of trace element Detection Using LB-TOFMAS. 2nd Asian Symposium on Laser Induced Breakdown Spectroscopy (ASLIBS 2017), August 27th-31st, Tokushima, Japan. （Poster Presentation）

[12] Y. Fujita, Y. Deguchi, **M.C. Cui**, S. Tanaka, R. Furukawa, Development of long and short DP-LIBS to porous materials underwater. 4th International Forum on Advanced Technologies (IFAT 2018), March 8th-9th, Tokushima, Japan. （Poster Presentation）

[13] S. Tanaka, Y. Deguchi, **M.C. Cui**, Y. Fujita, R. Furukawa, Development of quantitative measurement technology for steel materials in long distance using LIBS. 4th International Forum on Advanced Technologies (IFAT 2018), March 8th-9th, Tokushima, Japan. （ Poster Presentation）

[14] B.W. Xue, Y. Deguchi, **M.C. Cui**, C.X. Wang, Z.F. Miao, Influences of Sample Microstructure on Plasma Emission Characteristics Using SP-LIBS and Long-short DP-LIBS. 2nd Asian Symposium on Laser Induced Breakdown Spectroscopy (ASLIBS 2017), August 27th-31st, Tokushima, Japan. （Poster Presentation）

[15] R.W. Liu, Y. Deguchi, **M.C. Cui**, Z.Z. Wang, J.P. Liu, J.J. Yan, Situation analysis of LIBS measurement on steel samples under different sample temperature. 2nd Asian Symposium on Laser Induced Breakdown Spectroscopy (ASLIBS 2017), August 27th-31st, Tokushima, Japan. （Poster Presentation）

[16] C.X. Wang, Y. Deguchi, **M.C. Cui**, B.W. Xue, Z.F. Miao, Emission Characteristics of the Plasma Generated by LIBS from Steel Samples in Different Temperatures. 2nd Asian Symposium on Laser Induced Breakdown Spectroscopy (ASLIBS 2017), August 27th-31st, Tokushima, Japan. （Poster Presentation）

[17] Z.F. Miao, Y. Deguchi, **M.C. Cui**, C.X. Wang, B.W. Xue, Quantitative analysis of Cadmium in Soil Samples Using LIBS. 2nd Asian Symposium on Laser Induced Breakdown Spectroscopy (ASLIBS 2017), August 27th-31st, Tokushima, Japan. （Poster Presentation）

[18] S. Tanaka, Y. Deguchi, Y. Fujita, R. Furukawa, **M.C. Cui**, Development of real time measurement of trace element Detection Using LB-TOFMAS. 2nd Asian Symposium on Laser Induced Breakdown Spectroscopy (ASLIBS 2017), August 27th-31st, Tokushima, Japan. （Poster Presentation）

[19] R. Furukawa, Y. Deguchi, Y. Fujita, S. Tanaka, **M.C. Cui**, Long distance measurement of steel samples using LIBS. 2nd Asian Symposium on Laser Induced Breakdown Spectroscopy (ASLIBS 2017), August 27th-31st, Tokushima, Japan. （Poster Presentation）

[20] Z.Z. Wang, Y. Deguchi, R.M. Hu, R.W. Liu, **M.C. Cui**, J.J. Yan, J.P. Liu, Comparison of detection ability between SP-LIBS and DP-LIBS. 2nd Asian Symposium on Laser Induced Breakdown Spectroscopy (ASLIBS 2017), August 27th-31st, Tokushima, Japan. （Oral Presentation）

[21] B.W. Xue, Y. Deguchi, **M.C. Cui**, C.X. Wang, Z.F. Miao, The study of laser induced breakdown spectroscopy to measure underwater metal materials. 4th International Forum on Advanced Technologies (IFAT 2018), March 8th-9th, Tokushima, Japan. （Poster Presentation）

[22] C.X. Wang, Y. Deguchi, **M.C. Cui**, B.W. Xue, Inter-pulse delay optimization in long-short DPLIBS of a steel sample at different temperatures, 4th International Forum on Advanced Technologies (IFAT 2018), March 8th-9th, Tokushima, Japan. （Poster Presentation）

[23] Z.F. Miao, Y. Deguchi, **M.C. Cui**, B.W. Xue, The application of LIBS on soil pollution. 4th International Forum on Advanced Technologies (IFAT 2018), March 8th-9th, Tokushima, Japan. （Poster Presentation）

Domestic workshops

[1] **M.C. Cui**, Y. Deguchi, R.W. Liu, Y. Fujita, Z.Z. Wang, S.D. Zhao, Z.T. Hu, Application of collinear long and short dual-pulse LIBS to iron and steel samples. 第４回先端計測技術の応用展開に関するシンポジウム(Forth symposium on applications of advanced measurement technologies SAAMT2016), 12月8日－9日, 東海村産業・情報プラザ。（Poster Presentation）

[2] 出口 祥啓, Z.Z. Wang, **M.C. Cui**, F.J. Shiou, ロングショートダブルパルスLIBSを用いたLIBS計測特性の改善. レーザー学会学術講演会第38回年次大会講演予稿集, 平成30年1月24日－26日, 京都市勧業館みやこめっせ。（Oral Presentation）